Applied Research and Innovation Branch

POST-FIRE GROUND TREATMENTS

Christopher Bareither
Paul Heyliger
Kayla Moden
Kirsten Peterson

1. Report No. CDOT-2018-19	2. Government Accession No.	3. Recipient's Catalog No.
4. Title and Subtitle POST-FIRE GROUND TREATMENTS		5. Report Date 26 June 2018
		6. Performing Organization Code 115.02
7. Author(s) Christopher Bareither, Paul Heyliger, Kayla Moden, and Kirsten Peterson		8. Performing Organization Report No. CDOT-2018-19
9. Performing Organization Name and Address Colorado State University Fort Collins, CO		10. Work Unit No. (TRAIS)
		11. Contract or Grant No.
12. Sponsoring Agency Name and Address Colorado Department of Transportation - Research 2829 W. Howard Pl. Denver CO, 80204		13. Type of Report and Period Covered Final: 1/1/16 to 12/31/17
		14. Sponsoring Agency Code
15. Supplementary Notes Prepared in cooperation with the US Department of Transportation, Federal Highway Administration		
16. The objective of this project was to assess the efficacy of post-fire ground treatment in mitigating erosion and runoff on soil slopes subjected to wildfires. This objective was achieved through physical slope-model experiments and discrete element method (DEM) modeling. The physical experiments were conducted on block soil samples collected from U.S. Forest Service land in Colorado. The samples included were subjected to rainfall simulations characteristic of a typical short-duration, high-intensity summer storm. Rainfall simulations were completed on block samples with natural intact vegetation, burned vegetation, and burned vegetation plus straw mulch applied as ground cover. Soil erosion measured on the burned soil samples increased relative to the unburned soils. However, the presence of straw mulch on the surface of a burned soil reduced erosion to levels coincident with natural intact vegetation. The DEM models were completed on 2-dimensional and 3-dimensional assemblies of particles that included different arrangements of reinforcements to simulate soils with root networks present in unburned soils with intact vegetation compared to burned soils with the root networks destroyed from burning. Model simulations indicated that an increase in the root network inhibited particles dislodgement and decreased downslope movement of particles.		
17. erosion, geotechnical engineering, numerical modeling, runoff, soil, wildfire	18. Distribution Statement This document is available on CDOT's website http://www.coloradodot.info/programs/research/pdfs	
19. Security Classif. (of this report) Unclassified	20. Security Classif. (of this page) Unclassified	21. 186	22. Price

Form DOT F 1700.7 (8-72)   Reproduction of completed page authorized

ACKNOWLEDGEMENT

EXECUTIVE SUMMARY

The objective of this project was to assess the efficacy of post-fire ground treatment in mitigating erosion and runoff on soil slopes subjected to wildfires. This objective was achieved through physical slope-model experiments and discrete element method (DEM) modeling. The effects of soil surface vegetation burning and straw mulch application on runoff and erosion of soil surfaces was evaluated using a laboratory-scale slope-model experiment. Rainfall simulations were conducted on intact block samples with natural vegetation, burned vegetation, and burned vegetation and straw mulch applied as ground cover. The amount of runoff and erosion increased with a decrease in soil surface vegetation. Removal of surface vegetation via burning did not directly increase runoff, but did increase erosion. Applying straw mulch to the surface of a burned block sample reduced runoff rates and sediment concentrations relative to burned block samples without ground cover. This phenomenon was attributed to the ability of the ground cover to dissipate raindrop impact energy and temporary store precipitation. Straw mulch also reduced erosion via acting as a barrier to entrap dislodged soil particles, preventing downslope movement.

The ash layer present on burned soil surfaces had high infiltration capacity and acted as a water storage layer. A hydrophobic layer identified below the ash layer on the burned soil surfaces prevented water infiltration from the wettable ash layer deeper into the soil, which increased runoff from burned samples during subsequent rainfall simulations. Straw mulch helped protect the ash layer from eroding during rainfall simulations, which helped maintain the ability of the ash layer to provide water storage. Geotechnical property tests were also conducted on unburned and burned subsamples to evaluate changes in physical characteristic and hydraulic and mechanical properties due to burning. Changes in soil physical characteristics and hydraulic and mechanical properties

with high severity burning were not found in this study. Similarities in dry density, organic matter, field saturated hydraulic conductivity, and shear strength between unburned and burned soil samples suggested that increases in erosion on burned samples during rainfall simulations could be attributed to destruction of surface cover with burning.

Discrete element method modeling was completed on 2-dimensional (2-D) and 3-dimensional (3-D) particle assemblies that included different arrangements of reinforcements to the development of roots within over time in a burned soil. The DEM simulations represented idealized assemblies of particles and aided in the evaluation of soil behavior at a particulate level. More pronounced particle displacements and larger percent sediment yields occurred with higher drag forces applied to the particle surfaces that represented faster overland flow. Root reinforcements in all 2-D and 3-D DEM simulations helped inhibit particle movement, reduced sediment yields, and stabilized the slopes. An Increase in the amount of root reinforcement, which simulated root growth over time after a fire, decreased particle movement and sediment yield. In general, steeper slopes were associated with larger particle movement and larger sediment yields than less steep slopes subjected to the same drag forces.

IMPLEMENTATION STATEMENT

The lessons learned in the study can be used to mitigate the effects of post-fire conditions contributing to erosion, runoff, and potential debris flows. Based on the research and analyses presented herein, the following recommendations were developed for CDOT: (i) surface vegetation of post-burned soil slopes should be evaluated immediately following a wildfire and areas with high-burn severity (e.g., surface vegetation completely removed via burning) should have ground treatment applied to mitigate erosion and runoff; (ii) straw mulch used as a ground

cover should be applied at a rate of at least 0.06 kg/m^2 to reduce erosion to conditions relative to in-tact vegetation; and (iii) seeding should be applied along with ground cover application to promote re-establishment of surface vegetation to mitigate erosion and runoff long-term. These recommendations apply to high-burn severity ground conditions, straw mulch as the ground treatment, and a precipitation event consistent with that evaluated in this study (i.e., ≈ 50 mm/h).

Although seeding was not directly evaluated in this study, the similarity in erosion (i.e., sediment yield) between block samples with in-tact vegetation and straw mulch support the recommendation that seeding should be implemented concurrently with ground cover to promote re-growth of surface vegetation. The only ground cover evaluated in this study was straw mulch, and thus, the minimum recommended surface application rate of 0.06 kg/m^2 applies to straw mulch and was based on the experiments outlined herein. Other ground covers (e.g., wood chips, hydromulch) or application rates may be equally effective the straw mulch application rate recommended herein; however, additional testing may be needed to determine the effectiveness of a given ground cover for select slope conditions and anticipated precipitation events.

TABLE OF CONTENTS

LIST OF TABLES

LIST OF FIGURES

11

CHAPTER 1: INTRODUCTION

1.1 Background

1.1.1 Wildfires in Mountain West States

Wildfires are a natural phenomenon in Colorado and the western U.S., and the frequency of large, destructive wildfires has increased over the past decade and is forecasted to increase due to climate variability and fuel accumulation from fire suppression (MacDonald and Larsen 2009; Robichaud et al. 2010). Potential damage to the human and built environments is not only associated with burned lands, homes, and infrastructure during a wildfire, but can extend for years following a wildfire in the form of increased runoff from precipitation, soil erosion, and debris flows.

The wildland-urban interface is defined as the area where human development is close to, or within, natural terrain. With more than two million Coloradoans now living in the wildland-urban interface, the protection of lives, infrastructure, and municipal water sources from negative effects of wildfire is critical. There are many social and economic costs imparted by wildfires, including fire mitigation and suppression, property loss or reduction in home values, loss of tax revenue, and injuries or loss of life (Fried et al. 2004; Graham et al. 2011). Millions of taxpayer dollars are spent to suppress and control large fires. Millions more are spent in attempts to stabilize post-fire soil conditions that can lead to mass erosion and debris flows that can damage roads and property, and degrade soil and water resources.

The suppression cost for the High Park Fire that occurred during the summer of 2012 in Larimer County, Colorado was approximately $39.2 million. An estimated additional $24 million will be needed to address emergency stabilization treatments and treatments for public roads and private lands. County roads, CDOT highways, forest service roads, and private roads in the High Park burn area totaled 332 km (206 miles) and nearly 32,380 ha (80,000 acres) were considered

moderate to high soil erosion potential (BAER 2012). The 1996 Buffalo Creek fire in Colorado caused over $20 million in damage to Denver's water supply system (Lynch 2004). With an increase in wildfire frequency and burn area in Colorado, understanding post-fire soil conditions is becoming increasingly important to cost-effectively protect critical infrastructure and resources.

1.1.2 Wildfire Effects on Soil Properties

Runoff and soil erosion are both inversely related to the infiltration capacity of a soil. Infiltration capacity depends on the amount of ground cover, amount of soil organic matter, and presence of soil water repellency. Greater levels of organic matter increase porosity, which increases water storage capacity in soil. Higher amounts of surface roughness create longer flow pathways, which increase the amount of time water has to infiltrate the soil. Thus, ground cover can increase infiltration by increasing surface roughness and organic matter that can prevent soil sealing and mitigate soil detachment, which combine to reduce erosion and runoff. The erodibility of a soil is dependent on infiltration capacity and the ability of soil particles to resist detachment (Wischmeier and Mannering 1969). The ability of soil particles to resist detachment is largely dependent on particle size and the presence of detaching agents such as raindrops and surface flow (Morgan 2005).

Infiltration capacity and ability to resist particle detachment can be altered by moderate- to high-severity wildfires. Wildfires often decrease infiltration capacity by increasing soil dry density through aggregate breakdown (Moody and Martin 2001; Moody and Martin 2009; Ebel et al. 2012), increasing soil sealing by sediment and ash particles following loss of surface cover (Neary et al. 1999; Larsen et al. 2009), and forming a water repellent layer near the soil surface (DeBano 2000; Doerr et al. 2000). Soil particle detachment increases following a wildfire due to loss of soil cover and increased propensity for raindrops to impact and subsequently mobilize soil particles

(Morgan 2005). These aforementioned factors, along with other changes in soil physical characteristics and hydraulic and mechanical properties, result in increased runoff and sediment yield following moderate- to high-severity wildfires.

1.1.3 Post-Fire Ground Treatments

The United States Department of Agriculture (USDA) Forest Service Burn Area Emergency Rehabilitation (BAER) is the formal authority for post-fire response and rehabilitation measures. The goals of BAER are to (1) minimize the threat to life and property onsite or offsite; (2) reduce the loss of soil and onsite productivity; (3) reduce flooding potential; and (4) reduce deterioration of water quality (Neary et al. 2009). To accomplish these goals, BAER teams prescribe hillslope, channel, and/or road treatments. In the past decade, spending on post-fire treatment has increased due to the threat of debris flows and erosion near the growing wildland-urban interface (Robichaud et al. 2000). However, analysis of Burned Area Report forms from over 470 fires estimated that for every dollar spent on post-fire treatments, up to $200 is saved from losses.

Hillslopes are the critical source area for damaging surface runoff and debris flows (MacDonald and Robichaud 2008). Hillslope treatments are implemented to immediately reduce surface runoff and erosion on hillslopes by stabilizing the soil, reducing raindrop impact, promoting infiltration, and/or trapping sediment (Robichaud et al. 2000). Broadcast seeding, seeding plus fertilizer, mulching, contour-felled logs, contour trenching, scarification and ripping, temporary fencing, erosion mats, straw wattles, slash scattering, silt fences, geotextiles, and sand bags are all BAER hillslope treatments. Although certain treatments are known to be more effective than others, the effectiveness of each treatment is dependent on characteristics of the fire and factors unrelated to the fire event. The post-fire response and treatment effectiveness rely on fire characteristics such as burn severity, soil burn severity, amount of bare soil, soil water repellency, soil erodibility, and

time since the fire. Factors independent of the fire event that greatly impact the effectiveness of a given ground treatment are rainfall intensity, topography, and land use (Neary et al. 2005; MacDonald and Robichaud 2008; Robichaud et al. 2010). Considering that all aforementioned factors influence treatment effectiveness, the factors will also influence post-fire erosion (i.e., sediment yield).

Until the 21st century, broadcast seeding was the most common post-fire rehabilitation treatment. This treatment is typically applied aerially and is used to promote rapid vegetation establishment and infiltration to stabilize the soil through plant roots. Seed mixes commonly include legumes to fix nitrogen and native and non-native annual and perennial grasses. Some native species commonly used for post-fire stabilization treatment in Colorado are Canby bluegrass (*Poa canbyi*), slender and streambank wheatgrass (*Elymus genus*), and green needlegrass (*Nassella viridula*). Common non-native or invasive species used are white oat (*Avena sativa*), mountain brome (*Bromus marginatus*), and Idaho fescue (*Festuca idahoensis*) (Bruggink 2007). Although broadcast seeding is cost-effective, non-native species can delay the recovery of natural flora and alter the ecosystem (Baron 1962; Anderson and Brooks 1975; Elliot and White 1987; Conrad et al. 1991).

Bruggink (2007) reported that burned, unseeded plots following the Buffalo Creek Fire in Colorado had higher total species richness than burned plots treated with aerial seeding. Furthermore, studies have shown that grass seed application does not produce a significant increase in ground cover during the first year after a fire event, which is considered the critical year (Roby 1989; Robichaud et al. 2000; Beyers 2004; Robichaud et al. 2013). Seeding becomes effective in erosion control through re-establishing vegetation, which typically requires at least

two years after the fire event. Some seeding treatments also include the application of fertilizers to promote germination and rapid vegetation growth.

Mulching is increasingly becoming a preferred post-fire rehabilitation treatment for land managers. Mulching is a popular treatment option because, like broadcast seeding, mulch can be applied aerially instead of only through ground-based dispersal. Aerial treatment application is viable for otherwise inaccessible areas. Studies on multiple fires indicate that mulching is the most effective post-fire rehabilitation treatment because ground cover is immediately established (MacDonald and Larsen 2009). Agricultural straw mulch and wood-based mulches are commonly used to protect the soil surface from raindrop impact and promote infiltration. Many studies have reported that agricultural straw mulch and wood-based mulches considerably reduced post-fire sediment yield at low cost (Bautista et al. 2009; Robichaud 2000, Yanosek et al. 2006; Foltz and Copeland 2009; Foltz and Wagenbrenner 2010).

In recent years sustainability and environmental impacts associated with human actions have gained attention. Common erosion control practices, such as aerial application of agricultural straw mulch, may be recognized as potentially harmful to the ecosystem. Agricultural straw is non-native and can introduce non-native species, which inhibit re-growth of native vegetation (Foltz and Wagenbrenner 2010). There have been instances where even certified "weed free" straw contains noxious weed seeds. This occurred with straw used in the post-fire treatment of the Hayman Fire in Colorado (Robichaud et al. 2003). Although using agricultural straw as a post-fire stabilization treatment is less expensive than other mulches, straw mulch requires weed monitoring years after the treatment application, which can be expensive (Robichaud et al. 2013). Thus, mulches that are locally-sourced and cost-effective are considered viable alternatives to straw mulch.

1.1.4 Laboratory-Scale Slope-Model Experiment

Over the past few decades, numerous studies have been conducted to evaluate both the effectiveness of post-fire ground treatments in mitigating runoff and erosion and mechanisms of post-fire increases in runoff and erosion (e.g., Larson et al. 2009; Foltz and Wagenbrenner 2010). Although past studies have considered simulated rainfall, disturbed soil samples, and in situ burned soil samples, among other factors; limited laboratory experiments have been conducted on undisturbed soil samples with simulated rainfall to represent natural precipitation events. Few runoff and erosion studies analyzing post-fire ground treatments on burned soil have included unburned soil samples as well (e.g. Foltz and Wagenbrenner 2010).

Foltz and Copeland (2009) conducted laboratory rainfall simulations on unburned, remolded soil samples to evaluate the efficacy of woods shreds for mitigating erosion. Rainfall was simulated using a Purdue-type rainfall simulator where nozzles are used to achieve desired raindrop velocities. They found that increasing wood shred cover increased the time to runoff, reduced the runoff rate, and reduced the sediment delivery rate for a sandy loam soil when compared to a bare plot. Although each increase in wood shred coverage resulted in significantly less sediment loss, they suggested that 30% coverage would be sufficient to limit erosion. Foltz and Wagenbrenner (2010) conducted a similar study but evaluated wood shred performance on burned soils. Burned soils were collected from a recently burned area, and samples were remolded with the ash mixed through-out the soil profile. They found that wood shreds were useful in mitigating erosion and runoff on burned soils and suggested that the increased surface roughness imparted by the wood shreds decreased the runoff energy, therefore, decreasing the sediment yields.

Larsen et al. (2009) and Woods and Balfour (2008) found that the ash layer created from burning was important in reducing runoff and erosion during rainstorms. Larsen et al. (2009) conducted rainfall simulations using a Purdue-type rainfall simulator on field and laboratory plots of

unburned and burned soil. The results indicated that increases in erosion following a wildfire were primarily due to the loss of ground cover rather than fire-induced changes in soil properties. They also suggested that the ash layer reduced runoff and erosion by protecting the mineral soil surface from sealing. Woods and Balfour (2008) conducted rainfall simulations using an oscillating nozzle-type rainfall simulator on field plots of burned soil with and without an ash layer. The results suggested that the ash layer reduced runoff and erosion by providing additional water storage and by preventing soil sealing. Both studies addressed the susceptibility of ash layers to eventual erosion by rain and wind, suggesting that ash may provide reductions in runoff and erosion for only a short time following a fire.

1.1.5 Modeling Particulate Behavior

The two primary methods used to model particulate behavior are continuum based approaches (Eularian) and discrete based approaches (Lagrangian) (Bossy and Safuryn 2016). An example comparing the geometries of a continuum model and a discrete model is shown in
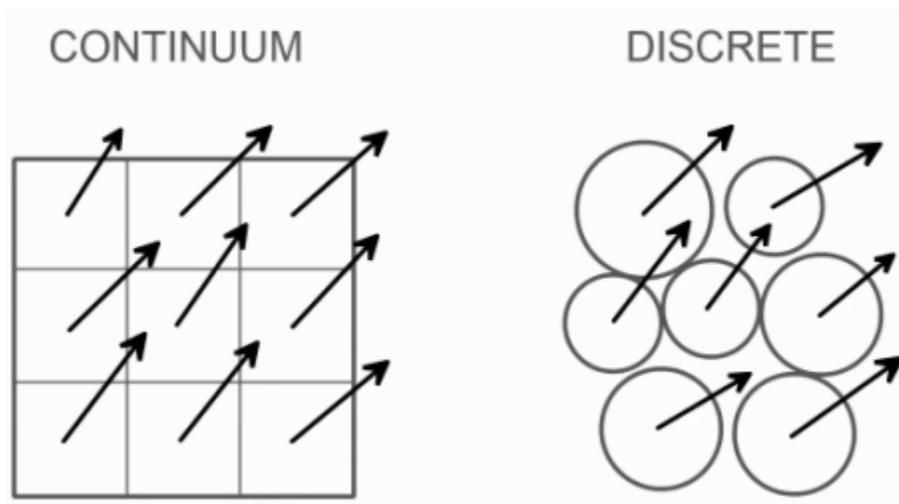
Figure 1. Continuum approaches assume that the material is continuous and all space is filled with

matter; individual particle behavior is ignored. Discrete element modeling represents granular

matter as an idealized assembly of particles with overall macroscopic behavior resulting from the

collection of all particle interactions. The choice between continuum and discrete modeling will

depend on the particular system being simulated, but discrete modeling is preferred when modeling

granular, discontinuous flow (Bossy and Safuryn 2016).
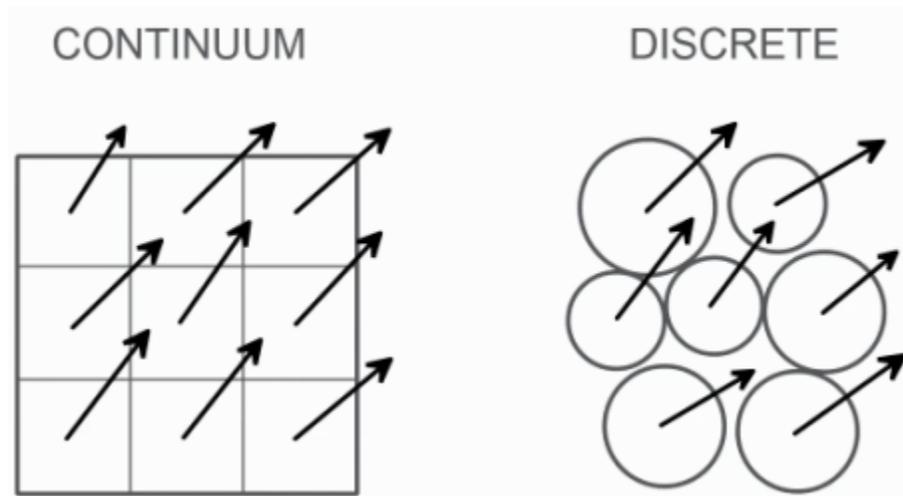
Figure 1. Example system geometry modeled with both a continuum approach and a discrete approach. Arrows show example resultant forces on a continuous material with specified areas in a grid (continuum) and on individual particles (discrete) (Bossy and Safuryn 2016).

There are advantages and disadvantages for both continuum and discrete modeling. The main

advantage of continuum modeling is that, as larger volumes are modeled, continuum modelling

quickly becomes much more computationally efficient than the discrete modeling counterpart

(Coetzee 2014). Disadvantages include difficulty in deciding on a constitutive law that will

accurately represent the mechanics of the system since the constitutive laws for continuum

modeling can be very complex and contain many provisional parameters and equations (Cundall

2001). Also, because the matter is modeled as a continuum, rather than as individual particles free

to move anywhere, capturing localized behavior in a continuum model that uses a mesh can be difficult. The development of shear bands is an example of this behavior (Cundall 2001).

Some advantages to discrete modeling are that the equations between particles are not coupled, the math is fairly straight forward, and the method can be used to study the micromechanics of materials at the element level. One disadvantage to discrete modeling is that analyses can become computationally expensive with an increase in total number of particles in a simulation. For example, to accurately represent macroscopic behavior of a granular material, a large enough volume of the material must be modeled, and a relatively small volume of soil will contain a relatively large number of particles. Therefore, a balance needs to be achieved in discrete modeling where enough particles are modeled to accurately represent the macroscopic behavior while maintaining a reasonable number of particles to keep the analyses to realistic computational times. The most persuasive explanations for using discrete modeling are that macroscopic (and clearly microscopic) behavior of a particulate system depends on particle level behavior, and this method accurately models individual interactions between particles.

1.1.6 The Discrete Element Method

The discrete element method (DEM) can be defined as "a numerical method that simulates the response of granular materials considering the individual particles to be rigid and uses relatively simple models to simulate their interactions" (O'Sullivan 2011). Yet another advantage of DEM modeling is that particle-scale interactions can be monitored that cannot be measured in laboratory tests. This is especially true in the geomechanics field, where laboratory testing is limited, and obtaining an undisturbed soil sample is difficult. Even when an undisturbed soil sample is obtained, measuring particle orientations and rotations is extremely difficult in laboratory tests, whereas this is a straight-forward task in DEM simulations. DEM modeling has the advantage of

capturing the dual nature of granular materials, which can behave both like a solid and a fluid, and then transforming these actions into the bulk behavior of the material. Specifically for the research in this report, DEM modeling from a geomechanics viewpoint is the primary focus, particularly for applications in soil mechanics and geotechnical engineering. However, DEM modeling is used in several different fields, including food technology, chemical engineering, geology, powder technology, physics, mining engineering, and other fields concerned with material response at a particulate scale (O'Sullivan 2011).

Most DEM simulations in geomechanics have been completed using commercial or open source codes. The first commercial code developed for three-dimensional DEM simulations is Trubal (Cundall and Strack 1979) and the most common three-dimensional commercial codes currently used, which are altered adaptions of and closely linked to Trubal (O'Sullivan 2011), include PFC3D and EDEM. Common open source DEM codes include LIGGGHTS, ESyS-Particle, YADE, and OVAL. The research performed here differs from most published DEM analyses in that commercial or open source code was not used, and an original discrete element model was written in Fortran coding language, and analyses were performed using capabilities of a high performance computing system. Using computationally rigorous calculations of large numbers of particles will improve the ability to predict soil behavior in the field.

A general description of the code and order of calculations during each time step is shown in
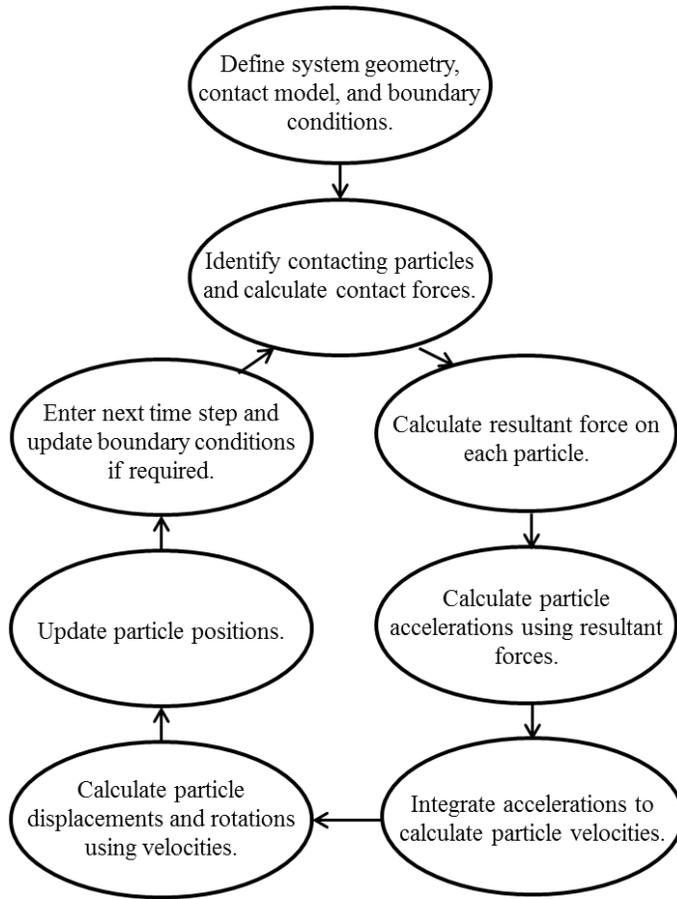
Figure 2. First, the system geometry, contact model, and boundary conditions are defined. For the

first time step, contacting particles are identified using a contact detection algorithm, and the

corresponding contact forces are calculated using the defined contact model. The resultant force

acting on each particle, including body forces and external forces, is calculated. Particle

accelerations are calculated using the resultant forces. The accelerations are integrated to

determine particle velocities. Particle displacements and rotations are calculated by integrating the

velocities. Finally, the particle positions are updated and these steps are then repeated for the next

time step where the user may need to revise the boundary positions as required. The circular arrow

path of
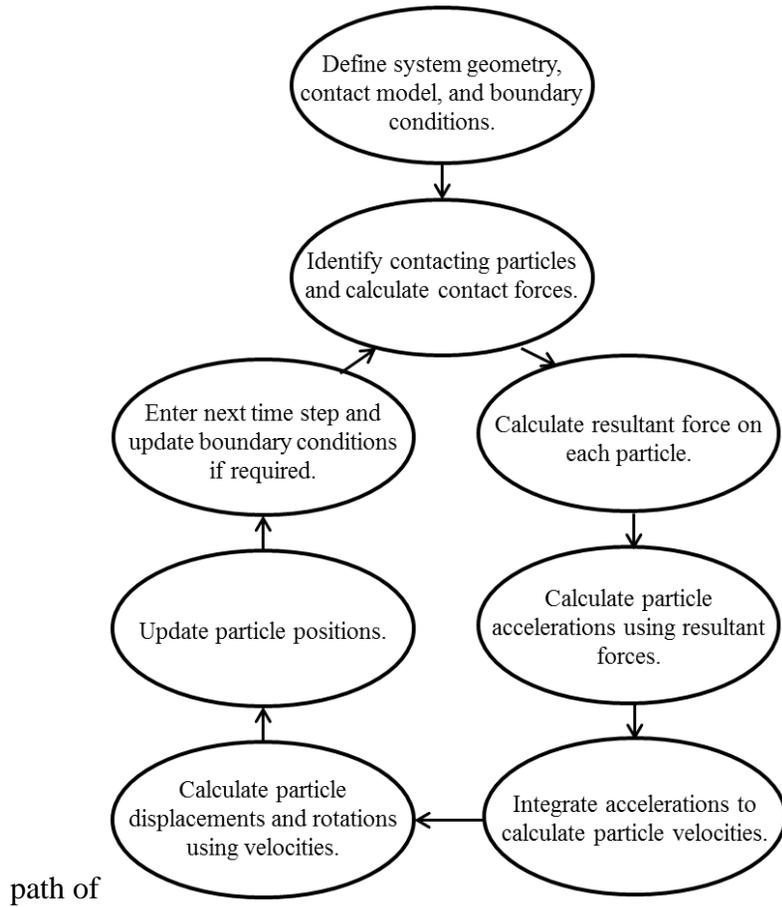
Figure 2 represents the time step process.
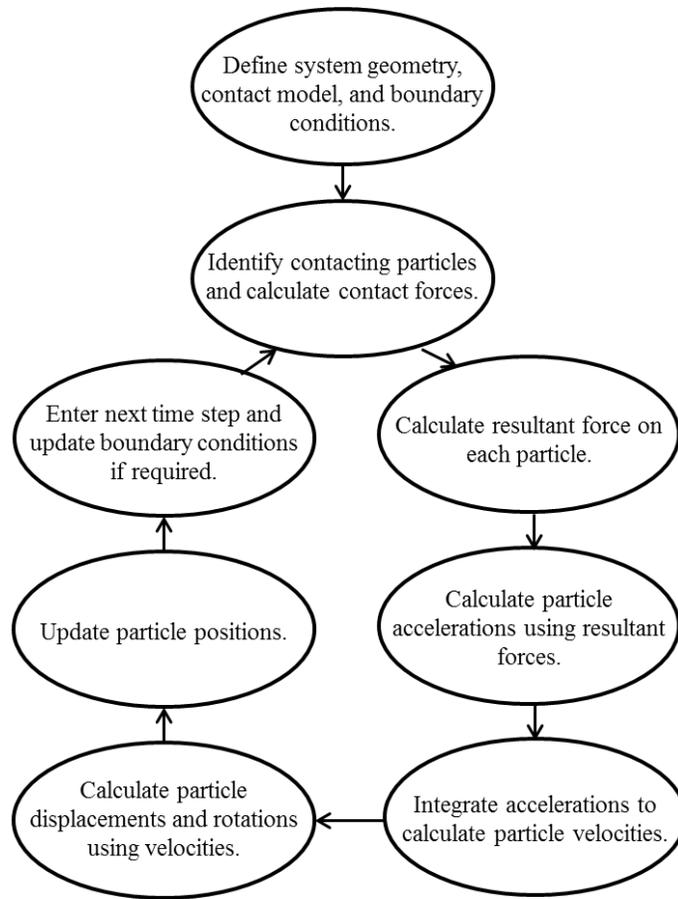
Figure 2. Illustrative representation of the calculation steps performed in a DEM simulation.

As with most numerical models, a DEM model is an idealization of a physical system; therefore, several assumptions are made to complete the analyses. As previously mentioned, computational cost is a concern for DEM analyses, so there exists a trade-off between computational cost and physical practicality. An assumption made in the DEM analyses of the research presented herein is that the particles simulated are perfectly spherical. Particle irregularities exist in natural soil; however, spheres are the simplest to use computationally because calculating if they are in contact with other spheres or with boundaries is more straight-forward. Because of the contact model chosen, another assumption made for these analyses is that the particles deform elastically. This assumption is reasonable for sand particles at low effective stress, but could cause problems for

soils with weaker particles or under high effective stress. There were other assumptions made to complete this research, but they are explicitly described herein and supported with explanations and published experimental evidence.

As has been demonstrated, DEM simulations can produce qualitatively realistic results (Thornton and Antony 2000). Also, with DEM simulations, several analyses (for example with different loadings) can be performed on the same exact initial configuration. This is not possible in laboratory experiments, where differences exist between test specimens, which may lead to difficulties when comparing test results. In DEM simulations (or any numerical simulations for that matter), these uncertainties do not occur (Thornton and Antony 2000).

1.2 Study Objectives and Project Scope

The first objective of this study was to assess the efficacy of a post-fire ground treatment in mitigating soil erosion and runoff. A laboratory-scale slope-model experiment was constructed with a rainfall simulator and the ability to measure runoff and erosion. Straw mulch was used as the post-fire ground treatment and slope-model experiments were conducted on unburned and burned block samples collected from U.S. Forest Service land in Colorado. Experiments were conducted with no straw mulch and application rates of straw mulch $= 0.06$, 0.11, and 0.22 kg/m^2. This study represents a step towards understanding the mechanisms of post-fire increases in runoff and erosion at the macro and micro scale. Results from this study will be beneficial for researchers and land managers. Although the rates and magnitudes of runoff and erosion will vary based on location and size of study plot, the mechanisms observed in this laboratory-scale study will be applicable at field-scale.

The following research tasks were completed as a part of this study to meet the first objective:

- Reviewed literature related to post-fire soil susceptibility and enhanced runoff and erosion;

- Collected in-tact block samples that were representative of ground conditions in wildfire prone areas;

- Conducted laboratory-scale slope-model experiments to evaluate the efficacy of post-fire ground treatments on mitigating erosion and runoff; and

- Evaluated effects of high severity burning on geotechnical properties of a Colorado soil.

The second objective of this study was to show that particle aggregates representing a burned soil and root developments in the aggregates can be modeled with DEM. Using DEM to simulate idealized assemblies of particles under natural root developments will shed light on soil behavior at a particulate level, resulting from the collection of all particle interactions. In turn, this can lead to a better understanding of the overall macroscopic behavior and the physical processes of soil erosion following a fire. The simulations presented at the particle level behavior that occur within the particle aggregates with no reinforcement or with fiber reinforcement, are intended to mimic root growth and reinforcement, within a particle aggregate.

The following research tasks were completed as a part of this study to meet the second objective:

- Developed a DEM model capable of performing all necessary calculations including the effects of hydraulic forces and particle reinforcements;

- Verified the accuracy of the DEM with published results from other researchers; and

- Quantified the ability of numerical reinforcements, representing natural root development, to stabilize soil slopes.

These tasks provided insight into how root reinforcements aid in stabilizing slopes at a particle aggregate level. Testing of post-fire ground treatments can be cumbersome and time consuming, whereas once a DEM model is calibrated for a particular soil, ground treatment techniques can be modeled and tested for capabilities before being implemented in the field. Using the DEM in the

future could allow for rapid assessment of the controlling parameters without having to conduct large-scale case studies or wait years for field observations. Overall, this research aimed to show that DEM has the potential to develop more cost effective and capable techniques of protecting critical infrastructure after a fire, at a lower cost, with less physical equipment, and less material than required for current testing practices.

CHAPTER 2: LABORATORY-SCALE SLOPE-MODEL EXPERIMENT

2.1 Methods and Materials

The experimental program for this study included slope-model experiments conducted under simulated rainfall and testing to assess soil characteristics and engineering properties. A summary of slope-model experiments conducted on the block samples is in

Table A. The following five scenarios were considered: (a) unburned with natural vegetation and ground litter; (b) burned without straw mulch; (c) burned with 0.06 kg/m^2 straw mulch; (d) burned with 0.11 kg/m^2 straw mulch; and (e) burned with 0.22 kg/m^2 straw mulch. All burned block samples were burned under identical conditions in the laboratory.

A summary of the soil characteristics and engineering properties evaluated and corresponding test procedures is in Table B. Soil characterization tests included particle-size distribution and Atterberg limits conducted on each of the eight grab samples, and specific gravity and compaction tests conducted on a single homogenized grab sample. Prior to each rainfall simulation on a block sample, Mini Disk Infiltrometer (MDI) and water drop penetration time (WDPT) tests were conducted. For each simulated rainfall event in a slope-model experiment, eroded sediment mass (i.e., sediment yield) and runoff volume were measured. In addition, the following three measurements were conducted for each in-tact block sample post testing: dry density, total organic carbon, and shear strength. Specimens for these tests were exhumed from the upper 6 cm of block samples after rainfall simulations using sampling procedures outlined in ASTM D7015-13 (ASTM 2013) and a thin-walled metal sampler.

31

Table A. Summary of slope-model experiments conducted on block samples.

Test Group	Scenario	Specimen Description	Straw Mulch Application (kg/m^2)	Test Specimen Replicates	Rainfall Simulations per Replicate
Block Sample	1	Unburned block	0	3	1
	2	Burned block	0	1	2
	3	Burned block	0.06	1	2
	4	Burned block	0.11	1	2
	5	Burned block	0.22	1	2

Table B. Summary of the soil characteristics and engineering properties that were evaluated and the experimental method for each.

Measurement	Method
Soil erodibility and runoff rate	Rainfall simulation
Soil characterization	Sieves, hydrometer, Atterberg limits, and specific gravity
Dry density	Mass loss by oven heating
Total organic carbon	Loss on ignition
Field saturated hydraulic conductivity	Mini Disk Infiltrometer
Water repellency	Water drop penetration test
Soil strength parameters	Drained direct shear

2.1.1 Soil Sample Collection

Soil samples were collected in Roosevelt National Forest, Colorado, in a location north of Estes Park and west of Fort Collins (coordinates: 40.56856, -105.47370). The location represented soil and vegetation conditions in Colorado that experience wildfires. Soil composition in the area was similar to soil composition at historic Colorado wildfire burn areas, which are summarized in Table C (Moody and Martin 2001; Benavides-Solorio 2001; MacDonald and Huffman 2004; Pietraszek 2006; Ebel et al. 2012; Robichaud et al. 2013). This location was also in close proximity to the

High Park Fire, which occurred in 2012. Permission to obtain soil samples from the site was granted by the U.S. Forest Service. The sampling area was chosen to avoid large roots and rocks.

Table C. Composition of soils in historic Colorado wildfire burn areas and soil collected from the block sample location.

Soil Texture	Colorado Wildfire Burn Areas			Block Sample Average (%)
	Low (%)	High (%)	Average (%)	
Gravel	0	56	25	15
Sand	23	69	47	57
Silt	6	41	23	26
Clay	0	20	6	3

Seven undisturbed block samples and eight grab samples were collected. Block samples were collected within sheet metal boxes that were 91.4-cm long, 30.5-cm wide, and 30.5-cm tall following cubical block sampling procedures outlined in ASTM D7015-13 (ASTM 2013). An 11 gauge steel box with an open top and bottom was placed on the soil surface. Soil was excavated around the box so that the box could be pressed into the ground, continually enclosing the soil sample during excavation. Once the top of the box was inserted approximately 23 cm into the soil, the base of the block was separated from the parent material. The block was then moved onto a plywood pallet. Excavation for one block sample provided a starting location for the next block sample such that all block samples were collected adjacent to one another. Grab samples were collected in 20-L buckets intermittently during excavation of the block samples (see Appendix A). Block samples were secured to the pallets used for collection and transported to CSU. The block samples were kept in a greenhouse and watered weekly to maintain healthy vegetation prior to testing.

2.1.2 Slope-Model Experiment with Simulated Rainfall

A schematic of the slope-model experiment is shown in Figure 3, which included a soil specimen container and rainfall simulator. The soil container was constructed from steel with dimensions of 76.2-cm long, 30.5-cm wide, and 30.5-cm deep. The container was designed with the ability to collect runoff and eroded sediment, drain infiltrated water from the bottom of the specimen, adjust slope of the specimen, and adjust location of the outflow plate. A non-woven geotextile was placed along the bottom of the soil container to allow drainage from the bottom of the specimen. To prevent sidewall water flow along the container-soil interface, bentonite paste (bentonite and water mixed at a ratio of 1:6) was placed around the specimen perimeter to a depth of 2.5 cm (Lee et al. 2010). If applicable, ground treatments were applied to soil specimens prior to rainfall simulations. Rainfall was applied to the soil specimens with a rainfall simulator designed based on Regmi and Thompson (2000). A schematic of the soil rainfall simulator is shown in Figure 3. Each raindrop former was a telescopic arrangement of a 21-ga. capillary tube inside a 9-ga. capillary tube. A total of 140 raindrop formers were spaced in an equilateral triangular grid on the bottom of the rainfall simulator. A stainless steel raindrop distribution screen was placed 71 cm below the raindrop formers to create a broader distribution of raindrop sizes that were representative of natural rainfall. Rainfall intensity was controlled by adjusting the head of water above the raindrop formers. Water was primarily low-ionic-strength snowmelt runoff with pH between 6.8 and 7.3 and an electrical conductivity between 4 to 8 mS/m (Larsen et al. 2009). The height between the bottom of the rainfall simulator and soil specimen container was 7.6 m (25 ft.), which allowed raindrops ≤ 2 mm in diameter to reach 95% of terminal velocity. The laboratory-scale slope-model experiment yielded repeatable measurements of sediment yield and runoff for replicate tests conducted on sand-silt mixtures (see Appendix B).
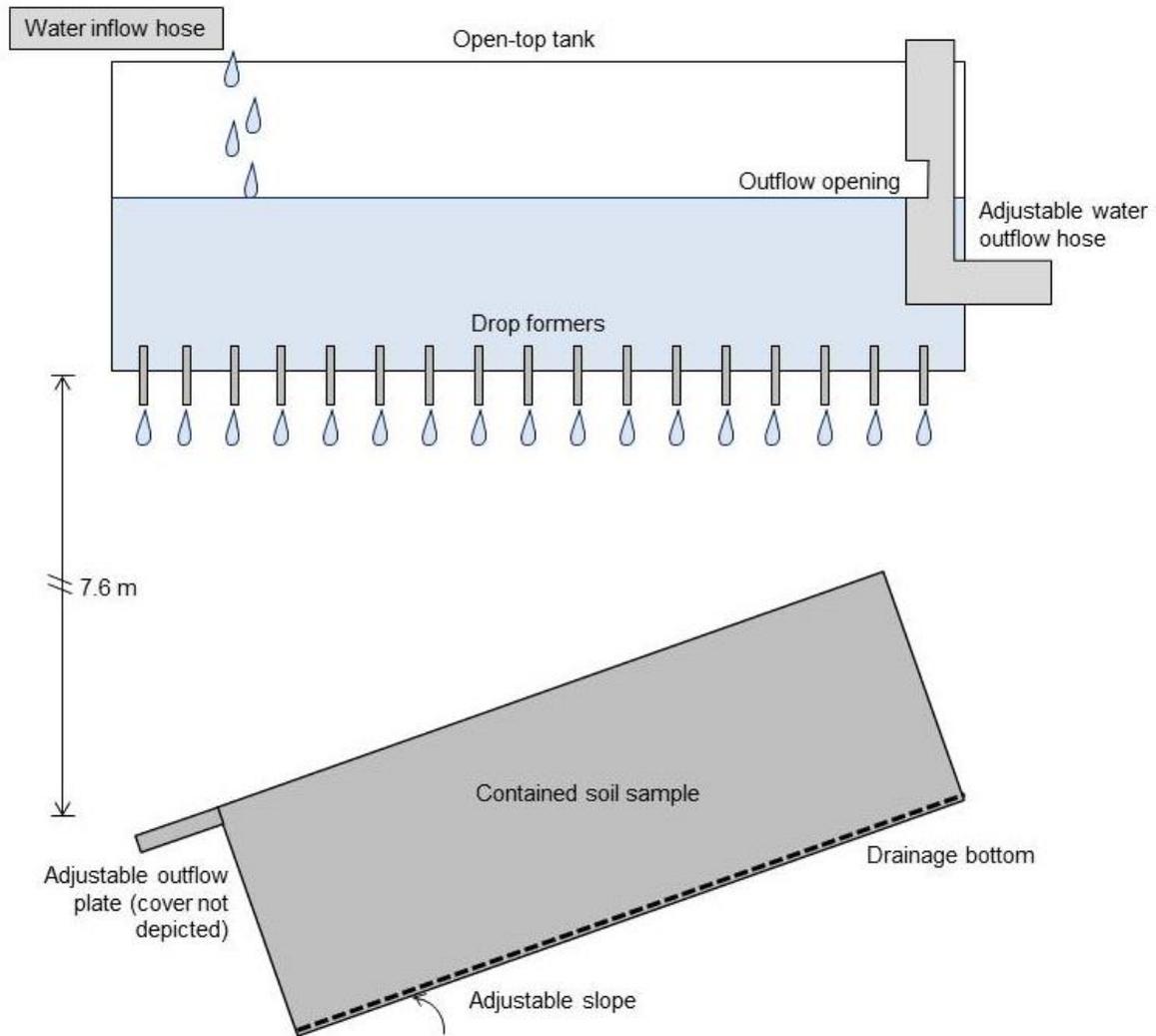
Figure 3. Schematic of the rainfall simulator (top) and soil container (bottom) used to conduct the slope-model experiments.

A summary of observed or simulated rainfall that produced runoff and erosion from burned Colorado hillslopes is in

Table D. Relationships of rainfall intensity versus rainfall duration from 23 Colorado Front Range NOAA weather stations are shown in Figure 4. In this study, rainfall was simulated at an intensity of approximately 48 mm/h and experiments were conducted for 40 min. The rainfall intensity and duration were chosen to replicate a typical short-duration, high-intensity summer storm in

Colorado that can lead to runoff and erosion on burned hillslopes (Robichaud and Brown 2005; Cannon et al. 2008; Larsen et al. 2009; Moody and Martin 2009; Foltz and Wagenbrenner 2010). A rainfall event in Colorado's Front Range that is comparable to what was simulated in this study has a return period of 25 yr. The rainfall generator was calibrated prior to testing to determine the target rainfall intensity and the intensity applied during a given experiment was measured at the start and end of each experiment. Successive rainfall simulations conducted on a single specimen were conducted three days apart to allow for potential soil crust formation (Larsen et al. 2009).

Table D. References and locations of observed or simulated rainfall that produced runoff and sediment yield. Rainfall parameters include recurrence interval, storm duration, and storm magnitude.

Reference	*Location*	*Recurrence Interval (yr)*	*Storm Duration (min)*	*Storm Magnitude (mm/h)*
---	High Park Fire BAER	10	60	38
Robichaud et al. (2012)	Intermountain West	50	15	50
Foltz and Wagenbrenner (2010)	Intermountain West	50	25	51
Cannon et al. (2008)	Colorado [a]	< 2	< 180	1-32
Robichaud and Brown (2005)	Colorado Bobcat Fire [b]	5-10	30	48
Murphy et al. (2012)	Fourmile Creek Fire [b]	---	30	46
Moody and Martin (2009)	Plains rainfall regime	2	30	19-52
Verdin et al. (2012)	High Park Burn Area 1	2	60	25
Verdin et al. (2012)	High Park Burn Area 2	10	60	43
Verdin et al. (2012)	High Park Burn Area 3	25	60	51

[a] Debris flows that were produced from 25 recently burned basins in Colorado in response to 13 short-duration, high-intensity convective storms
[b] Actual storm event producing high sediment yields

Block samples were transferred from the metal collection boxes to the soil specimen container located beneath the rainfall simulator. The soil specimen container (Figure 3) was then fixed at a slope of 27° for all experiments, which was representative of burned Colorado hillslopes that have produced runoff and erosion (Pietraszek 2006; Schmeer 2014). Plastic splashguards were placed

on either side of the specimen parallel to the direction of slope to minimize loss of soil upon raindrop impact. Runoff, along with entrained sediment that had been eroded, was collected at the lower end of the soil specimen every five to ten minutes in 1.0-L bottles. The total water and sediment collected at each interval was weighed and then dried in an oven at 105 °C for 24 h. The eroded sediment mass (i.e., sediment yield) at each interval was the mass of sediment after drying. The runoff at each interval was taken to be the total mass collected minus the mass of eroded sediment, assuming the density of water = 1 g/cm^3.
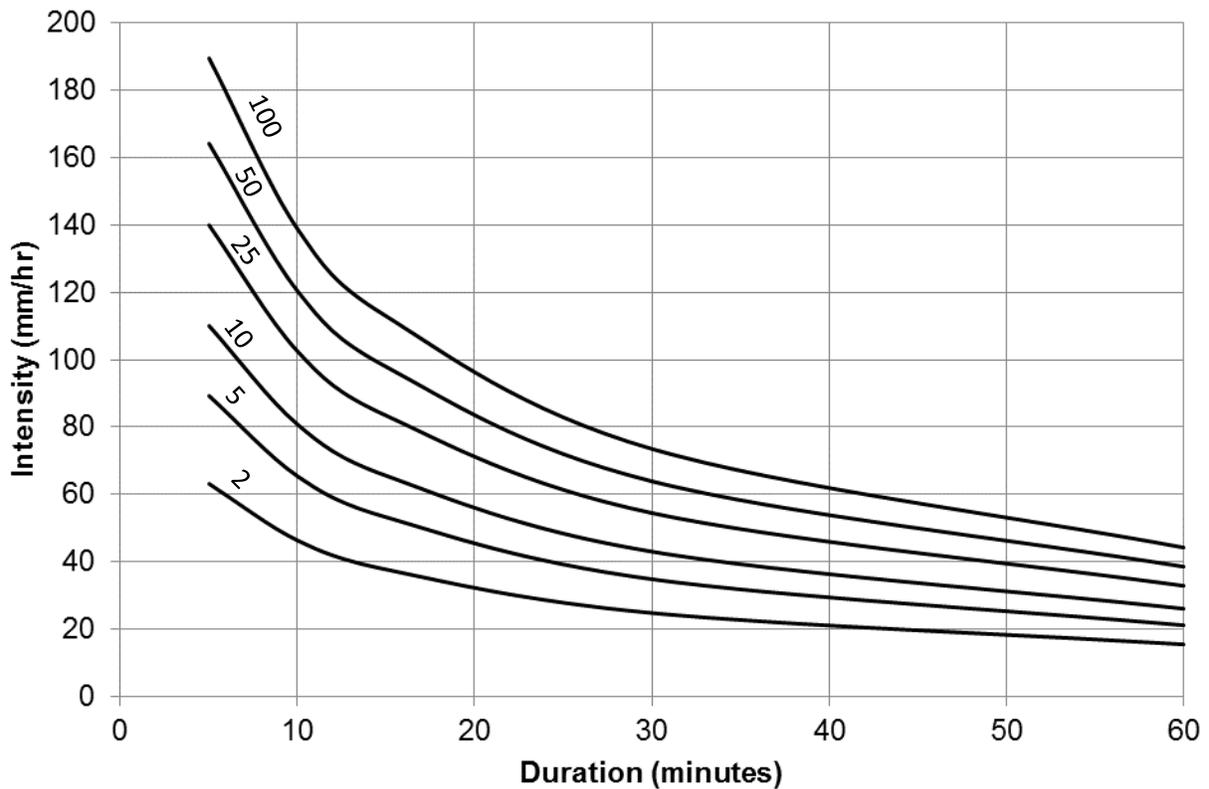
Figure 4. Intensity-duration-frequency (IDF) plot based on average annual maxima data from 23 Colorado Front Range weather stations where each data series represents a return interval in years.

2.1.3 Burn Simulation

Block samples were burned under controlled conditions to replicate a moderate to high soil-burn severity. Previous laboratory studies have shown that the hydrophobic layer in the soil subsurface is intensified at temperatures from 175 to 250 °C (DeBano and Krammes 1966; Doerr et al. 2000; Robichaud and Hungerford 2000; Zavala et al. 2010). These temperatures also correspond to a moderate to high soil-burn severity (Zavala et al. 2010). Prior to burning, the block samples were air-dried for 1 week to promote post-burning water repellency at shallow depths following recommendations in Robichaud and Hungerford (2000).

Hardwood lump charcoal was ignited and placed on a foil-lined, perforated metal sheet elevated 2.5 cm above the soil surface. Newly ignited charcoal was added to the metal sheet every 20 min until the soil at a depth of 2 cm from the surface reached 200 °C. The bottom and sides of the block sample were wrapped in an insulating fabric to promote soil heating from the surface down. The soil temperature 2 cm below the surface was monitored in real time using an Omega Type K thermocouple connected to a computer. Burning the soil using this approach required approximately 120 min to reach the target soil temperature (see Appendix C).

2.1.4 Block Samples Tested

A summary of the slope-model experiments conducted on burned and unburned block samples is in

Table A. Photographs of test specimens prepared from three unburned block samples with varying levels of vegetation and from four burned block samples with and without straw mulch as ground

cover are shown in Figure 5. The three unburned block samples were observed to have different amounts of vegetation and ground litter. These visual differences in surface cover were qualitatively described as low, medium, and high vegetation, where vegetation is used to imply intact surface vegetation and surface litter.
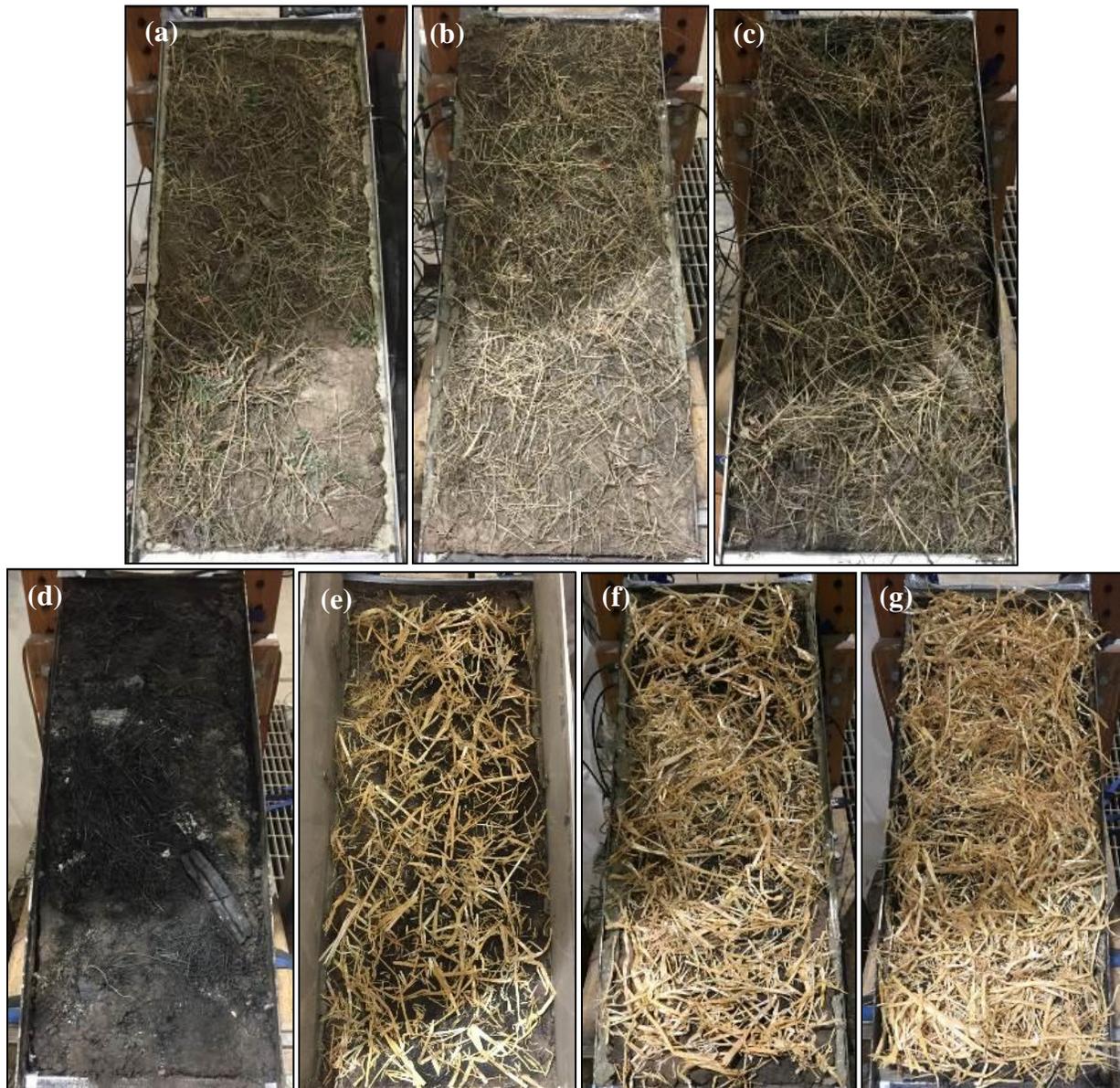
Figure 5. Pre-rainfall simulation pictures of (a) low vegetation, unburned block, (b) medium vegetation, unburned block, (c) high vegetation, unburned block, (d) burned block, no straw mulch, (e) burned block, 0.06 kg/m^2 straw mulch, (f) burned block, 0.11 kg/m^2, and (g) burned block, 0.22 kg/m^2.

Straw mulch was applied to burned soil samples by hand, if applicable, prior to the first rainfall simulation. A straw mulch application rate of 0.22 kg/m^2 is commonly used as a post-fire ground treatment by BAER on Colorado hillslopes (Robichaud et al. 2000; BAER 2012). The straw mulch application rates of 0.06 and 0.11 kg/m^2 were evaluated to explore how reducing ground cover influenced runoff and erosion. Burroughs and King (1989) provided an equation to estimate the percent ground cover from mulch applications, whereby straw mulch application rates of 0.06, 0.11, and 0.22 kg/m^2 corresponded to ground cover percentages of approximately 40%, 50%, and 65%. However, the percent ground cover visually appeared higher (Figure 5) than those predicted using the equation in Burroughs and King (1989).

Three replicates were considered for the unburned scenario, and one replicate was considered for each burned scenario. A rainfall simulation was conducted on each unburned specimen prior to burning. Subsequent rainfall simulations were then conducted on burned specimens with the varying amounts of straw mulch (i.e., no cover to 0.22 kg/m^2). For each burned scenario, two rainfall simulations were conducted three days apart to explore changes in soil hydraulic properties due to potential soil crust formation. Pictures of the test specimens in the slope-model experiments before and after each rainfall simulation are in Appendix D.

2.1.5 Soil Characteristic and Engineering Property Tests

A summary of geotechnical characteristics measured on the eight grab samples collected from the field is in Table E. Particle-size distribution by sieve and hydrometer analyses (ASTM D6913-04 2009; ASTM D7928-16 2016) and Atterberg limits (ASTM D4318-10 2010) were conducted on each of the eight grab samples. Particle-size distribution curves for the eight grab samples and the average particle-size distribution curve are shown in **Error! Reference source not found.**. The eight samples yielded similar percent composition of gravel, sand, silt, and clay particles, and the

soil classified as silty sand (SM) according to the Unified Soil Classification System. An equal

mass of each grab sample was mixed together to create a representative, homogenized soil sample

to assess specific gravity (ASTM D854-14 2014) and standard compaction (ASTM D698-12

2012).

Table E. Summary of soil characteristics determined on the grab samples.

Characteristic	Soil sample [a]
Gravel (%)	15 ± 3
Sand (%)	57 ± 2
Silt (%)	26 ± 3
Clay (%)	3 ± 1
Specific gravity	2.69
Plastic limit	1 ± 1
Max dry unit weight (kN/m^3)	16.4
Optimum gravimetric water content (%)	18

[a] Characteristics presented as $X \pm Y$: X = average and Y = standard
deviation based on samples analyzed from each of the eight grab samples
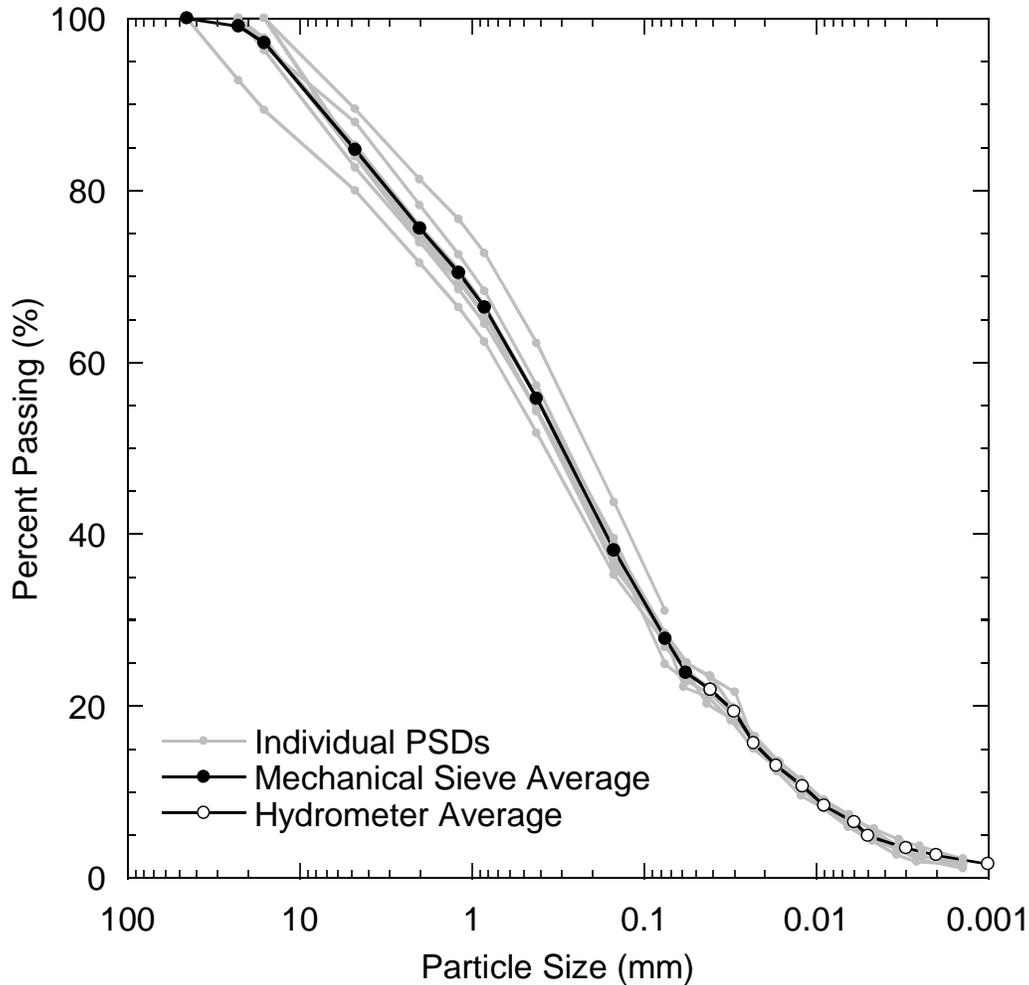
Geotechnical testing also was conducted on unburned and burned soil samples to analyze the effect of burning on physical characteristics and hydraulic and mechanical properties. Changes in physical characteristics due to burning were analyzed by measuring dry density and total organic carbon. Changes in hydraulic properties due to burning were analyzed by measuring field saturated hydraulic conductivity and water repellency. Changes in mechanical properties due to burning were analyzed by measuring shear strength via direct shear. Unburned soil specimens were trimmed from block samples prior to rainfall simulations. Burned soil specimens were collected from burned block samples after rainfall simulations were complete.

Dry density and total organic carbon (TOC) were assessed on the upper 6 cm of block samples following sampling procedures outlined in ASTM D7015-13 (ASTM 2013) with a thin-walled metal sampler. Dry density was assessed on unburned and burned soil following ASTM D7263-09. A moist soil specimen was weighed, dried in a ceramic crucible at 105 °C for 24 h, and then re-weighed.

Total organic carbon was estimated using the loss-on-ignition (LOI) method. The LOI method involves the heated destruction of all organic matter in a soil specimen. A moist soil specimen was weighed and dried in a ceramic crucible at 105 °C for 24 h. The dry soil was then re-weighed and heated to 440 °C for 24 h. The specimen was then cooled in a desiccator and weighed again. Organic matter content was calculated as the difference between the initial and final dry masses divided by the initial dry mass. Furnace temperature for the LOI method was maintained below 450 °C to avoid destruction of any inorganic carbonates that may be present in the soil (Schumacher 2002).

A mini-disk infiltrometer (MDI) was used to estimate the field saturated hydraulic conductivity (Decagon Devices). The MDI was placed on the soil surface after removing duff material from the unburned samples or ash from the burned samples. A negative pressure head of 0.5 cm was applied at the soil surface to promote water infiltration. Measurements of volumetric inflow versus time were recorded every 30 s for 15 min and then every minute until at least 15 mL of water infiltrated into the soil (Decagon Devices).

Field saturated hydraulic conductivity was calculated from the MDI data using a method proposed by Zhang (1997). Cumulative infiltration volume (I) versus time (t) was calculated using the following equation:

$$I = C_1 t + C_2 \sqrt{t} \hspace{3cm} \textbf{[Equation 1]}$$

where C_1 and C_2 are parameters related to hydraulic conductivity and soil sorptivity, respectively. Field saturated hydraulic conductivity (K_{fs}) was then calculated as

$$K_{fs} = \frac{C_1}{A} \qquad \qquad \textbf{[Equation 2]}$$

where A is a van Genuchten parameter obtained from the instrument manual based on soil type and suction height. The MDI tests were conducted on block samples that had not been exposed to water for three days.

The water drop penetration time (WDPT) method was used to measure soil surface water repellency. The WDPT method is used widely as an indicator for determining the persistence of water repellency (Doerr et al. 2004), and was performed in conjunction with the MDI test.

Duff material was removed from the unburned and burned block sample surfaces in the area where the experiment was conducted. One droplet ($\approx$ 80 µL) of de-ionized water was placed on the soil surface. The time required for the water droplet to infiltrate the soil was recorded. Repellency class intervals and associated ratings are summarized in

Table F. Penetration times greater than 5 s were recorded in 20 s intervals for the first 600 s, and then every 30 min. The WDPT tests were terminated after 5 h if a water drop had not penetrated (Doerr et al. 2004).

Table F. Water drop penetration time (WDPT) class increments and corresponding descriptive repellency rating (Doerr et al. 2004).

WDPT classes (s)	≤5	> 5, 20, 40, 60	80 - 600	> 600 - 3600	> 3600
Repellency rating	Wettable	Slight	Strong	Severe	Extreme

Direct shear tests were conducted under drained conditions on unburned and burned specimens following ASTM D3080. Intact specimens were collected from the upper 6 cm of the block samples using sampling procedures outlined in ASTM D7015-13 (ASTM 2013) with a thin-walled

metal sampler. Specimens with a diameter of 64 mm and height of 33 mm were cut from the block samples and transferred to a circular direct shear box. Direct shear testing was conducted under effective normal stresses (σ'_n) of 17, 34, and 65 kPa, which were reasonably low stresses that could be applied in the direct shear apparatus to assess shear strength of the surficial soil deposit. Specimens were inundated for 2 h immediately following application of normal stress. Drainage was permitted through porous metal disks and filter paper placed on the top and bottom of the specimens. Tests were conducted at a displacement rate of 0.08 mm/min using an ELE International Digital Shear Machine. Measurements of horizontal displacement, vertical displacement, and shear force were recorded every second using a National Instruments data acquisition card (NI USB-6009, 192256A-01), LABView software, and a laptop computer. Two linear variable displacement transducers (Novotechnik Models TR-0050 and TR-0025) were used to measure horizontal and vertical displacements. A load cell (Interface Force Transducer Model SSM-AJ-500) was used to measure shear force. Direct shear specimens were inspected post shearing to note if any gravel-sized particles were present within the shear plane.

Peak shear strengths were used to develop strength envelopes if a peak shear stress was observed in the shear-displacement data. Alternatively, the shear stress at 7 mm of horizontal displacement was selected as the shear strength for development of a strength envelope in the event peak shear strength was not observed.

2.2 Rainfall Simulation Results

A summary of the rate of simulated rainfall, average runoff rate, ultimate runoff rate, and average percent runoff for the three unburned block samples and four burned block samples tested in the slope-model experiment is in Table G. Average rainfall intensity for all rainfall simulations was 48 ± 2 mm/h. The average runoff rate was calculated as the total runoff collected during the

simulated rainfall over the 40-min rainfall duration. The ultimate runoff rate was calculated as the runoff collected during the last 5 min of the simulated rainfall, which was approaching a constant runoff rate in all experiments. Average percent runoff was computed as the percent of cumulative precipitation falling on a soil specimen that resulted in runoff. Cumulative precipitation falling on a given specimen was computed based on surface area of the specimen, rainfall intensity, and duration of rainfall. Average infiltration capacities for unburned and burned soils (estimated using MDI) were less than the rainfall rate, which indicated that infiltration excess surface runoff occurred during the rainfall simulations. Infiltration excess runoff is common during short duration, high intensity rainstorms analogous to the storm simulated in this study.

Table G. Rate of simulated rainfall, average runoff rate, ultimate runoff rate, and average percent runoff for unburned and burned block samples tested in the slope-model experiment.

Condition	Rainfall Simulation	Cover/ Straw Mulch (kg/m^2)	Rainfall Rate (mm/h)	Average Runoff Rate (mm/h)	Ultimate Runoff Rate (mm/h)	Percent Runoff (%)
Unburned block	1st	Low vegetation	48	24	32	50
		Medium vegetation	48	13	22	27
		High vegetation	47	11	18	23
Burned block	1st	0	48	15	25	31
		0.06	49	20	23	41

		0.11	49	9	17	18
		0.22	50	11	20	22
	2nd	0	47	21	29	45
		0.06	49	21	23	43
		0.11	49	14	18	29
		0.22	46	11	16	24

2.2.1 Effect of Burning on Runoff and Erosion

Temporal trends of runoff rate and sediment concentration from the slope-model experiments on the three block samples with intact natural vegetation and the one burned block sample with no ground cover are shown in Figure 6. Runoff rate was computed incrementally as the volume of runoff occurring between subsequent measurements divided by specimen surface area and elapsed time. Sediment concentration was computed as the ratio of sediment yield to runoff between subsequent measurements.

The rate of runoff increased during the first 20-25 min of simulated rainfall for the burned soil and three soil specimens with natural vegetation, and subsequently approached an approximately consistent rate (i.e., ultimate runoff rate). The presence of natural vegetation directly influenced runoff, whereby the low vegetation, unburned specimen had the highest amount of runoff (50% of total rainfall), and the amount of runoff decreased with an increase in the amount of surface vegetation (Table G, Figure 6a). The amount of runoff measured for the burned soil with no ground cover was between the cumulative runoff measured on the medium and high vegetation block samples. The amount of runoff for the burned block sample was attributed to a wettable ash layer on the burned soil surface that acted as a water storage layer. Thus, during the first rainfall simulation the ash layer had the capacity to store precipitation since this ash layer was dry at the start of the rainfall simulation.

47
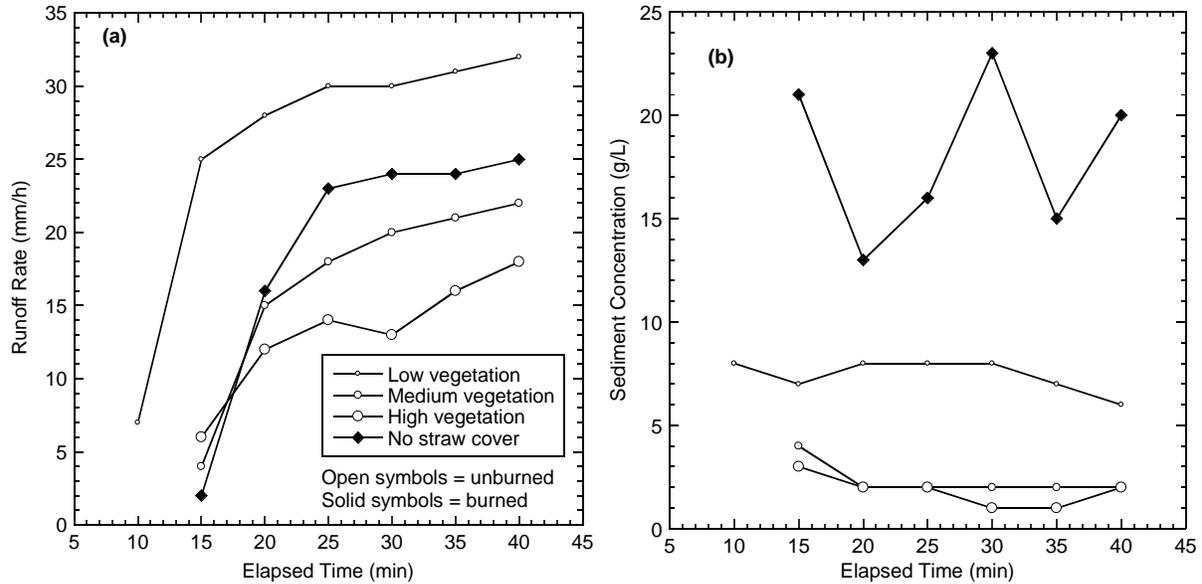
Figure 6. Temporal relationships of (a) runoff rate and (b) sediment concentration for slope-model experiments conducted on three unburned block samples and one burned block sample with no straw mulch cover.

In contrast to similarities in runoff between unburned and burned block samples, the amount of erosion was considerably higher for the burned block sample (Figure 6b). The amount of sediment eroded from the burned block sample increased by at least a factor of two relative to the low vegetation specimen and nearly an order of magnitude relative to specimens with medium and high vegetation (Figure 6b). Although vegetation and bare areas on unburned soil surfaces can convey surface flow as runoff, the surface vegetation and corresponding root network helps protect the soil surface from raindrop impact and subsequent particle entrainment during runoff. Vegetation also aids to trap dislodged sediment or at least impede downslope movement, which reduces the amount of erosion. Soil particles on the burned soil surface with no ground cover were fully exposed to erosive forces of raindrop impact and surface water flow. Thus, the greater ability for soil particles to dislodge and transport on the burned soil surface increased erosion relative to the unburned block samples.

2.2.2 *Effect of Straw Mulch on Runoff and Erosion*

Temporal trends of runoff rate and sediment concentration measured in the slope-model experiments conducted on the four burned block samples with varying amounts of straw mulch are shown in

Figure **7**. The presence of straw mulch was observed to directly influence the amount of runoff during the first and second rainfall simulations (Table G,

Figure **7**a and

Figure **7**b). The amount of runoff generally decreased with an increase in the amount of straw mulch. Runoff measured for the burned block samples with 0.11 and 0.22 kg/m^2 straw mulch was approximately the same as the cumulative runoff measured on the high surface vegetation block sample (

Figure **7**a). Also observed in the runoff measurements was an increase in the amount of runoff for the second rainfall simulation on the burned soil sample without ground treatment and with the burned soil samples with 0.06 and 0.11 kg/m^2 straw mulch. However, magnitude of the runoff increased from the first to second rainfall simulation and was highest for the burned sample without straw mulch. The straw mulch applied to the burned samples protected the ash layer from rainfall induced erosion, allowing the ash layer to continue to provide water storage during the second rainfall simulation.

◆ No straw cover	▫ 0.06 kg/m2 straw cover	▫ 0.11 kg/m2 straw cover	▫ 0.22 kg/m2 straw cover
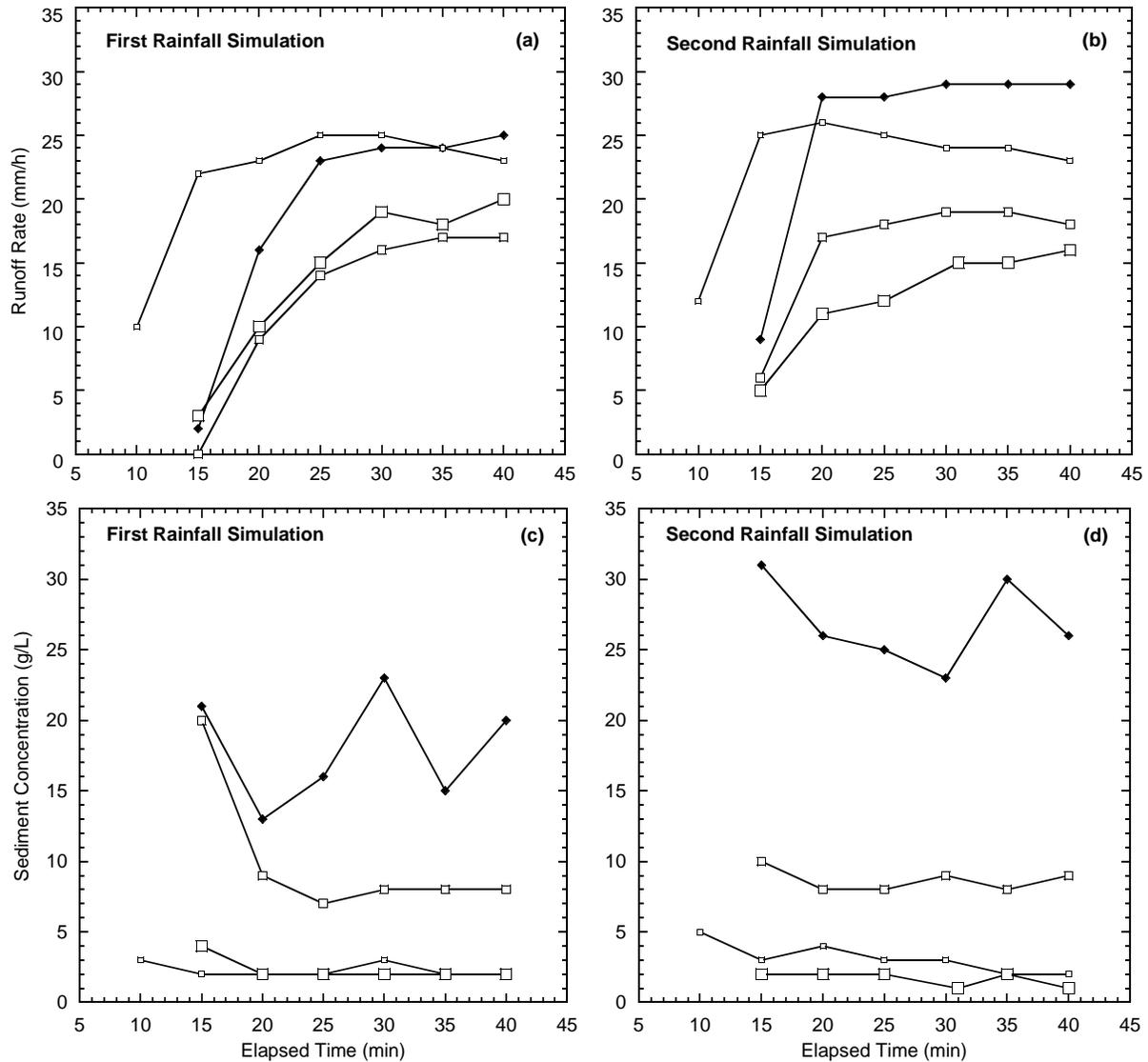
Figure 7. Temporal trends of runoff rate for the (a) first rainfall simulation and (b) second rainfall simulation, and temporal trends of sediment concentration for the (c) first rainfall simulation and (d) second rainfall simulation from the slope-model experiments conducted on the burned block samples with varying amounts of straw mulch.

The ultimate runoff rate generally decreased with increasing ground cover, whether the ground cover was natural vegetation or straw mulch (Table G). A water balance analysis was conducted for each soil specimen during a given rainfall simulation. Water entering the system (i.e., a soil specimen) was simulated rainfall, and water leaving the system was in the form of infiltration, surface runoff, or water absorbed by surface cover. Burned block samples were exposed to similar

rainfall rates and had similar infiltration capacities (discussed subsequently), and yet exhibited varying runoff rates. Straw mulch increased surface roughness for overland flow, which slowed down runoff and allowed more time for infiltration. Considering that runoff developed due to infiltration excess, increasing the amount of straw mulch decreased runoff rates by allowing more time for the water to infiltrate the soil. Straw mulch also reduced runoff by absorbing and storing water; however, this likely wasn't a major factor in runoff reduction. Based on the water absorption capacity of the straw mulch, the maximum amount of water the straw mulch could absorb was 1-4% of the total rainfall, depending on the rate of straw mulch application.

The amount of sediment eroded from the burned block sample with no straw mulch increased by a factor of seven relative to the burned samples with 0.06 and 0.11 kg/m^2 straw mulch and over an order of magnitude relative to the burned sample with 0.22 kg/m^2 straw mulch (

Figure **7**c and

Figure **7**d). In addition, sediment concentration measured on the burned block sampled increased from the first to the second rainfall simulation, whereas sediment concentration was approximately constant between the two rainfall simulations for the burned block samples with ground cover. The straw mulch used as ground cover acted similar to vegetation on the unburned samples in mitigating erosion. The straw mulch protected the burned soil surface from raindrop impact and provided an alternative flow path of water versus directly along the soil surface. Straw mulch also helped dissipate energy from raindrop impact, which reduced the potential for particle detachment. Dislodged particles were able to be trapped by the straw strands, which prevented the particles from being carried by water further downslope.

Temporal trends of the ratio of runoff rates during the second simulated rainfall (Q_2) to runoff rates during the first simulated rainfall (Q_1) for the four burned samples with varying amounts of straw

mulch are shown in Figure 8. Runoff rates during the first 20 min of the rainfall simulation increased considerably for the second rainfall simulation compared to the first simulation for burned block samples with no straw mulch and 0.11 kg/m^2 straw mulch. However, runoff rates for the second rainfall simulation when compared to the first simulation remained nearly the same for the burned samples with 0.06 and 0.22 kg/m^2 straw mulch, and Q_2/Q_1 for the 0.11 kg/m^2 sample was about 1.0 by the end of the rainfall simulation.
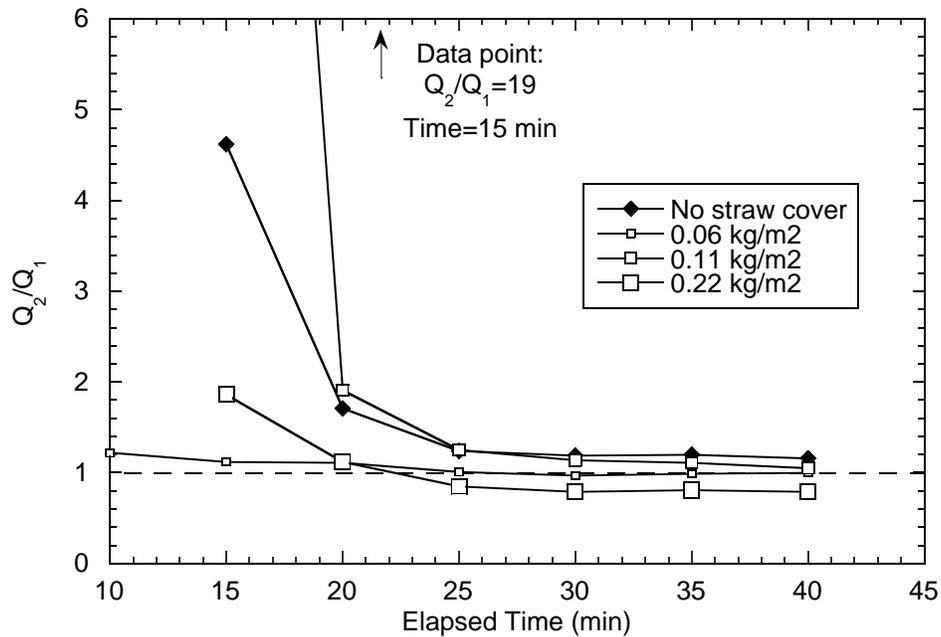
Figure 8. Temporal trends of the ratio of cumulative runoff during the second simulated rainfall (Q_2) to cumulative runoff during the first simulated rainfall (Q_1) for four burned samples with varying amounts of straw mulch application.

The increase in runoff for the second rainfall simulations was attributed to (i) an increase in soil saturation near the surface that decreased available soil water storage, and (ii) the development of soil hydrophobicity. Post-testing analysis on all four burned samples revealed a hydrophobic layer had formed 2 cm below the soil surface (classified as "extreme" using WDPT method). The hydrophobic layer inhibited infiltration, which resulted in a nearly saturated surface layer after the

first simulation and start of the second rainfall simulation. The high degree of saturation in the surficial soil was qualitative and determined visually. The nearly saturated surface soil had limited available soil water storage during the second rainfall simulation, which increased runoff from the soil surface. The magnitude of the difference in runoff and erosion from the first rainfall simulation to the second was largest for the burned block sample with no straw and generally decreased with increasing straw mulch application rate. This was attributed to increased erosion of the wettable ash layer with decreasing cover as exposure to the erosive forces of raindrop impact and surface runoff increased. Erosion and subsequent removal of the ash layer reduced water storage provided by the ash layer (Woods and Balfour 2008).

Total sediment yield from successive rainfall simulations in the slope-model experiments on the four burned samples with varying amounts of straw mulch are shown in Figure 9. Also included in Figure 9 is the range of total sediment yield from the three unburned block samples with varying amount of surface vegetation. The addition of straw mulch to the surface of burned soil exponentially decreased the total eroded sediment during a rainfall simulation. All three straw mulch application rates (0.06, 0.11, and 0.22 kg/m^2) reduced total sediment yield to levels comparable with unburned samples. Erosion generally increased with successive rainfalls on burned samples, which was attributed to an increase in surface runoff (Figure 8). However, the addition of straw mulch considerably reduced the difference between sediment yields measured for successive rainfall simulations when compared to the burned block sample with no ground cover. An increase in the amount of straw mulch applied to the surface of burned soil provided protection from erosive forces and was effective in decreasing erosion.
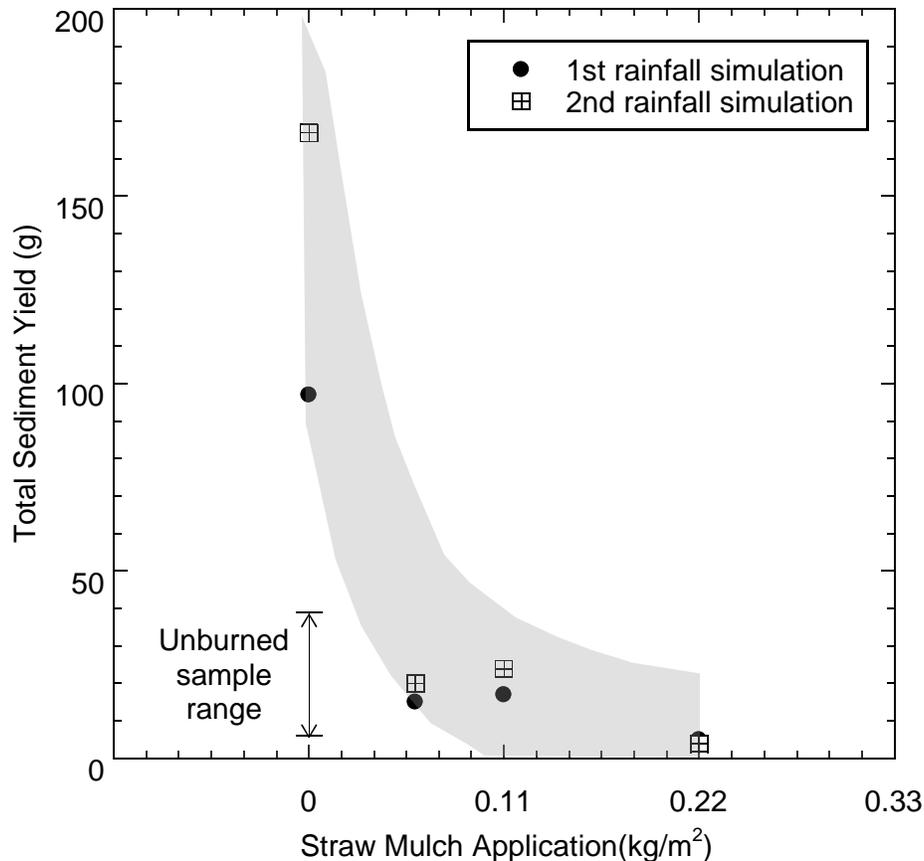
Figure 9. Relationships of total sediment versus straw mulch application for successive simulated rainfalls on four burned samples with different amounts of straw mulch. Range of sediment yield included from the unburned samples with natural vegetation.

A scatter plot of sediment yield versus percent runoff for all rainfall simulations on unburned and burned block samples is shown in Figure 10. Unburned block samples with vegetation and burned block samples with straw mulch exhibited a similar trend of low sediment yield despite increasing percent runoff, which is depicted by the shaded area in Figure 10. However, burned block samples with no straw mulch exhibited a trend of increasing sediment yield with increasing percent runoff. Although the trend identified in this study was only based on two measurements, a similar trend was observed by Wood and Balfour (2008), wherein sediment yield in burned plots with and without ash were positively correlated with runoff. The results suggest that straw mulch can prevent runoff from dislodging and transporting soil similar to vegetation on unburned soil. Results

also suggest that for a given percent runoff, eroded sediment will be higher for burned soil with no straw mulch compared to burned soil with straw mulch. Comparing the two burned block samples that yielded approximately 45% runoff, the burned sample with straw mulch decreased sediment yield nearly an order of magnitude relative to the burned sample with no ground cover.
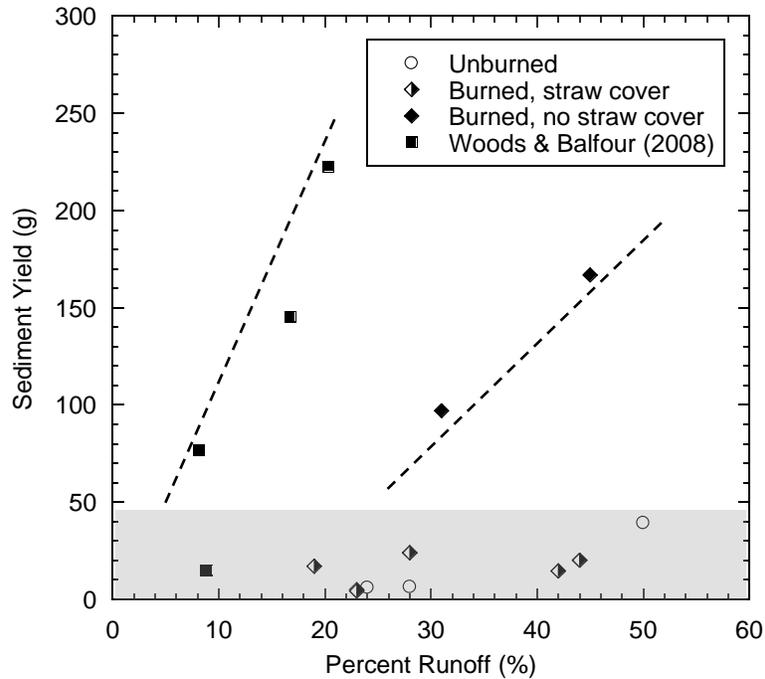
Figure 10. Scatter plot of sediment yield vs. percent runoff for all rainfall simulations on unburned and burned block samples. Burned soil, no cover data from Woods and Balfour (2008) was included to build on the trend observed for the burned soil, no cover data from this study.

2.2.3 Comparison to Previous Studies

A compilation of runoff rate, runoff reduction, sediment concentration, and sediment concentration reduction for soils with and without ground treatments are summarized in Table H. The runoff reductions and sediment concentration reductions were computed for soils with ground treatments relative tests on the same soil without ground treatment. All soils were sandy loam (SL) or silty

sand (SM) tested in similar physical laboratory models with simulated rainfall. Runoff and sediment yield were determined from the referenced studies and this study after an elapsed time of 25-min of simulated rainfall to provide consistency between all studies. Runoff reduction (RR) was calculated using the following equation:

$$RR = \frac{(T-B)}{B} \qquad \qquad \text{[Equation 3]}$$

where T and B are the runoff rates at 25 min of simulated rainfall from the treated sample (T) and bare sample (B), respectively.

Yanosek (2006) and Foltz and Copeland (2009) reported high runoff rates from unburned soils. For all studies, the addition of mulch generally reduced runoff for unburned and burned soils. Wood mulch appeared to be more effective at runoff reduction compared to agricultural straw mulch; however, making direct comparisons between studies is difficult due to differences in several variables. Both wood and straw mulch appeared equally effective at sediment concentration reduction. The mass of straw mulch used was 42-95% less than the mass of wood mulches used, suggesting straw mulch can provide similar erosion reduction at a lower cost. Yanosek (2006) suggested that the reduction in runoff, rilling, and erosion with the addition of wood strands was due to the strands slowing down water flow, which reduced shear forces of water against the soil. These observations made by Yanosek (2006) are similar to observations made in this study regarding the mechanisms of how ground cover on the surface of burned soil decreased soil erosion.

Table H. Compilation of runoff rate, runoff reduction, sediment concentration, and sediment concentration reduction from treated samples with respect to bare samples for laboratory slope-model experiments of sandy loam (SL) or silty sand (SM) soils with different ground treatments after 25-min of simulated rainfall.

Study	Soil	Slope (%)	Rainfall Intensity (mm/h)	Cover Mass (kg/m^2)	Cover Material	Runoff Rate (mm/h)	Runoff Reduction (%)	Sediment Conc. (g/L)	Sediment Conc. Reduction (%)
This study [a]	SM, unburned	50	48	0	Bare	21		4	
	SM, burned	50	48	0	Bare	23		16	
				0.06	Straw	25	- 9 [b]	2	88
				0.11		14	39	7	56
				0.22		15	35	2	88
Yanosek (2006) [c]	SL, unburned	30	50	0	Bare	31			
				0.38	Wood strand	14	55		66 [d]
Foltz and Copeland (2009) [c]	SL, unburned	30	50	0	Bare	28			
				0.49	Wood shred	8	71		74 [d]
Foltz and Wagenbrenner (2010) [c]	SL, burned	40	51	0	Bare	12			
				0.64	ASIS wood	4	67		82 [d]
				1.12	ASIS wood	3	75		95 [d]

[a] Runoff rate and runoff reduction for first rainfall simulation

[b] Negative value indicates increase in runoff when compared to bare sample

[c] Runoff rates and sediment concentrations after 15-min of simulated rainfall and 10-min of pre-wetting prior to rainfall simulation

[d] Reported sediment concentration reduction values from Foltz and Wagenbrenner (2010)

2.3 Soil Characteristic and Engineering Property Tests

2.3.1 Physical Soil Characteristics

Soil dry density and TOC measured for four unburned and four burned subsamples taken from the block samples are compiled in Table I. Soil surface dry density did not change with high severity burning. Dry density for unburned samples varied from 1.0 to 1.2 g/cm^3, with an average dry density of 1.1 g/cm^3. Dry density for burned samples varied from 0.8 to 1.1 g/cm^3, with an average dry density of 1.1 g/cm^3. Although select studies reported that burning increased soil dry density due to aggregate breakdown and soil structure collapse (e.g. Moody and Martin 2001), other studies reported that average dry density did not change considerably between unburned and burned soils (Moody et al. 2005; Wieting et al. 2017).

Surface TOC did not change with high severity burning (Table I). TOC estimated as the percent mass loss from LOI for unburned samples varied from 5% to 10%, with an average of 8%. Percent mass loss for burned samples varied from 8% to 11%, with an average of 9%. The LOI (TOC) values from this study are similar to those reported in literature, whereby Moody et al. (2005) reported LOI ranging from 6.0% to 7.3% for unburned Colorado soils and 5.8% to 7.4% for burned Colorado soils. Wieting et al. (2017) reported a high-temperature heated (high severity burned) sample average LOI value of 9%.

A possible reason for the lack of change in surface dry density and TOC with high severity burning observed in this study was the size of the surface subsample used for measurements. Subsamples were obtained from the upper 6 cm of the block samples. Thus, although complete combustion of organic matter and destruction of roots was observed in the upper 2 cm of each burned sample, the effects of burning were less pronounced in the rest of the subsample (i.e., between sample depths of 2 cm and 6 cm). An increase in dry density and decrease in TOC with burning may have been measurable if the subsample height was reduced from 6 cm to 2 cm.

Table I. Dry density and total organic carbon (TOC) measured on intact unburned and burned subsamples exhumed from block samples tested in the slope-model experiment.

Sample	*Replicate*	*Dry density (g/cm³)*	*TOC (%)*
Unburned block	1	1.1	5
	2	1.0	9
	3	1.0	8
	4	1.2	10
	Average	1.1 ± 0.1	8 ± 2
Burned block	1	1.1	8
	2	1.1	11
	3	0.8	9
	4	1.1	10
	Average	1.1 ± 0.1	9 ± 1

2.3.2 Hydraulic Soil Properties

Field saturated hydraulic conductivity of the soil surface (estimated using MDI) and water repellency (estimated using WDPT) measured on unburned and burned block samples are tabulated in Table J. Surface K_{fs} slightly increased with high severity burning and slightly decreased between the first and second rainfall simulation on burned block samples. The K_{fs} for unburned samples prior to the first rainfall simulation varied from 5×10^{-5} to 1×10^{-3} cm/s, with an average $K_{fs} = 5 \times 10^{-4}$ cm/s. The K_{fs} for burned samples prior to the first rainfall simulation varied from 5×10^{-4} to 6×10^{-3} cm/s (average $K_{fs} = 3 \times 10^{-3}$ cm/s), whereas K_{fs} for burned samples prior to the second rainfall simulation varied from 8×10^{-4} to 1×10^{-3} cm/s (average $K_{fs} = 1 \times 10^{-3}$ cm/s). An increase in K_{fs} with burning was not expected based on previous studies that suggest K_{fs} decreased with burning (e.g. Ebel et al. 2012). However, Wieting et al. (2017) also showed an increase in K_{fs} between unburned and burned soils with average values of 3.7×10^{-5} cm/s and 1.4×10^{-4} cm/s, respectively.

Table J. Saturated field hydraulic conductivity (K$_{fs}$) and wettability index measurements conducted on burned and unburned block samples tested in the slope-model experiment.

Sample	Replicate	Time	K$_{fs}$ (cm/s) [a]	WDPT (s) [b]
Unburned block	1		3×10^{-4}	<5
	2		5×10^{-5}	<5
	3		2×10^{-4}	<5
	4		1×10^{-3}	<5
	Average		5×10^{-4}	<5
Burned block	1	Before rainfall	2×10^{-3}	<5
		After rainfall	1×10^{-3}	<5
	2	Before rainfall	4×10^{-3}	<5
		After rainfall	8×10^{-4}	<5
	3	Before rainfall	6×10^{-3}	<5
		After rainfall	1×10^{-3}	<5
	4	Before rainfall	5×10^{-4}	<5
		After rainfall	8×10^{-4}	<5
	Average	Before rainfall	3×10^{-3}	<5
		After rainfall	1×10^{-3}	<5

[a] Average value from 2 MDI tests
[b] Average value from 3 drops

Based on the WDPT class ranges proposed by Doerr et al. (2004), the water repellency rating was wettable for both unburned and burned soil surfaces. However, the repellency rating 2 cm below the soil surface for unburned soils was wettable, where for burned soils was extremely repellent. This result implies the subsurface formation of a hydrophobic layer with burning developed and was attributed to the condensation of organic hydrophobic coatings. The wettable surface on burned samples was likely due to presence of an ash layer, since the ash layer was not removed prior to testing. Ebel et al. (2012) found that ash layers had a much larger infiltration capacity than burned soil. Thus, the ash layer can create a temporary storage layer above a subsurface hydrophobic layer. Similarly, Woods and Balfour (2008) and Larsen et al. (2009) found that the ash layer created by burning provided additional water storage capacity and prevented soil surface

sealing. The hydrophobic layer created with burning in this study was not at the soil surface, which

left a highly wettable ash layer above the hydrophobic layer to temporarily store water.

2.3.3 Mechanical Soil Properties

Shear strength of intact samples excavated from unburned and burned block samples as well as

unburned remolded samples was measured in direct shear. A summary of the direct shear tests

conducted is in Table K along with the σ'_n, peak shear strength (τ_p), and horizontal displacement

to peak shear strength. The τ_p listed in Table K are actual peak shear strengths if a peak shear stress

was observed or represent the shear stress at a horizontal displacement of 7 mm. The purpose of

testing unburned, remolded soil (dry density = 1.2 g/cm^3) was to analyze the effect of roots on

shear strength parameters. This collection of direct shear tests aided in evaluating the hypothesis

that high severity soil burning reduced shear strength due to loss of surface vegetation.

Relationships of τ_p versus σ'_n for direct shear tests conducted on intact unburned soil, intact burned

soil, and unburned remolded soil are shown in Figure 11. Peak shear strength of the unburned

remolded soil coincided with lower-bound τ_p plotted in Figure 11, such that nearly all τ_p measured

on intact burned and unburned soil specimens plotted above the strength envelope for the unburned

remolded soil. At least three replicate direct shear tests were conducted on intact burned and

unburned soil specimens at each σ'_n (Table K). Considerably more scatter was observed in τ_p

measured on the intact burned soil samples relative to the intact unburned soil. Furthermore, τ_p for

the intact burned soil at a given σ'_n ranged from as high as τ_p measured on intact unburned soil and

as low as τ_p measured on unburned remolded. This scatter in τ_p measured on intact burned soil

specimens was attributed to variability in surface burning. Select locations on the surface retained

roots after burning that led to τ_p similar to the unburned intact specimen. In contract, other locations

on the burned soil surface had completely destroyed root structures after burning that reduced τ_p to levels comparable with the unburned remolded soil.

Table K. Shear strength measured on intact unburned and burned subsamples exhumed from block samples tested in the slope-model experiment and unburned, remolded samples tested in drained direct shear.

Sample	Effective Normal Stress (kPa)	Peak Shear Strength (kPa)	Horizontal Displacement at Peak Shear Strength (mm)
Unburned block	17.2	20.5	7.0
		23.8	7.0
		19.5	7.0
	32.7	38.9	7.0
		39.8	7.0
		37.9	7.0
	63.6	67.6	7.0
		65.3	7.0
Burned block	17.2	12.1	7.0
		29.3 [a]	7.0
		19.8	7.0
		26.4	6.9
	32.7	33.4	7.0
		29.7	7.0
		41.7	7.0
		37.2	7.0
	63.6	55.8	7.0
		69.2	7.0
		69.3	7.0
		62.2	7.0
Unburned, remolded	17.2	13.6	7.0
	32.7	33.1	6.4
	63.6	52.3	7.6

[a] Outlier

The burned block outlier was due to an observed rock in the shear plane and was not included in the development of the burned strength envelope. Only 2 tests are presented for intact, unburned soil tested at σ'_n of 63.6 kPa due to testing equipment error during the 3 test.
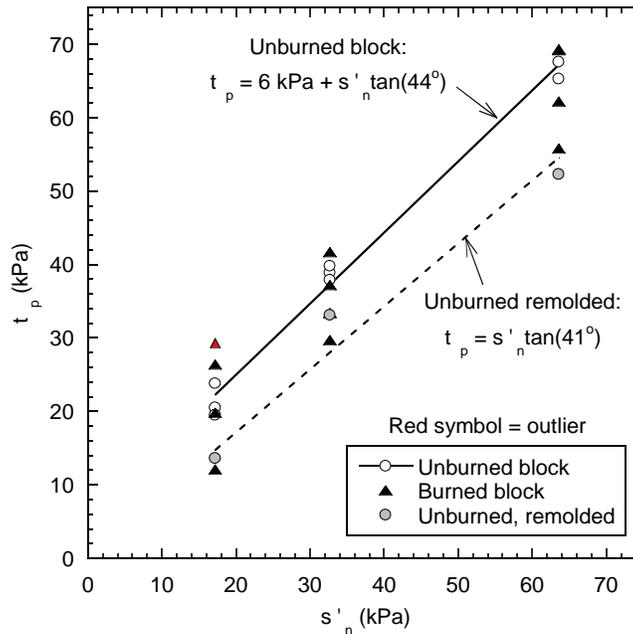
Figure 11. Strength envelopes for undisturbed surface samples of unburned and burned soil and unburned, remolded soil using direct shear. The burned block outlier was due to an observed rock in the shear plane.

Strength envelopes determined for each of the data sets in Figure 11 exhibited a high degree of linearity, with coefficients of determination (R^2) ranging from 0.92 to 0.99. Effective cohesion intercepts ranged from 0 kPa for unburned remolded soil, to 6 kPa for unburned intact soil. The effective stress friction angle (Φ') for unburned and burned intact soil and unburned remolded soil were similar, ranging from 40° to 44°. These similarities in Φ' but differences in c' were expected. Burning and remolding did not necessarily alter the mineral properties of the soil, which contribute to frictional strength. However, burning does, compromise root strength and the action of remolding completely removed roots. These results suggest that unburned soil can be remolded at a representative surficial dry density and evaluated in direct shear to estimate frictional strength that would be anticipated present within the soils following a wildfire.

2.3.4 Summary of Effects of Burning on Soil Characteristics

Considerable changes in soil physical characteristics and hydraulic and mechanical properties between unburned and burned soil samples were not found in this study. Similarities in surface dry density, organic matter, field saturated hydraulic conductivity, and shear strength between unburned and burned soil samples imply that the observed increases in erosion on bare burned samples during rainfall simulations was mainly caused by the destruction of surface cover with burning. This result is similar to that drawn by Larsen et al. (2009) who found post-fire sediment yields were likely not due to fire-enhanced soil water repellency, but were attributed to the loss of ground cover. Several studies (e.g. Neary et al. 1999; DeBano 2000; Doerr et al. 2000) have suggested that observed increases in runoff and erosion following high severity wildfires are due in large part to changes in soil characteristics and properties; however, results from this study suggest that soil properties may not change considerably with burning.

CHAPTER 3: DISCRETE ELEMENT METHOD MODELING

3.1 Computational Details of the DEM Model

A numerical model using the discrete element method (DEM) was developed to better understand reinforced soil behavior at a particle level. Verification of the accuracy of the DEM model will have potential future applications to allow for rapid assessment of the controlling input parameters. These include but are not limited to the material properties of the particles, particle size distribution, and surface slope, the ground treatment type and associated properties, hydraulic loading mechanisms, and other types of applied external loads without having to construct a physical model.

The overall modeling procedure incorporated within the DEM code first introduced in
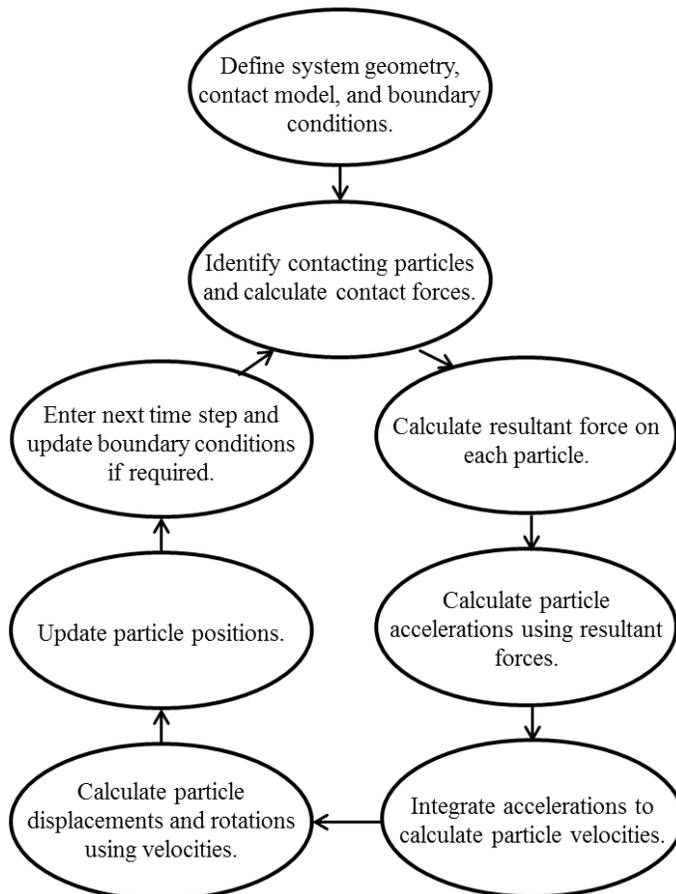
Figure 2 will again be briefly described and additional details are given in subsequent sections of this chapter. The system geometry and boundary conditions are described first, as is the total range of time over which the analysis will be completed. The total time duration is divided into a finite number of time steps. For each time step, the contacting particles are identified using a contact detection algorithm and the contact forces are calculated between interacting particles. The resultant force acting on each particle is calculated, including body forces and all external forces that include but are not limited to those from gravity, hydraulic forces, and changing boundary conditions. Using the resultant forces that act on each particle, the particle accelerations are calculated and then integrated in time to determine particle velocities. Finally, for each time step, the particle displacements are calculated and the current particle positions are updated. These steps are then repeated for the next time step where forces will most likely change based on particle location. These steps are repeated until the final time duration has been reached.

Using the DEM model, simulations were performed on both two-dimensional disc and three-dimensional sphere models. Throughout the rest of this section, equations and algorithms that make up the model are discussed along with discussions on why the specific equations, appropriately referenced, were chosen and the associated benefits and/or limitations. For the most part, the equations discussed are for the three-dimensional analyses and the only changes made to the equations for the two-dimensional analyses are the following:

- Translational motion is restrained in the *y* direction;

- Rotational motion is restrained about the *x* and *z* axes; and

- The moment of inertia and volume (therefore also mass) calculations are for discs instead of spheres.

3.1.1 Particle Kinematics

The discrete element model was formulated using Newton's vector equations of motion to govern the particle behavior. Each particle has six degrees of freedom; three translational and three rotational. The expression of the equations of motion governing the translational and rotational dynamic equilibrium of each individual particle i with mass m_i and moment of inertia I_i (Zhu et al. 2007) are expressed as

$$m_i \frac{dv_i}{dt} = \sum_j F_{ij}^c + F_i^f + F_i^g \qquad \text{[Equation 4]}$$
$$I_i \frac{d\omega_i}{dt} = \sum_j M_{ij}^c \qquad \text{[Equation 5]}$$

where v_i is the translational velocity, ω_i is the rotational velocity of particle i, F_{ij}^c is the contact force and M_{ij}^c is the contact moment acting on particle i by particle j or boundary conditions, F_i^f is the particle-fluid interaction force on particle i, F_i^g is the gravitational force, and t is time. The derivatives of translational and rotational velocities with respect to time are the translational and rotational accelerations of the particle.

The computational algorithm used in this study calculates the right hand side of $mi\frac{dv_i}{dt} = \sum_j F_{ij}^c + F_i^f + F_i^g$ [Equation 4 as the resultant force on each particle for each time step. This force has three values (for each particle), one in each the x, y, and z directions, which will be called F_i^{tx}, F_i^{ty}, and F_i^{tz}, respectively, for time step t. After these resultant forces are calculated, they are divided by the mass of the particle to obtain the accelerations of the particle in the x, y, and z directions for time step t. Similarly, the right hand side of $Ii\frac{d\omega_i}{dt} = \sum_j M_{ij}^c$

[Equation 5 is calculated as the resultant moment on each particle for each time step about the x, y, and z axes, M_i^{tx}, M_i^{ty}, and M_i^{tz} respectively, and then these are divided by the moment of inertia of the particle to obtain the rotational accelerations. The accelerations are

given by a_i^{tx}, a_i^{ty}, and a_i^{tz}, translational, and $\dot{\omega}_i^{tx}$, $\dot{\omega}_i^{ty}$, and $\dot{\omega}_i^{tz}$, rotational, and are defined as

$$a_i^{tj} = \frac{F_i^{tj}}{m_i} \qquad \textbf{[Equation 6]}$$

$$\dot{\omega}_i^{tj} = \frac{M_i^{tj}}{I_i} \qquad \textbf{[Equation 7]}$$

where j goes from 1 to 3, with 1=x, 2=y, and 3=z. This nomenclature is used throughout the rest of this report.

In terms of structural dynamics nomenclature for discrete systems, the terms associated with mass density are contained in the mass matrix, which is a diagonal matrix containing only non-zero entries on the diagonal (essentially the same as lumped mass matrices used in the finite element method). Computational space is reduced if the mass of each particle is saved in an Nx1 array, where N is the number of particles, instead of an NxN array with non-zero values only existing on the diagonals. Therefore, the acceleration of each particle can be solved separately instead of having to solve a system of equations simultaneously. This is a significant difference between modeling a collection of particles and, for example, a continuous structural system where the mass matrix is not diagonal.

The velocities of particle i for time step t in the x, y, and z directions, v_i^{tx}, v_i^{ty}, and v_i^{tz}, translational, and ω_i^{tx}, ω_i^{ty}, and ω_i^{tz}, rotational, respectively, can then be calculated using

$$v_i^{tj} = v_i^{(t-1)j} + a_i^{tj} dt \qquad \textbf{[Equation 8]}$$

$$\omega_i^{tj} = \omega_i^{(t-1)j} + \dot{\omega}_i^{tj} dt \qquad \textbf{[Equation 9]}$$

where $v_i^{(t-1)j}$ and $\omega_i^{(t-1)j}$ are the initial translational and rotational velocities of particle i at the beginning of the time step (also the final velocities from the previous time step) and dt is the value of the time increment for the time step, in seconds. The initial velocities are equal to zero during the first time step, unless a non-zero initial velocity for a particle is specified. At the end of each time step, v_i^{tx}, v_i^{ty}, v_i^{tz}, ω_i^{tx}, ω_i^{ty}, and ω_i^{tz} are saved as the initial velocities for the next time step.

Next, the translational distances that the center of each particle travels in the time step, d_i^{tx}, d_i^{ty}, and d_i^{tz}, in the x, y, and z directions, respectively, are calculated using

$$d_i^{tj} = v_i^{tj} dt \qquad \text{[Equation 10]}$$

The angles of rotation of the edges of each particle, θ_i^{tx}, θ_i^{ty}, and θ_i^{tz}, in the x, y, and z directions, respectively, with radius R_i are calculated using

$$\theta_i^{tj} = \frac{\omega_i^{tj} dt}{R_i} \qquad \text{[Equation 11]}$$

Finally, the positions and edge locations of the particles are updated by adding the distances moved to the final locations of the previous time step, x_i^t, y_i^t, and z_i^t, using

$$x_i^t = x_i^{t-1} + d_i^{tx} \qquad \text{[Equation 12]}$$
$$y_i^t = y_i^{t-1} + d_i^{ty} \qquad \text{[Equation 13]}$$
$$z_i^t = z_i^{t-1} + d_i^{tz} \qquad \text{[Equation 14]}$$

Assigning the x, y, and z locations of each particle to a time step is essential, because issues will arise when the location of a particle is updated mid time step (i.e. after particle-particle contact is calculated for another particle), before the particle is analyzed in the force summation loop. Because the forces, and subsequently the accelerations, velocities, and distances, are direction defined, negative values automatically follow through the calculations and the positions are correctly updated. These calculations are repeated for every time step.

One issue that needs to be resolved in any computational scheme is determining the appropriate value for dt. In general, this can be of any arbitrary magnitude. However, this value must not exceed the critical time increment that has been determined (O'Sullivan 2011 and Sheng et al. 2004), and used by commercial software TRUBAL and EDEM, beyond which solutions can potentially be unstable. The main reason for the instability that arises is that discrete element modelling does not consider disturbances, say from one particle colliding with another, propagating further than the immediate neighbors of the particle. Therefore, if the time increment is sufficiently small, an assumption can be made that the force propagation is negligible compared

to the other forces in the system (Zhu et al. 2007). This assumption is used by Cundall and Strack (1979) and greatly reduces the memory requirements for DEM simulations. The limiting time increment is defined as dt_{crit}, which is defined for DEM simulations with spheres and a Hertzian contact model by (Sheng et al. 2004)

$$dt_{crit} = \frac{\pi R_{min}}{\alpha} \sqrt{\frac{\rho}{G}} \qquad \text{[Equation 15]}$$

where R_{min} is the minimum radius of all particles in the simulation and ρ and G are the density and the shear modulus of that smallest particle. If there are multiple particles with the minimum radius and are composed of different materials, all values for density and shear modulus should be checked so that the smallest time step will be calculated. Finally, α is defined by (Sheng et al. 2004) as

$$\alpha = 0.1631\nu + 0.876605 \qquad \text{[Equation 16]}$$

where ν is the value of the Poisson's ratio for the most critical material of the smallest particles.

$\boldsymbol{dtcrit} = \frac{\pi R_{min}}{\alpha} \sqrt{\frac{\rho}{G}}$ [Equation 15 is derived from the Rayleigh wave surface velocity equation, with α being the root of an eighth order equation and approximated with

$\boldsymbol{\alpha} = \boldsymbol{0.1631\nu + 0.876605}$ [Equation 16 (Sheng et al. 2004), therefore the

critical time step calculated with $\boldsymbol{dtcrit} = \frac{\pi R_{min}}{\alpha} \sqrt{\frac{\rho}{G}}$ [Equation 15 is also

referred to as the Raleigh time step (Bossy and Safuryn 2016). The critical time step increases with increased minimum radius and density of the material. If very small particles are being used in the simulation, density scaling may be appropriate to increase the minimum time increment and make the run times more reasonable (O'Sullivan 2011).

The Raleigh time step does not take into account the relative movement of particles and the value may turn out to still be too large to ensure numerical stability. Therefore, if relative velocities between particles are very high and numerical instability occurs, the time step should be reduced

further. The Raleigh time step is only an approximation and therefore a fraction of the value is typically used in simulations (Bossy and Safuryn 2016). Using a small fraction of the Raleigh time step for the simulations will greatly increase the simulation time, therefore a balance must be found and for high relative velocities between particles. This balance is typically a time step that is 20% of the Raleigh time step (Bossy and Safuryn 2016).

3.1.2 Particle Shape

Spheres are by far the most common type of particle shape used in three-dimensional DEM analyses (O'Sullivan 2011). Spheres possess the simplest and most efficient method of contact detection, which significantly decreases the simulation time (Bossy and Safuryn 2016). There are simple calculations to determine if a sphere is in contact with other spheres or with boundaries. Even ellipsoids, having relatively simple geometry, involve solving a non-linear equation to solve contact resolution (O'Sullivan 2011). Determining what to use for the shape of the particles causes the analyst to trade between computational cost and physical practicality. For these reasons, spheres were chosen for the simulations performed with this DEM model.

3.1.3 User Inputs

The execution of any DEM simulation requires that the following variables must generally be known:

- Number of particles;

- Number of time steps;

- Time increment for each time step;

- Minimum and maximum dimensions in the x, y, and z directions;

- Density, velocity profile, liquid surface tension, and contact angle of the fluid (water in

71

this case);

- Gravity magnitude and direction;

- Coefficient of restitution between particles and rigid walls;

- Global damping coefficient;

- Individual particle properties, including particle density, Young's modulus, shear modulus, and Poisson's ratio; and

- Damping coefficient for particle-particle contact forces.

3.1.4 Contact Forces between Particles

3.1.4.1 Contact Detection Algorithm

To save computational time, the discrete element model uses a contact detection algorithm to determine which particles are near enough to be checked for physical contact. This allows for only the particles that are near each other to go through the contact force loop instead of every particle being checked with every other particle in the packing. One way of looking at the amount of time that can be saved is to imagine a person only having to say hello to all of their immediate neighbors, instead of every other person on the planet. The requirements for a contact detection algorithm are reliability, ease of implementation, and time and memory efficiency (Munjiza 2004).

This discrete element model uses a grid based algorithm, similar to the method proposed by Munjiza (2007). The algorithm developed here assigns cell numbers to every particle and then only checks particles in the same or adjacent cells for contact. The grid is automatically split into equally sized cells with size calculated as a function of the maximum particle radius present in the simulation. For example, depending on the initial geometry of the simulation, the grid could be composed of 1,000 cells with a 10x10x10 cell structure. Basing the cell sizes off of the actual radii of the particles being simulated, as opposed to making the size of the cells a user input or just a

constant value, makes the algorithm more efficient. This is an advantage, because the algorithm is written to optimize the size of the cells to ensure all particle contacts will be detected while also minimizing the number of particle-particle contact checks performed in the program, thereby saving computational time.

One aspect that could be seen as a "limitation" of this contact detection algorithm is that all of the cells are the same lengths in the x, y, and z directions. This would only be a limitation if a very specific problem is being run, for example, a problem with geometry of very large sized particles on one side of a boundary and very small sized particles on the other side. Even in this case, the contact detection algorithm will still work; however, technically the algorithm could be more time efficient if the cells could be different sizes (e.g. smaller sized cells containing the smaller particles will allow for less contact checks). This is a very specific problem and for the analyses presented in this report (along with the vast majority of DEM research problems), the fact that the cells are all the same size is not a limitation. The primary physical limitation is that cells should not be smaller than the size of the largest particle (O'Sullivan 2011).

3.1.4.2 Normal Contact Forces

Once two particles are found to be in the same or adjacent cells by the contact detection algorithm, the distance between the particles is calculated. The overlap behavior of two particles coming into contact can be seen in Figure 12. If the particles are in contact with one another, particle contact forces exist as the particles deform. In the DEM simulations modeled for this research, particles do not actually deform the way they would in real life, but the amount of overlap is accurately controlled to mimic the real world elastic deformations (Padros and Kokocinska 2016). This is considered a soft-sphere method of discrete element modeling, as opposed to hard-sphere which does not allow for any overlap. The soft-sphere approach allows for both normal and tangential

forces to be more accurately evaluated and is the most common approach used in current practice (Bossy and Safuryn 2016).

In Figure 12, two particles with known velocities come into contact with each other. Forces develop, acting in opposite directions, on the particles as a function of the amount of overlap between the particles, calculated based off the locations of the centers and the known radii values. The force calculations are dependent on the chosen contact model being used in the DEM simulation.
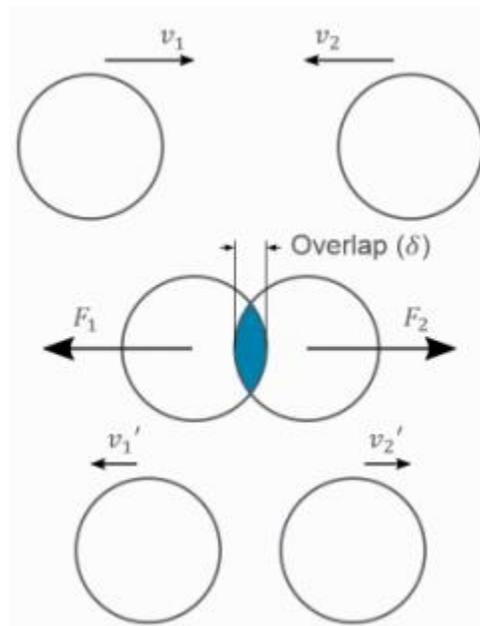
Figure 12. Soft-sphere approach allowing overlap between two contacting particles (Bossy and Safuryn 2016).

A number of different contact models exist that can accurately model realistic material behavior. The simplest types of contact models assume that the contact between two particles, which is in fact a very complex nonlinear problem of solid mechanics, can be represented by a linear spring with stiffness K_n that exists between two particles as they come in contact with one another. Because the linear spring stiffness does not have an easily intuitive relationship with respect to the

known properties of the particle, models have been developed to link the stiffness to the physical particle material properties. This DEM model uses a simplified Hertzian contact model, with stiffness for time step t, K_n^t, calculated by (O'Sullivan 2011)

$$K_n^t = \left(\frac{2\langle G \rangle \sqrt{2\langle R \rangle}}{3(1 - \langle v \rangle)}\right) \sqrt{\delta_n^t} \qquad \text{[Equation 17]}$$

where, for sphere-sphere contact, the coefficients are calculated as (O'Sullivan 2011)

$$\langle R \rangle = \frac{2R_A R_B}{R_A + R_B} \qquad \text{[Equation 18]}$$
$$\langle G \rangle = \frac{1}{2}(G_A + G_B) \qquad \text{[Equation 19]}$$
$$\langle v \rangle = \frac{1}{2}(v_A + v_B) \qquad \text{[Equation 20]}$$
$$\delta_n^t = R_A + R_B - d_{AB}^t \qquad \text{[Equation 21]}$$

Here R is the sphere radius, G is the elastic shear modulus, v is the Poisson's ratio, and the subscripts A and B refer to two spheres, A and B, in contact. Lastly, δ_n^t is the sphere overlap for time step t, with d_{AB}^t being the distance between the centers of the two particles at time step t, and calculated by

$$d_{AB}^t = \sqrt{{d_{xAB}^t}^2 + {d_{yAB}^t}^2 + {d_{zAB}^t}^2} \qquad \text{[Equation 22]}$$

where d_{xAB}^t, d_{yAB}^t, and d_{zAB}^t are the x, y, and z distances between the centers of the particles, respectively, during time step t, and calculated by

$$d_{xAB}^t = x_A^t - x_B^t \qquad \text{[Equation 23]}$$
$$d_{yAB}^t = y_A^t - y_B^t \qquad \text{[Equation 24]}$$
$$d_{zAB}^t = z_A^t - z_B^t \qquad \text{[Equation 25]}$$

The equations represented above amount to an effort to replicate the actual deformation between two elastic spheres with a relative simple one-dimensional relationship rather than using the full equations of three-dimensional elasticity.

The normal contact forces between the particles in the x, y, and z directions, F_{nx}^t, F_{ny}^t, and F_{nz}^t, respectively, for time step t are calculated as (O'Sullivan 2011)

$$F_{nj}^t = K_n^t \delta_n^t \frac{d_{jAB}^t}{d_{AB}^t} \qquad \text{[Equation 26]}$$

The magnitude of the distance between the particles, d_{AB}^t, is always positive, but d_{xAB}^t, d_{yAB}^t, and

d_{zAB}^t can be positive or negative depending on the location of the particles relative to each other. Therefore, the directions of the forces are constantly updated.

The simplified Hertzian contact model is effective for use in DEM simulations because the model provides a logical basis for the link between spring stiffness and actual material properties. Also, in general, the model can provide very efficient and accurate calculations for non-cohesive granular materials (Bossy and Safuryn 2016).

A linear model was also used for the two-dimensional disc slope stability analyses. This model is simpler, with a constant normal stiffness simply multiplied by the overlap distance to get the forces between particles for each time step. Additional computational details are given later when the simulations are discussed.

3.1.4.3 Tangential Contact Forces

This DEM model uses a simplified Mindlin-Deresiewicz tangential contact model, where the tangential stiffness for time step t, K_t^t (Mindlin and Deresiewicz 1953 and Vu-Quoc et al. 2000) is calculated as

$$K_t^t = K_n^t \left(\frac{2(1-\langle v \rangle)}{2-\langle v \rangle} \right) \qquad \text{[Equation 27]}$$

Because the Poisson's ratios of the particles are a constant, the ratio between normal and tangential stiffnesses is a constant throughout the simulation. The tangential forces are calculated as (O'Sullivan 2011)

$$F_{tj}^t(\delta_t, \dot{\delta}_t) = K_t^t \int_{t_c^0}^{t} \dot{\delta}_t dt \qquad \text{[Equation 28]}$$

where $\dot{\delta}_t$ is the relative velocity between the particles at time t. The integral in $\boldsymbol{Ftjt}(\delta_t, \dot{\delta}_t) = K_t^t \int_{t_c^0}^{t} \dot{\delta}_t dt$ [Equation 28 is approximated by the summation

$$\int_{t_c^0}^{t} \dot{\delta}_t dt \approx \sum_{t_c^0}^{t} \dot{\delta}_t \triangle t \qquad \text{[Equation 29]}$$

and the relative velocity between the particles at time t is given by (O'Sullivan 2011)

$$\dot{\delta}_i = \left[v_i^b + e_{ijk}\omega_j^b\left(x_k^C - x_k^b\right)\right] - \left[v_i^a + e_{ijk}\omega_j^a\left(x_k^C - x_k^a\right)\right] \qquad \textbf{[Equation 30]}$$

where e_{ijk} is the permutation tensor, v and ω are the translational and rotational velocities, respectively, of particles a and b, x^a and x^b are the components of the particle centroids, and x^C are the contact coordinates. The tangential component is then calculated by subtracting the normal component of the relative velocity vector as (O'Sullivan 2011)

$$\dot{\delta}_i^t = \dot{\delta}_i - \dot{\delta}_j n_j n_i \qquad \textbf{[Equation 31]}$$

The tangential forces are limited by a Coulumb friction criteria and are given by (O'Sullivan 2011)

$$F_{tj}^t = -min\left(\left|\mu F_{nj}^t\right|, F_{tj}^t(\delta_t, \dot{\delta}_t)\right)\frac{\dot{\delta}_t}{|\dot{\delta}_t|} \qquad \textbf{[Equation 32]}$$

where μ is the friction coefficient between the particles. The tangential forces are then added to the normal forces and also cause moments about the centers of the particles.

The computational difficulty with the tangential forces is that the tangential displacements must

b

e

i

n

c

r

e

m

e

For mostly static simulations, the tangential force contributions can be negligible because the summed tangential displacements are almost zero. However, because the research performed here is investigating behavior after particles begin to roll, the tangential model is used during all

l

l   77

y

simulations.

Once a particle is found to be in contact with another particle, the forces between them in the x, y, and z directions are calculated only once for that time step and then stored with the same magnitude but in the opposite directions for the other particle.

3.1.5 Boundary Conditions

Two different types of boundary conditions are considered: rigid wall boundary conditions and a boundary condition novel to this DEM model, called a save-mass boundary condition. For calculations performed using this DEM model, the plane equation of the boundary condition must be input in the following form:

$$ax + by + cz + d = 0 \qquad \text{[Equation 33]}$$

During each time step, the distances between each particle and each boundary condition are calculated. If a particle is in contact with a boundary, the forces or displacement relationship between the particle and the boundary are calculated. These forces and displacement relationships are described in the following text for each boundary condition type.

3.1.5.1 Rigid Wall Boundary Conditions

To determine if a particle, i, is in contact with a rigid wall, the distance between the center of the particle and the rigid wall boundary condition at time step t, d_{iBC}^t, is calculated using (O'Sullivan 2011)

$$d_{iBC}^t = \frac{ax_i^t + by_i^t + cz_i^t + d}{\sqrt{a^2 + b^2 + c^2}} \qquad \text{[Equation 34]}$$

where a, b, c, and d are the components of the equation of the plane, from $ax+by+cz+d=0$

[Equation 33, of the rigid wall boundary condition and x_i^t, y_i^t, and z_i^t, are the x, y, and z coordinates of the center of particle i in contact with the wall at time step t. This calculation

method is widely accepted for a sphere-boundary contact (O'Sullivan 2011). Rigid wall boundary conditions also apply if the walls are moving. If this is the case, a, b, c, and d are adjusted throughout the simulation. Care must be taken to ensure the time step increment is appropriate for how fast the wall is moving (i.e. a wall must not move too much in one time step to cause particle instability).

For

If

3.1.5.2

The

Figure
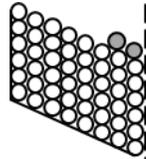
Time step = i
Saved mass = 0

Figure

3.1.6

In

Damping

3.1.6.1

Mass damping (also called global damping), originally proposed by Cundall and Strack (1979), is used for some of the simulations performed for this research. The damping is applied to the

resultant velocities of each particle, changing $vitj = v_i^{(t-1)j} + a_i^{tj}dt$

[

E

$$v_i^{tj} = \left(\frac{v_i^{(t-1)j}(1-\alpha\triangle t/2)+a_i^{tj}dt}{1+\alpha\triangle t/2}\right)$$ [Equation 35]

$$\omega_i^{tj} = \left(\frac{\omega_i^{(t-1)j}(1-\alpha\triangle t/2)+\dot\omega_i^{tj}dt}{1+\alpha\triangle t/2}\right)$$ [Equation 36]

q
Where α is the mass damping coefficient.

u

3.1.6.2 Particle-Particle Contact Damping

As stated before, one problem with the simplified Hertzian contact model and all contact models

that are elastic prior to yielding is that the energy dissipation that occurs physically is not captured

in the model (O'Sullivan 2011). The issue that arises is that if there is no yield by contact

separation, the particles will continue to vibrate like a system of connected elastic springs. Particle-

particle contact damping is used to relieve this issue. In this scenario, the damping forces, F_{dampx}^t,

o
F_{dampy}^t, and F_{dampz}^t, in the x, y, and z directions, respectively, for time step *t* are simply a reduced

contact force and calculated by

a
$$F_{dampj}^t = -\mu_c K_n^t \delta_n^t$$ [Equation 37]

Where μ_c is the contact damping coefficient between the particles. Finally, $Fnjt = K_n^t \delta_n^t \frac{d_{jAB}^t}{d_{AB}^t}$

d
[Equation 26 is changed to include the damping force by

$$F_{nj}^t = \left(K_n^t \delta_n^t + F_{dampj}^t\right)\frac{d_{jAB}^t}{d_{AB}^t}$$ [Equation 38]

R
3.1.7 Loads

E
3.1.7.1 Gravitational Loads

Gravity loading for the analyses considered in this study is significant and one of the primary

forces on the individual particles. Gravity forces are easy to compute, require little explanation,

and are applied for all simulations.

R

e

f

3.1.7.2 Hydraulic Forces

Forces generated by water resulting from rainfall or overland flow are the primary loads affecting soil behavior post-fire. The simulations presented later in this report are tested as worst case scenarios and one assumption made is that overland flow has developed. In this context, overland flow is surface runoff that occurs when excess rainwater flows over the surface of a soil slope and this condition could be present for multiple reasons. For example, the soil could be hydrophobic, fully saturated, or the rain intensity could be so large that the water does not physically have enough time to infiltrate and starts to flow instead. Hydrophobic soils are water repellant and this can occur in burned soils because of water-repellent compounds released by burning plants (Ravi et al. 2009). When rainwater falls onto a hydrophobic soil during a rainfall event, the water collects and pools on the soil surface instead of infiltrating into the ground. This will cause overland flow to occur more quickly and cause higher erosion rates.

One simplification made for the presented simulations is that the particular reason that overland flow is initiated is not a concern; the assumption is simply made that overland flow has developed and is the driving force that moves the soil particles. One reason the assumption of overland flow is made is because the DEM model developed here does not have the capabilities of simulating the fluid itself, but rather only the forces on the particles from the fluid as a function of particle shape, sizes, and fluid properties. Therefore, more complicated fluid behavior would be much more difficult to model, but is a possibility for future work. Because overland flow is assumed to be the driving force, any effects from infiltration are ignored and are not included in the simulations. If infiltration were included, overland flow would take longer to develop and the simulation run times would be much larger.

At a certain point during a precipitation event, enough water will accumulate to start flowing over

81

a soil slope. This will create drag forces on the particles in contact with the fluid. The force applied by runoff water to the soil particles on the surface of a slope is influenced by a variety of factors, such as the geometry of the slope, runoff velocity, density and compactness of the soil, and exposure of each particle to flow. Accounting for the effect of all such factors was beyond the scope of this study, and therefore several simplifying assumptions are made in the modeling of the hydraulic drag forces.

3.1.7.2.1 Simplified Drag Forces: Two-Dimensional Simulations
For the two-dimensional discs, a simplified drag force equation was used. To account for the fact that larger particles typically have a larger surface exposed to flow, one assumption made is that the drag force applied to surface particles is proportional to the radius of the particles. The maximum value of hydraulic drag force on each particle is the product of a scale factor, γ, multiplied by the radius of the particle. Another assumption is that the surface particles are submerged in water and that the buoyancy force will counteract the downward component of the drag force applied to these particles. The drag force on particle i, with radius R_i, and at timestep t, $F_{drag_i}^t$, is only applied in the horizontal direction as

$$F_{drag_i}^t = \gamma R_i \qquad\qquad \text{[Equation 39]}$$

3.1.7.2.2 Drag Forces for Three-Dimensional Simulations
For the three-dimensional sphere slope stability analyses, a more commonly used equation for drag force on a sphere, taking into account actual fluid properties, was used. The drag force on particle i at timestep t, $F_{drag_i}^t$, is given as (Julien 2010)

$$F_{drag_i}^t = \frac{1}{2} \rho V^2 C_d A_i \qquad\qquad \text{[Equation 40]}$$
where ρ is the density of the fluid (1,000 kg/m^3 for water), V is the velocity of the fluid flow, C_d

is a shape factor (0.5 for spheres), and A_i is the projected surface area perpendicular to flow of particle i ($A_i = \pi R^2$ for spheres with radius R). To avoid sudden instabilities, simulations were performed with the velocity of flow linearly increasing until reaching the maximum value. Also, the maximum magnitude of drag force had a linearly increasing profile in the direction of depth of slope. Details on how forces are applied are described later in this chapter when the three-dimensional slope stability simulations are discussed.

A schematic of the drag force applied to a particle is shown in Figure 14. As opposed to the disc simulations where the drag force is applied to the center of the particles, the three-dimensional sphere simulation has drag forces that are applied on the surfaces of the particles and will also create a moment acting at the center of each of the surface particles about the axis into the plane. The assumption is made that the surface particles are submerged in water and that the buoyancy force will counteract the downward component of the drag force applied to these particles.
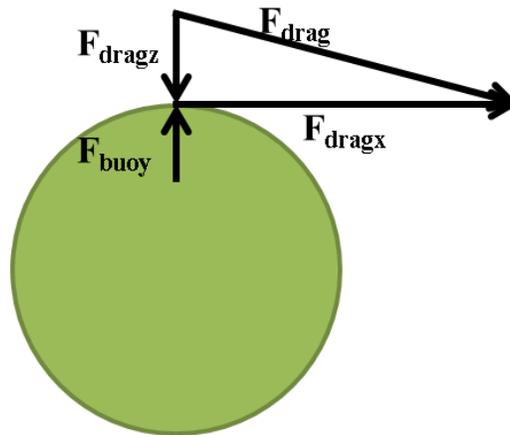
Figure 14. Drag force from overland flow acting on the surface of a particle.

Surface particle identifying algorithms were written for both the 2D and 3D simulations to decide which particles receive surficial drag forces. Details on these algorithms are described later in this

report with examples given on the actual particle slopes used for the simulations.

3.1.8 Natural Root Reinforcements

One of the main objectives of the research presented in this report is to quantify how different amounts and layouts of slope reinforcements stabilize soil slopes. In this DEM model, numerical spring forces are used to simulate roots and other organic matter stabilizing the slopes. This is done by connecting the centers of surface particles to centers of deeper particles by springs with a specified stiffness. The connected surface particles are referred to as reinforced particles. A schematic of this is shown in Figure 15, with the black lines representing the springs connecting surface particles to particles below the surface of the slope.
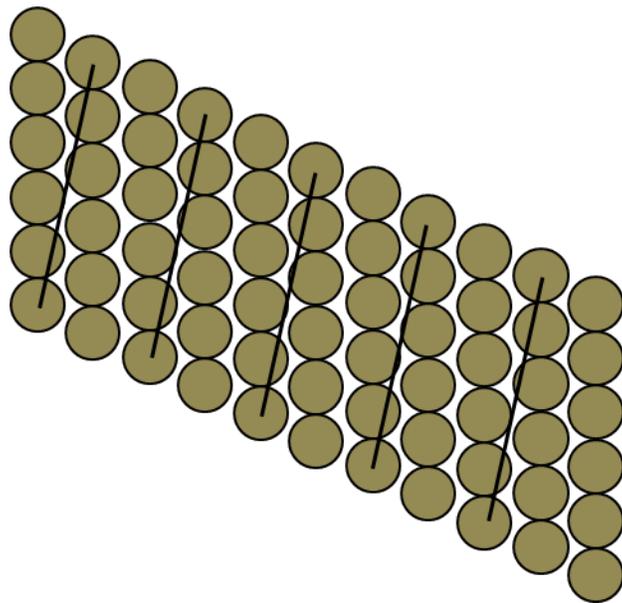
Figure 15. Schematic of numerical springs used to represent natural roots using the DEM. The spheres are soil aggregate particles and the black lines represent the numerical springs.

Initially there are no forces between reinforced particles. In a manner similar to that of a spring, as the surface particles begin to flow and the distances between the particles grow (i.e., the spring extends), forces are developed that act to hold the surface particles in place. Physically, this represents a root, or other type of vegetation, bonded to the particles, acting to reinforce them and stabilize the slope. Although exact forces between soil particles and connected roots have not been quantified, an assumption made for the simulations is that the root stiffness is much larger than the particle-particle contact stiffnesses. Numerically, the spring forces simply act to hold the surface particles in place. As an example, the forces in the DEM model will behave similarly to when weeds are pulled and soil clumps are connected to the roots. If one soil clump is pulled away, the particles will be held by the connected root system.

Once the model recognizes that two particles are connected by a numerical spring, the forces between them (can be tensile or compressive), $F_{springx}^t$, $F_{springy}^t$, and $F_{springz}^t$, in the x, y, and z directions respectively, are calculated very similarly to $\boldsymbol{Fnjt} = K_n^t \delta_n^t \frac{d_{jAB}^t}{d_{AB}^t}$

[Equation 26, by

$$F_{springj}^t = K_{spring}^t \left(\delta_{spring}^t - \delta_{spring1}^t \right) \frac{d_{springj}^t}{\left| d_{spring}^t \right|} \qquad \textbf{[Equation 41]}$$

Here K_{spring}^t is the spring stiffness, δ_{spring}^t is the current distance between the particles, $\delta_{spring1}^t$ is the distance between the particles at t=0, and $d_{springx}^t$, $d_{springy}^t$, and $d_{springz}^t$ are the components of the current distance between the particles in the x, y, and z directions.

T

h

e

o

n

85

l

v

distance between the particles. Therefore there are no spring forces generated between the particles until they start to move.

3.2
Validating

3.3
As

Soil

3.3.1
3.3.1.1
Slope

3.3.1.2
The

Table

BC	Type	a	b	c	d
1	rigid	1	0	0	0
2	rigid	0	0	1	0
3	rigid	-	0	0	0.5
4	save	1	0	0	-

A

Figure
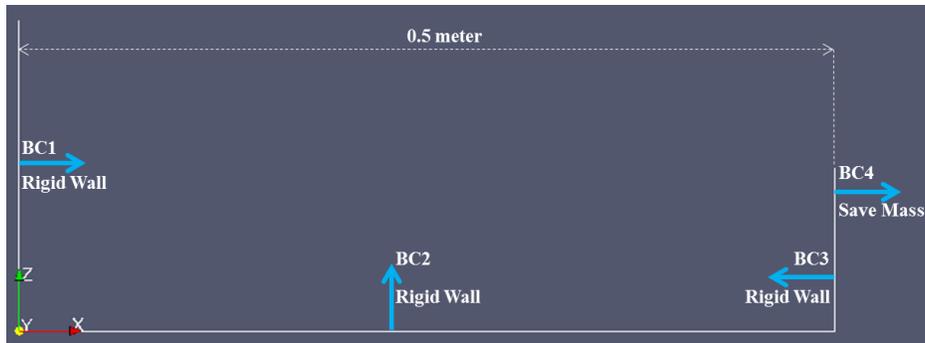
Figure

3.3.1.3

Originally,

These

Finally,
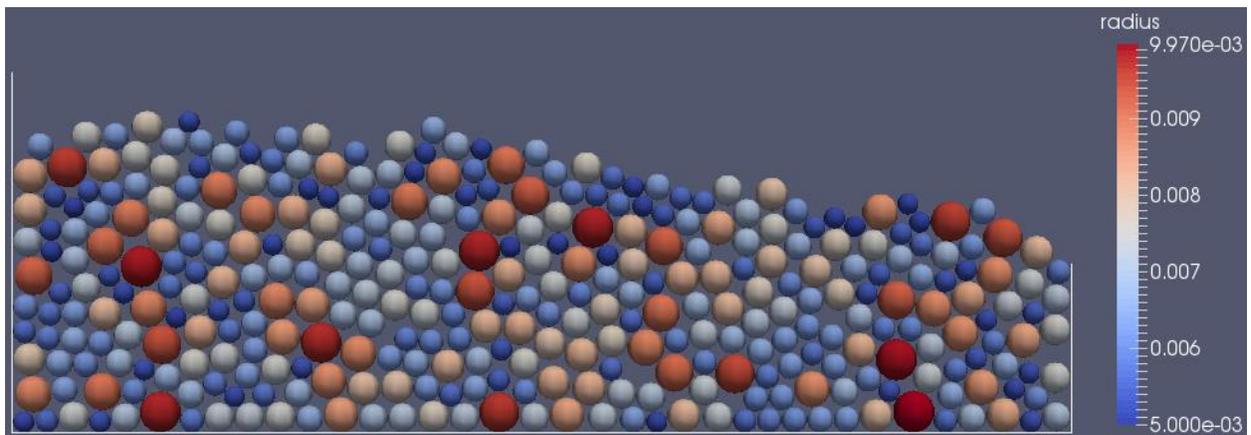
Figure
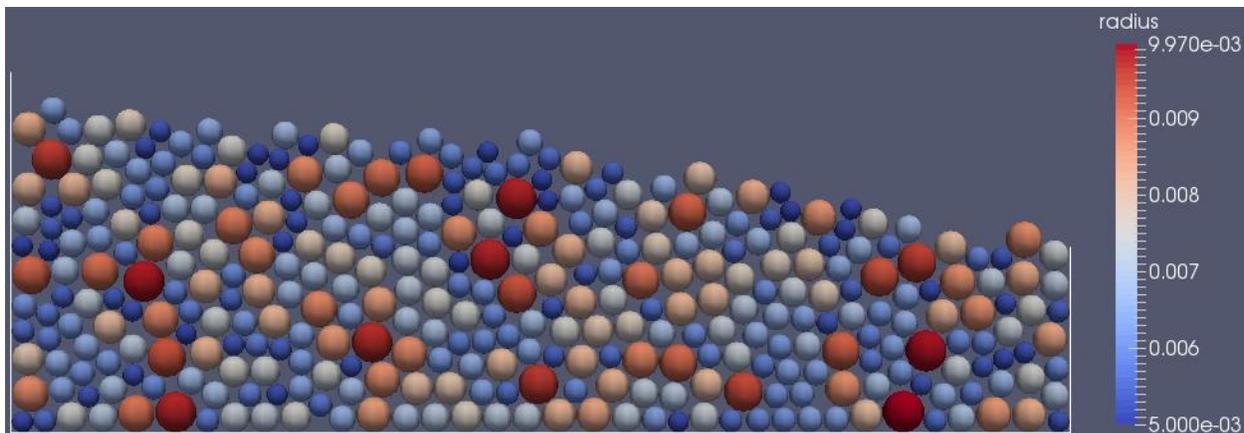
Figure
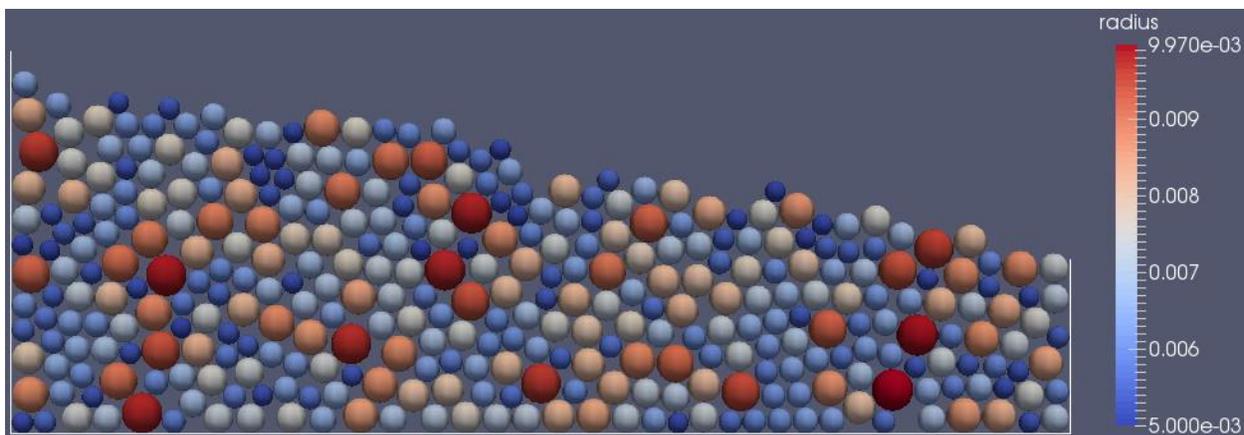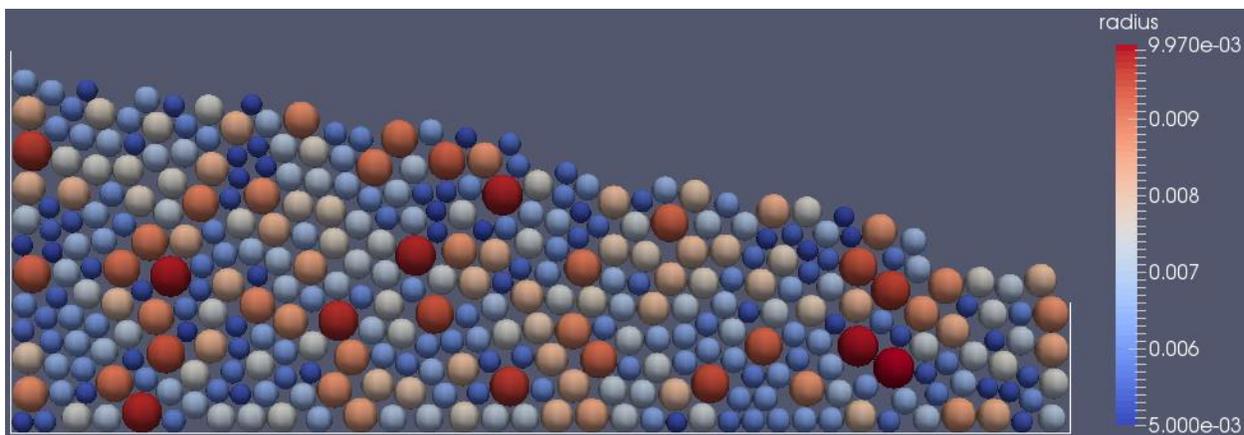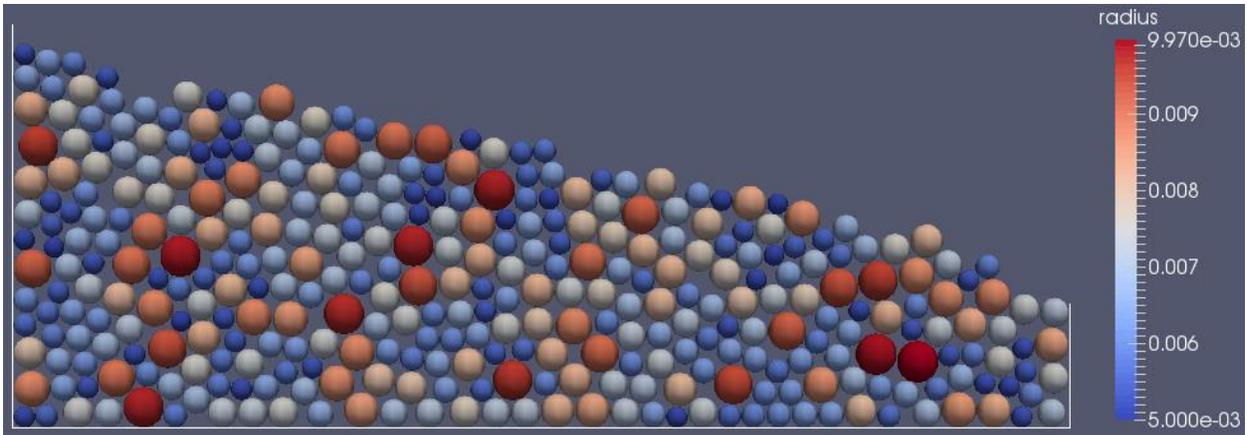
Figure

Figure

Figure

3.3.1.4

Initial configurations of the reinforcement patterns were pre-determined, with either 25% or 50%

of surface particles connected either shallowly (to another particle about 2-3 particles below the

surface) or deeply (1-2 particles above BC2). As previously discussed, the spring forces between

reinforced particles were calculated with $\boldsymbol{Fspringjt} = K_{spring}^{t}\left(\delta_{spring}^{t} - \delta_{spring1}^{t}\right)\frac{d_{springj}^{t}}{\left|d_{spring}^{t}\right|}$

[Equation 41.

Figure 22 through

Figure 26 show all shallow and deep reinforcing cases. Reinforced particles are red and the white

lines show the connections.
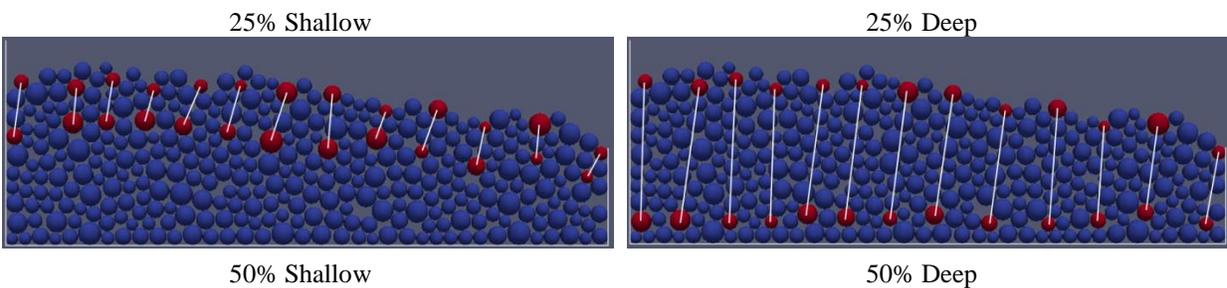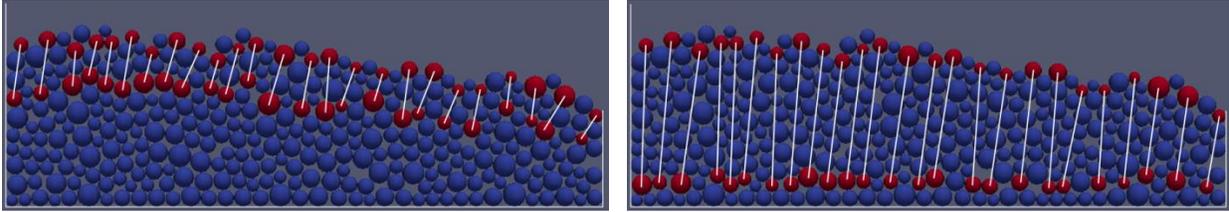
25% Shallow   25% Deep

50% Shallow   50% Deep

Figure 22. Slope 5.89º Shallow and Deep Reinforcements

25% Shallow   25% Deep

50% Shallow   50% Deep

Figure 23. Slope 7.51º Shallow and Deep Reinforcements

25% Shallow   25% Deep

50% Shallow   50% Deep
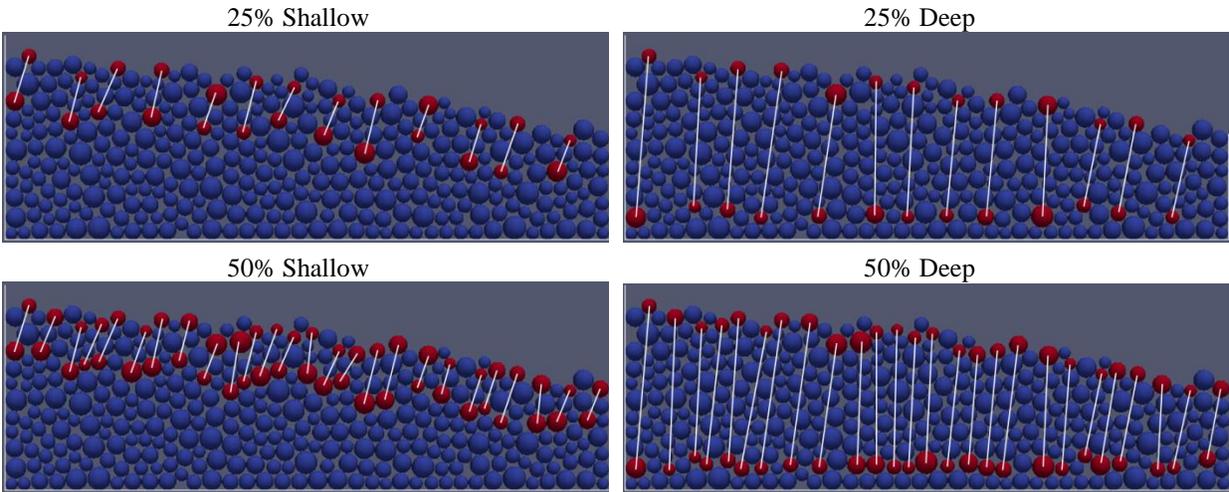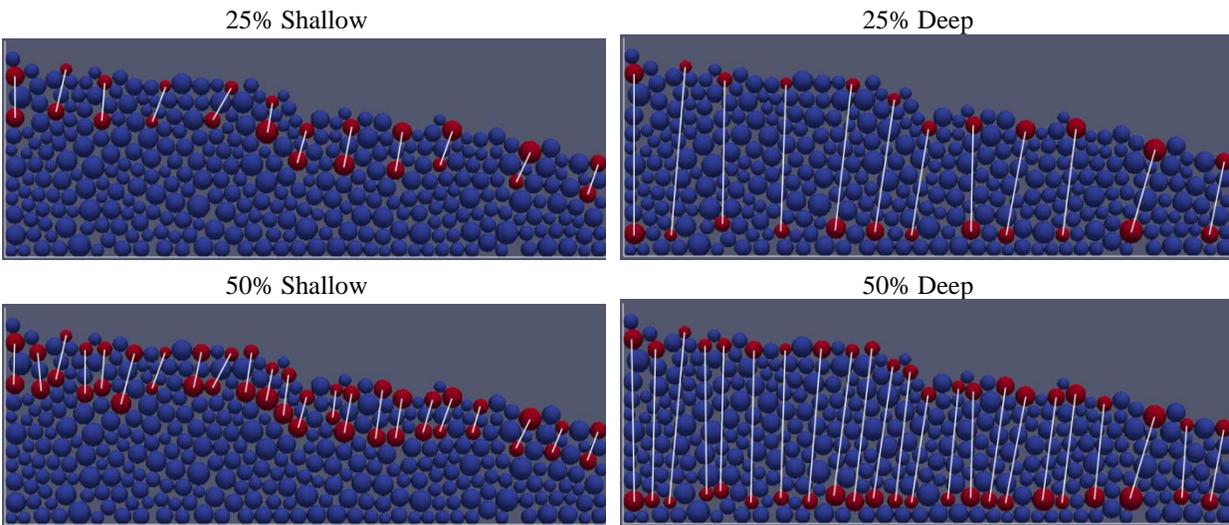
Figure 24. Slope 9.14º Shallow and Deep Reinforcements

25% Shallow   25% Deep

| 50% Shallow | 50% Deep |

Figure 25. Slope 10.93º Shallow and Deep Reinforcements

| 25% Shallow | 25% Deep |

| 50% Shallow | 50% Deep |
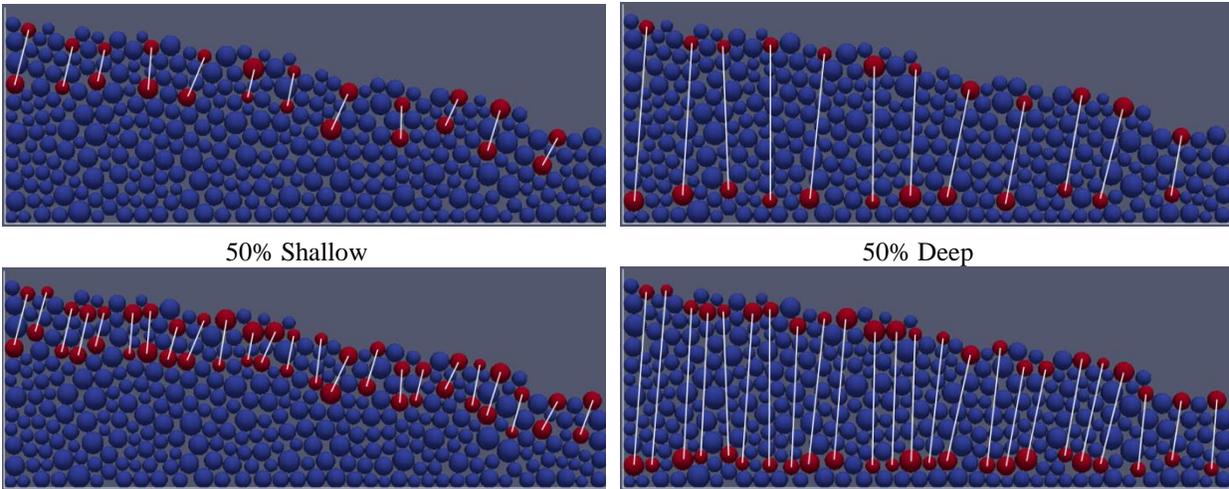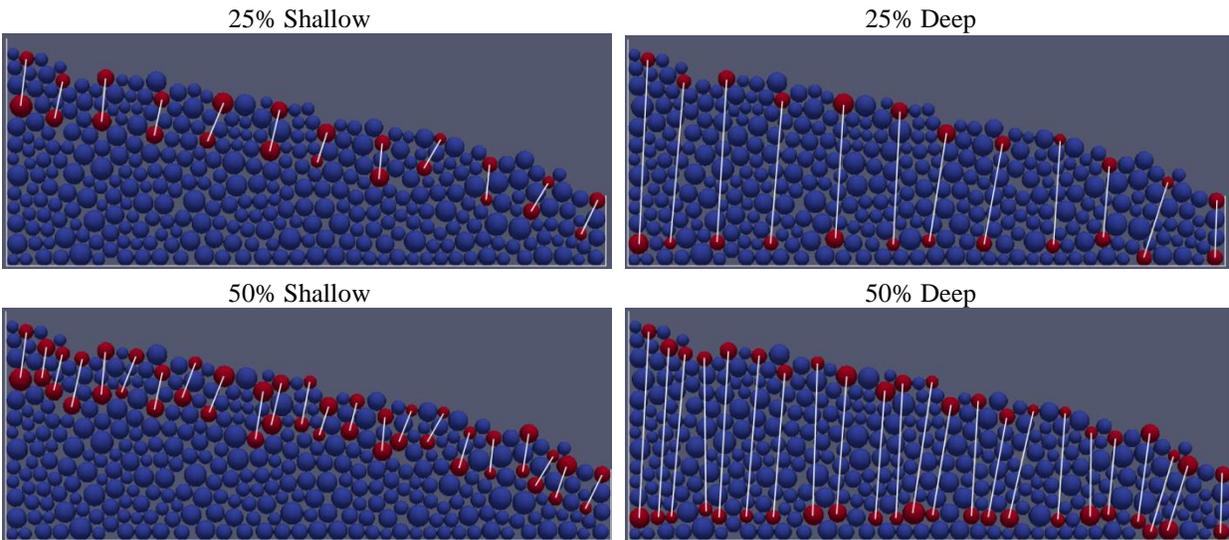
Figure 26. Slope 12.05º Shallow and Deep Reinforcements

3.3.1.5 Hydraulic Loading

The simplified drag force previously described for two-dimensional simulations was applied to all

r

e

i

n

f

o

r

To

One

91

<div align="center">

0	1
2	3
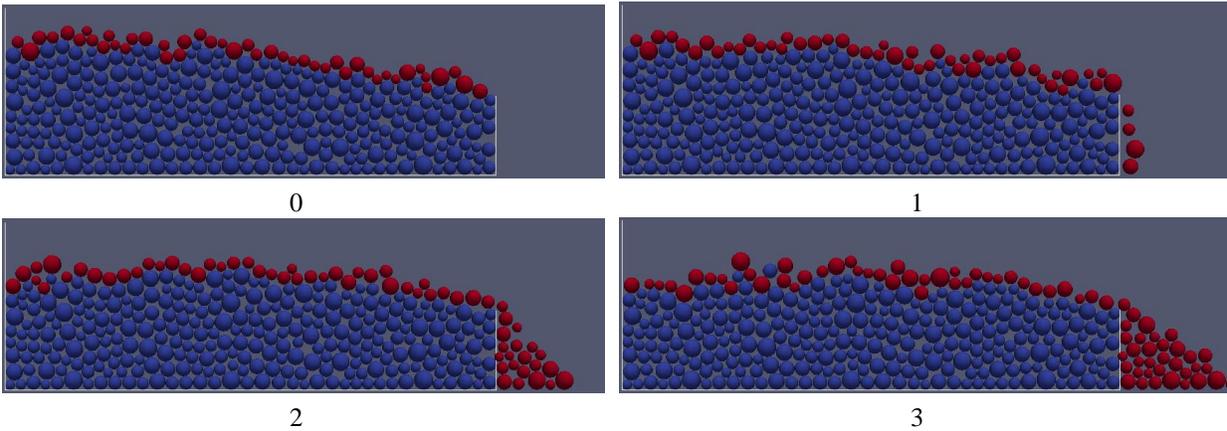
Figure

</div>

3.3.1.6

The linear normal contact model previously discussed was used for all two-dimensional disc simulations described here. Therefore, a normal stiffness had to be specified. Comparisons were done with the Simplified Hertzian contact model for a range of elastic moduli for a coarse sand material of 10-24 N/mm² (APPC-Soil), Poisson's ratio of 0.15, and assuming a maximum overlap of 5% of the diameters of the particles (or 10% of the radii), and a range for normal stiffness was found to be 10,400-25,000 N/m. Therefore, a value of 20,000 N/m was chosen for these simulations. Plugging this normal stiffness and Poisson's ratio into $\boldsymbol{Ktt} = \boldsymbol{K_n^t} \left(\frac{2(1-\langle v \rangle)}{2-\langle v \rangle} \right)$

[Equation 27 gives a constant tangential stiffness of 18,400 N/m.

The strength of roots and other ground vegetation is stronger than the individual contacts between particles. To evaluate a range of realistic root stiffnesses, the following equation was used:

$$K = \frac{AE}{L} \qquad \textbf{[Equation 42]}$$

where K is the stiffness, A is the cross-sectional area, E is the elastic modulus, and L is the length of the specimen. Comparing values from Cofie et al. (2000) for beech roots and Commandeur and Pyles (1991) for Douglas-fir roots, findings showed that the stiffness of roots varies from 75 to

<div align="center">

92

</div>

5000 times the normal contact stiffness between the particles. There is a lot of variability for these stiffnesses. Therefore, to choose a value in the range, but also choose a value low enough not to cause numerical instability in the model, the reinforcement stiffness was chosen to be $100 * K_n$ for the shallow and deep reinforcements. This value was found to be too high for the Net reinforcements and to retrieve realistic behavior and keep the model stable a value equal to K_n was used for the Net reinforcement stiffnesses.

A sufficiently small time increment was chosen and checked to be less than dt_{crit} in $\boldsymbol{dtcrit} =$

$$\frac{\pi R_{min}}{\alpha} \sqrt{\frac{\rho}{G}}$$
[Equation 15 as 10^{-6} seconds. Therefore, for one second of simulation time, one million time steps must be completed in the model. The simulations were run for 3 seconds of simulation time; therefore there were 3 million time steps for each simulation. An observation made after testing the surface particle identifier algorithm, was that the surface particles did not need to be updated every single time step. Therefore, to save time, they are updated every 10,000 time steps, or every one hundredth of a second of simulation time.

All input parameters are summarized in Table M and the third column gives information on where the variable is used.

Table M. Input Parameters for 2D Simulations

Parameter (units)	Value	Needed For
Number of Particles	350	-
Density (kg/m^3)	1850 (APC-Soil)	gravitational loading

Poisson's Ratio	0.15 (AP PC-Soil)		i
dt (sec)	10^{-6}		time increment for time stepping
K_n 20,000	20,0	$Fnjt= K_n^t \delta_n^t \dfrac{d_{jAB}^t}{d_{AB}^t}$	[Equation 26
K_t 18,400	18,4	$Ftjt(\delta_t, \dot{\delta}_t) = K_t^t \int_{t_c^0}^{t} \dot{\delta}_t dt$	[Equation 28
K_r (N/m)	100K	K$_{spring}$ in $Fspringjt= K_{spring}^t(\delta_{spring}^t - \delta_{spring1}^t) \dfrac{d_{springj}^t}{\left|d_{spring}^t\right|}$	[Equation 41
K_{net} (N/m)	K_n	K$_{spring}$ in $Fspringjt= K_{spring}^t(\delta_{spring}^t - \delta_{spring1}^t) \dfrac{d_{springj}^t}{\left|d_{spring}^t\right|}$	[Equation 41
Friction angle	35°	$\tan(35°) = \mu$ in $Ftjt= -\boldsymbol{min}\left(\left|\mu F_{nj}^t\right|, F_{tj}^t(\delta_t, \dot{\delta}_t)\right)\dfrac{\dot{\delta}_t}{\left|\dot{\delta}_t\right|}$	[Equation 32
Global damping coefficient	25		α i n
Particle-particle contact damping coefficient	0.15	μ_c in $Fdampjt= -\boldsymbol{\mu_c} K_n^t \delta_n^t$	[Equation 37

3.3.1.7

An

Other

Finally,

3.3.1.8

3.3.1.8.1

Firstly,
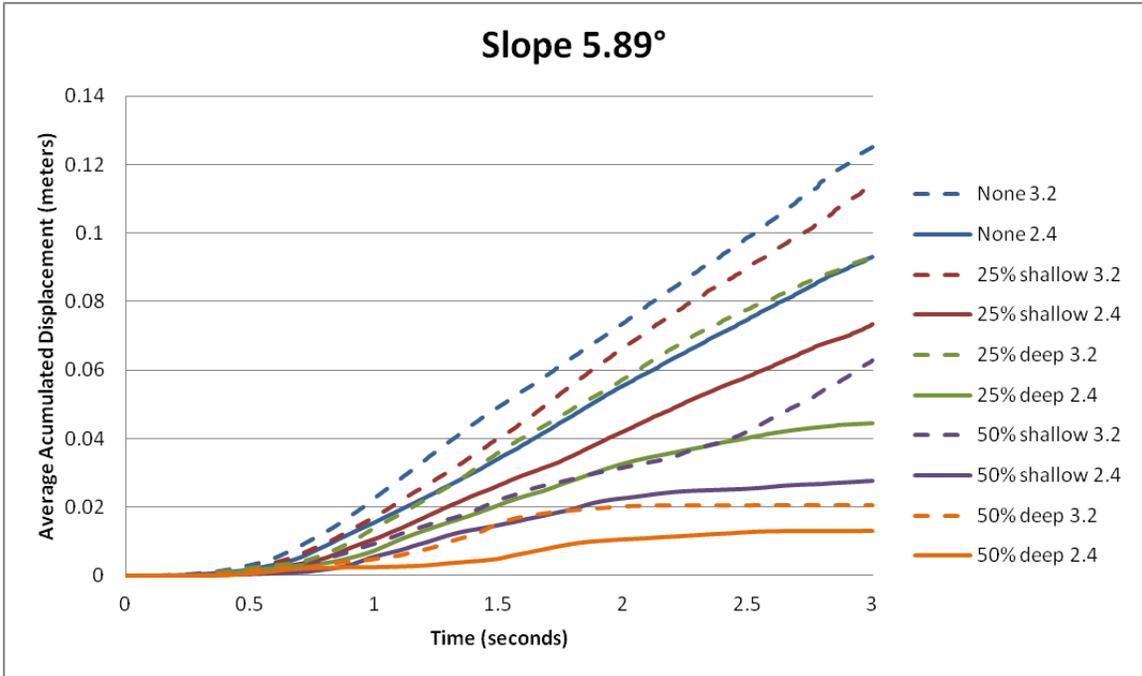
Figure
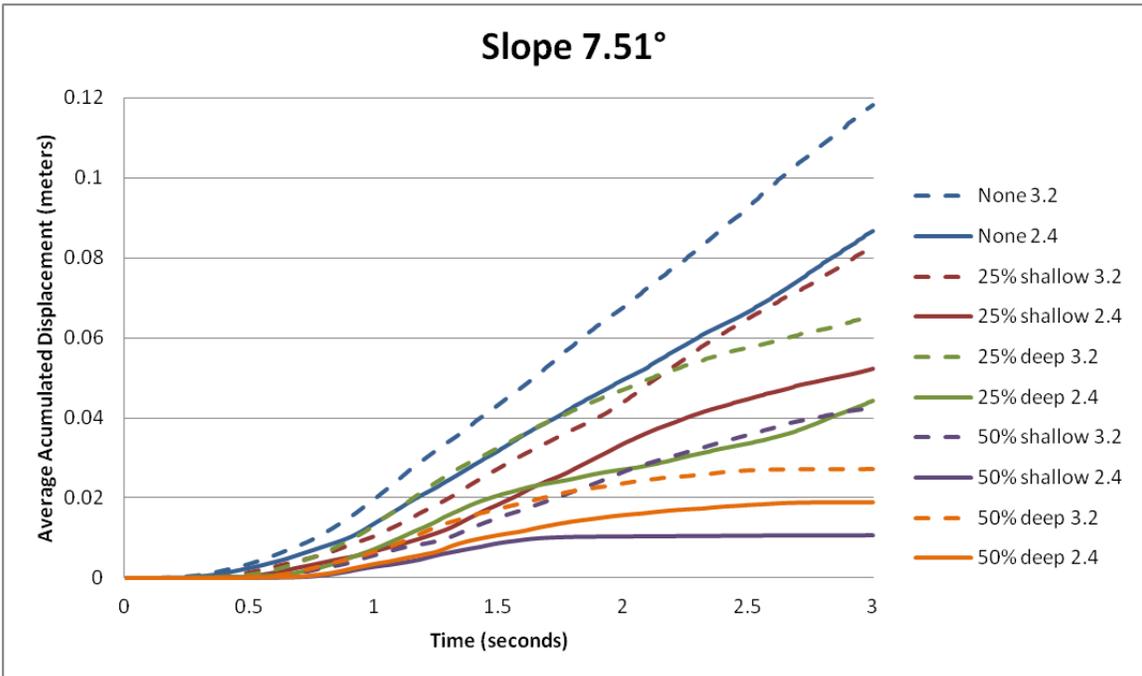
Figure
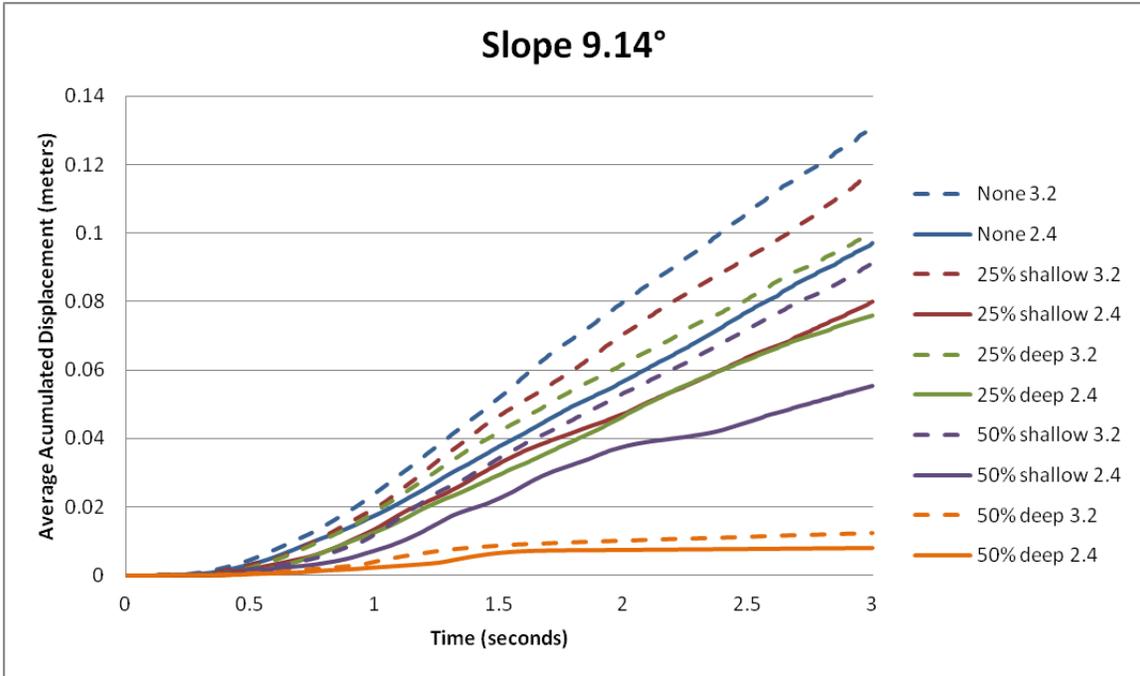
Figure
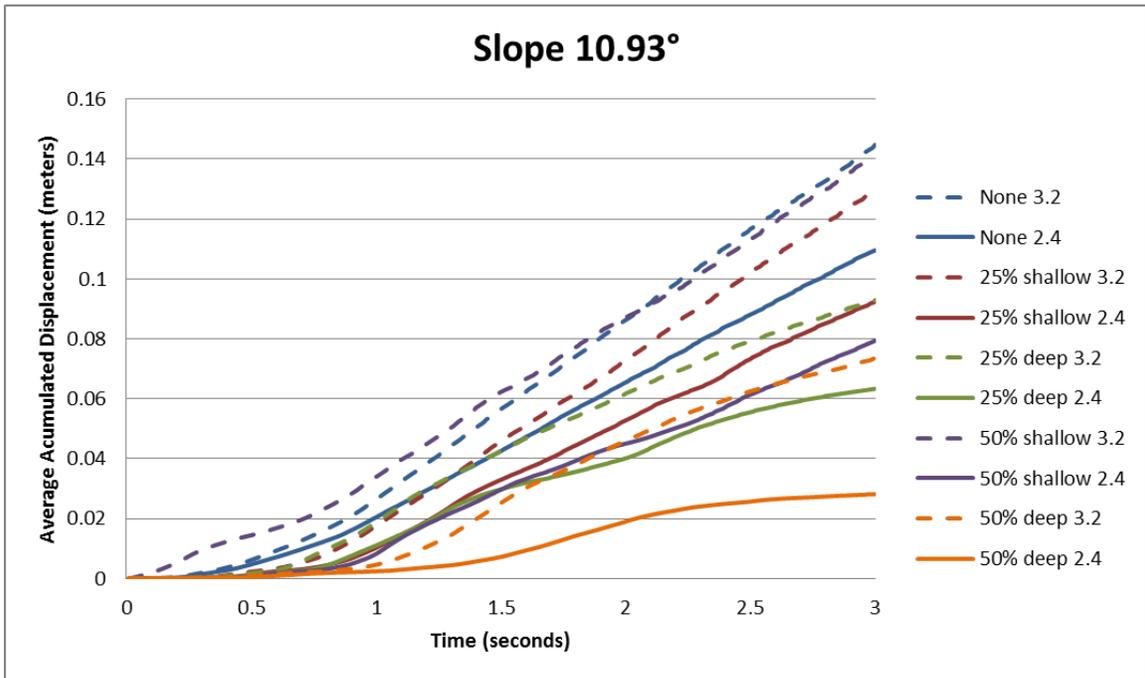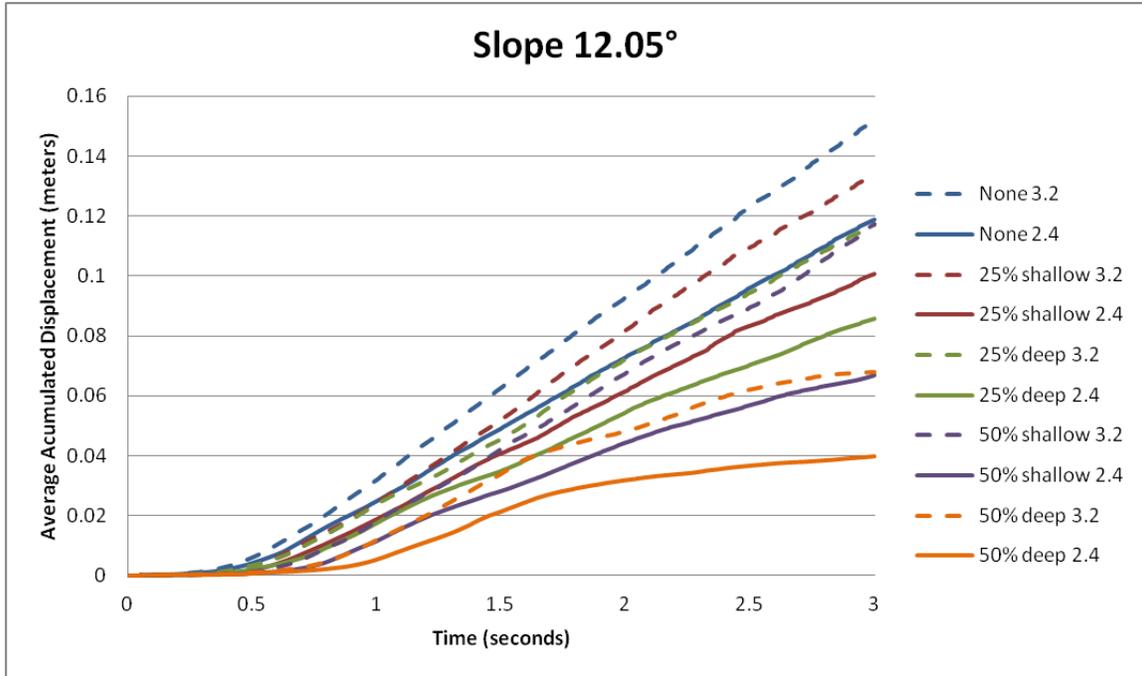
Figure

Figure

Next,
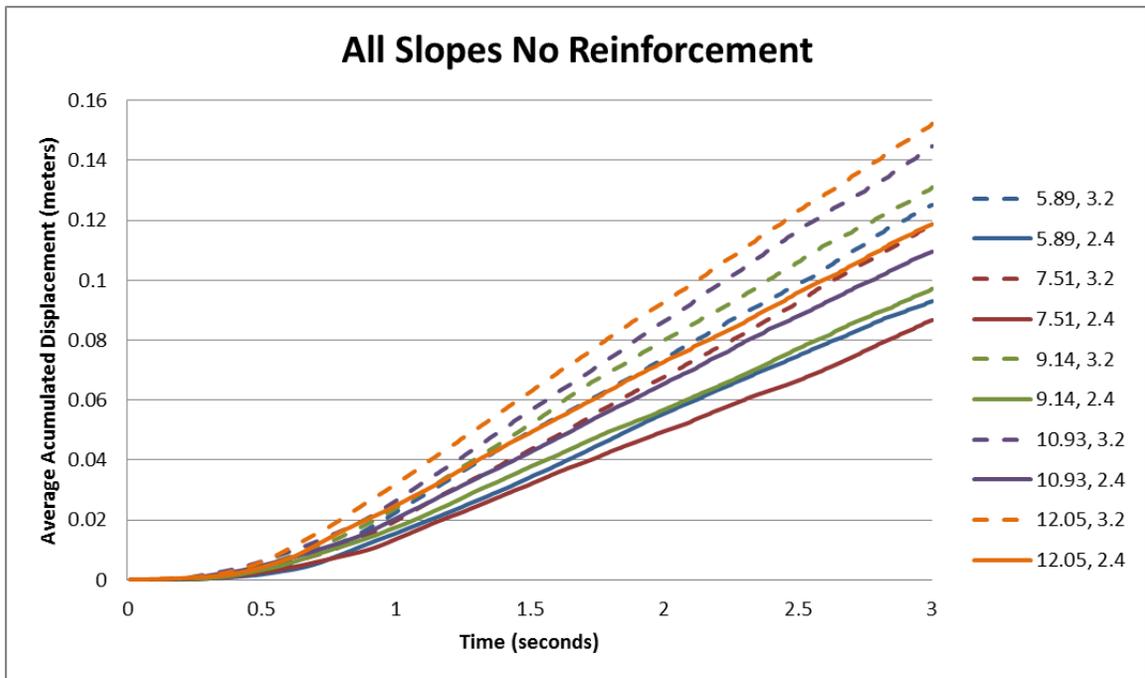
Figure

3.3.1.8.2

To

Table

	Drag				
	Reinforcement				
Slope	*None*	*25%*	*25%*	*50%*	*50%*
Slope	9.3%	8.3%	2.6%	0.8%	0.4%
Slope	6.5%	1.9%	2.6%	0.0%	0.0%
Slope	8.4%	5.3%	4.1%	3.1%	0.0%
Slope	10.3%	8.8%	4.5%	7.5%	0.5%
Slope	11.5%	9.6%	5.8%	4.3%	1.9%
	Drag				
	Reinforcement				
Slope	*None*	*25%*	*25%*	*50%*	*50%*
Slope	11.9%	12.0%	7.5%	4.5%	0.8%
Slope	9.7%	4.8%	5.0%	2.4%	1.0%
Slope	11.7%	9.3%	6.9%	6.1%	0.1%
Slope	13.7%	12.8%	7.7%	14.5%	4.8%
Slope	15.1%	11.9%	10.3%	10.3%	5.9%

3.3.1.8.3

Next,

Table

Drag					
	Reinforcement				
Slope	*None*	*25%*	*25%*	*50%*	*50%*
Slope	-	-	-	-	-
Slope	-	-	-	-	-
Slope	-	-	-	-	-
Slope	-	-	-	-	-
Slope	-	-	-	-	-

Drag					
	Reinforcement				
Slope	*None*	*25%*	*25%*	*50%*	*50%*
Slope	0.51	0.20	-	-	-
Slope	-	-	-	-	-
Slope	0.55	1.03	-	-	-
Slope	-	-	-	-	-
Slope	-	-	-	-	-

To

Table

Drag					
	Reinforcement				
Slope	*None*	*25%*	*25%*	*50%*	*50%*
Slope	83%	54%	12%	33%	-
Slope	78%	62%	31%	11%	10%
Slope	69%	72%	44%	47%	0%
Slope	67%	60%	28%	52%	9%
Slope	73%	50%	36%	34%	15%

Drag					
	Reinforcement				
Slope	*None*	*25%*	*25%*	*50%*	*50%*
Slope	109%	103%	54%	77%	12%
Slope	98%	74%	28%	33%	22%
Slope	106%	111%	55%	90%	2%
Slope	89%	82%	61%	93%	33%
Slope	95%	88%	56%	80%	18%

Comparing

Finally,

3.3.2

3.3.2.1

Again

3.3.2.2

The

Table

BC	Type	a	b	c	d
1	rigid	0	0	1	-
2	rigid	0	1	0	-
3	rigid	0	-	0	1.05
4	rigid	1	0	0	-
5	rigid	-	0	0	1.25
6	save	1	0	0	-

A
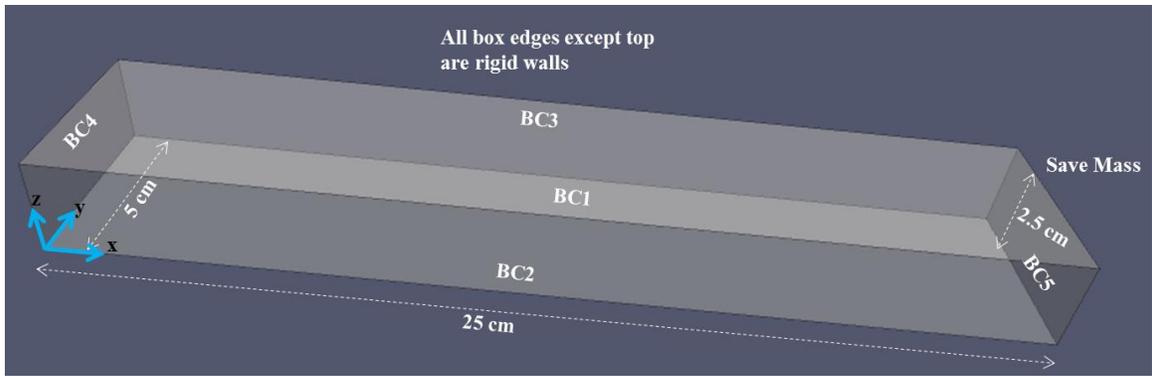
Figure

3.3.2.3

Originally,
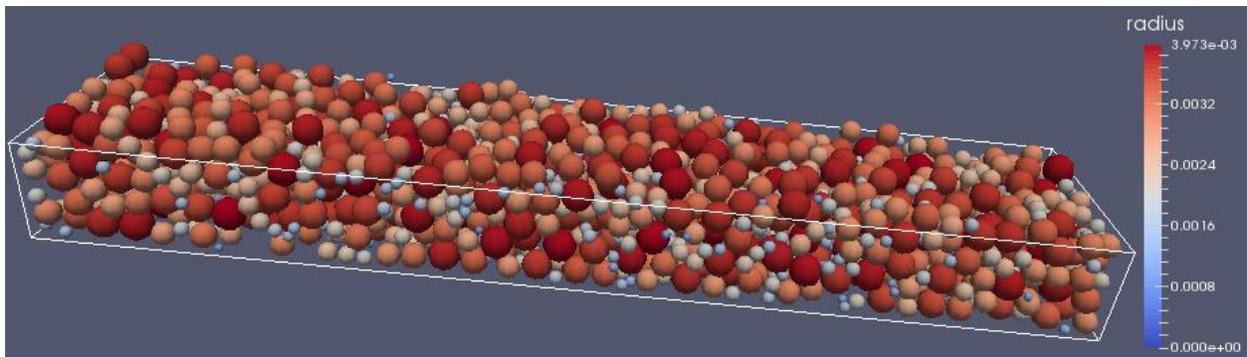
Figure
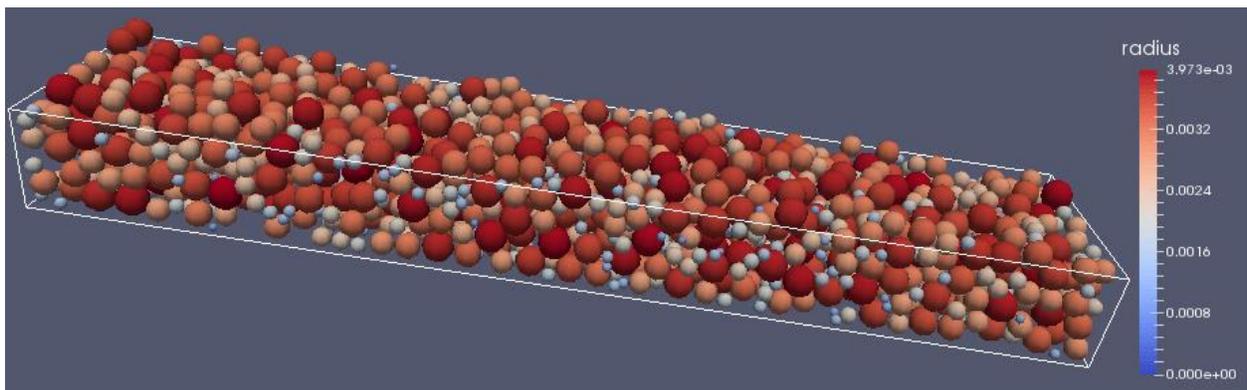
Figure
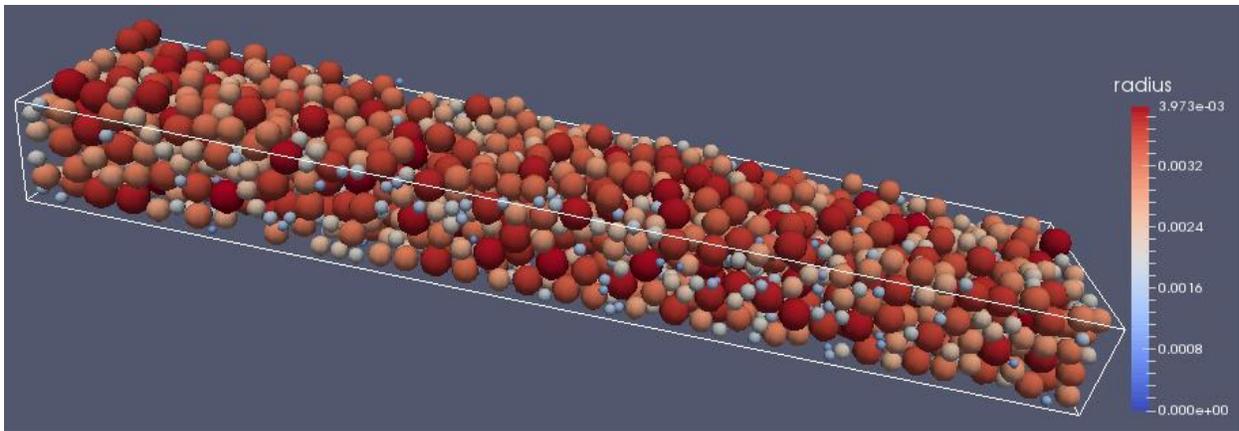
Figure

3.3.2.4

From

Figure

Figure

No 10%

25% 50%

Figure

No 10%

25%   50%

Figure

No   10%

25%   50%
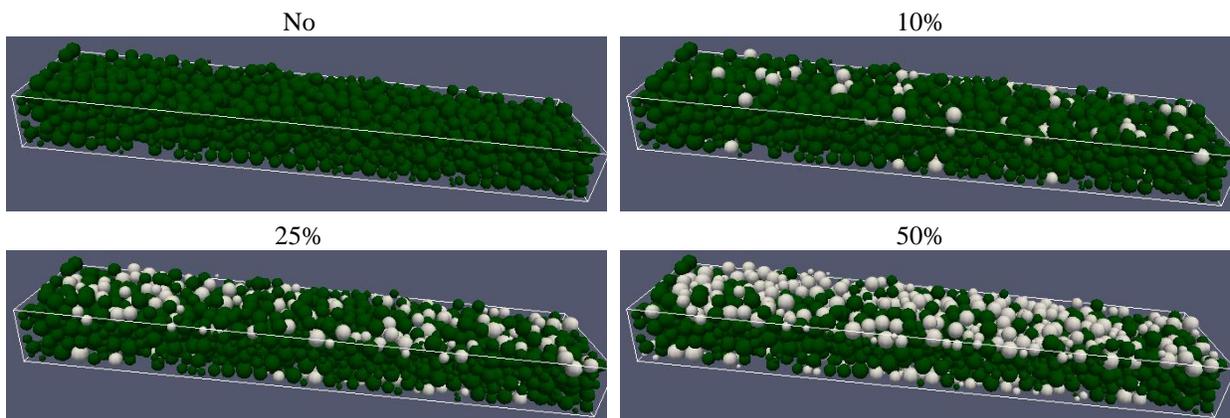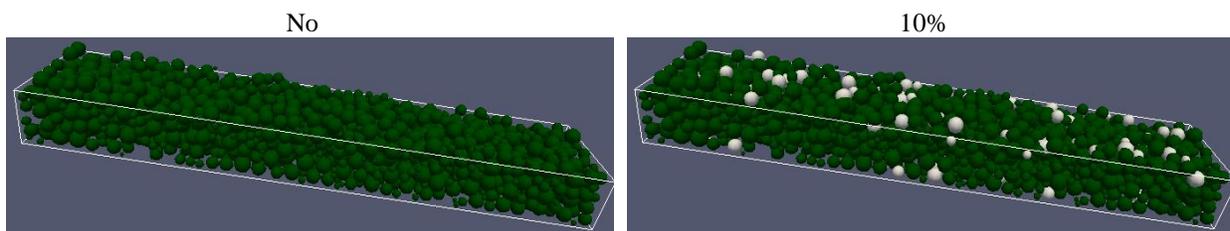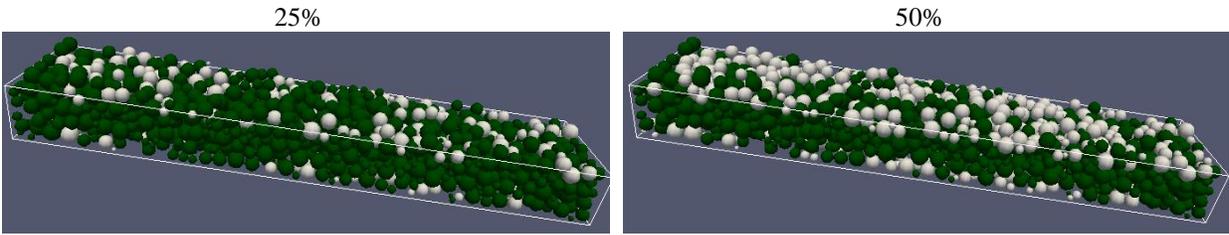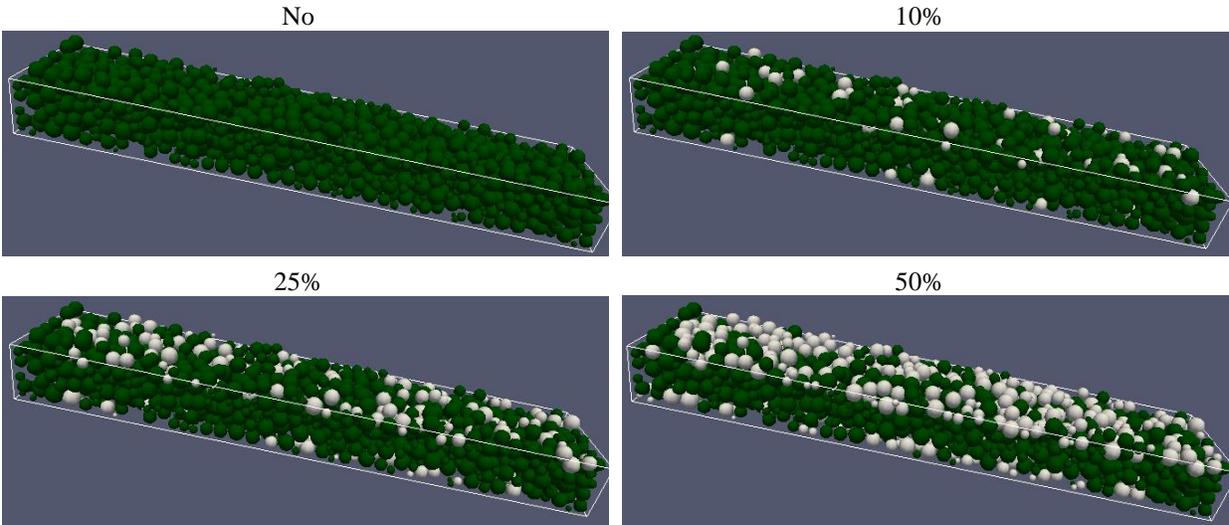
Figure

3.3.2.5

A

g

a

i

n

,

The drag forces were only applied to surface particles and particles were assigned as surface

particles if their centroid z location was above z_{surf}, calculated by

e

103

r

$$z_{surf} = 1.5(z_{ave} - 1) + 1 \qquad\qquad \textbf{[Equation 43]}$$

where z_{ave} is the average z location of all particles and the plus and minus 1 is because the bottom

left corner of the particle boundary is not located at the origin of the coordinate system, but rather

at (1m,1m,1m) as described above. Once a particle is assigned as a surface particle, the actual

magnitude of the drag force applied to the particle is a linear function of depth. More specifically,

a particle i at time step t, that has already been identified as a surface particle, has a drag force

e

q

u

a

$$\text{if } z_i \leq 2(z_{ave} - 1) + 1$$

$$\boldsymbol{z_{mult}} = \left(\frac{2}{z_{ave}-1}\right) \boldsymbol{z_i} - 3 - \left(\frac{2}{z_{ave}-1}\right) \qquad\qquad \textbf{[Equation 44]}$$

else

$$\boldsymbol{z_{mult}} = \boldsymbol{1} \qquad\qquad \textbf{[Equation 45]}$$

z_{mult} is a minimum of 0 for particles with a z value of z_{surf} (lowest surface particles) and this is

t

proven by plugging in $z_{surf} = 1.5(z_{ave} - 1) + 1$ for z_i in $\boldsymbol{zmult} = \left(\frac{2}{z_{ave}-1}\right) \boldsymbol{z_i} - 3 - \left(\frac{2}{z_{ave}-1}\right)$

o

[Equation **44**

$$z_{mult} = \left(\frac{2}{z_{ave}-1}\right)[1.5(z_{ave}-1)+1] \cdot 3 \cdot \left(\frac{2}{z_{ave}-1}\right) = 3 + \left(\frac{2}{z_{ave}-1}\right) - 3 - \left(\frac{2}{z_{ave}-1}\right) = 0 \checkmark \text{ with}$$

z_{mult} calculated as m of 1 for particles with a z value equal to or greater than $2(z_{ave} - 1) + 1$ and

this is proven by plugging in $2(z_{ave} - 1) + 1$ for z_i in $\boldsymbol{zmult} = \left(\frac{2}{z_{ave}-1}\right) \boldsymbol{z_i} - 3 - \left(\frac{2}{z_{ave}-1}\right)$

[Equation **44**

$$z_{mult} = \left(\frac{2}{z_{ave}-1}\right)[2(z_{ave}-1)+1] - 3 - \left(\frac{2}{z_{ave}-1}\right) = 4 + \left(\frac{2}{z_{ave}-1}\right) - 3 - \left(\frac{2}{z_{ave}-1}\right) = 1 \checkmark$$

A schematic of how z_{mult} (and therefore $F^t_{drag_i}$) varies through the depth of the particle packing

is shown in Figure 41.
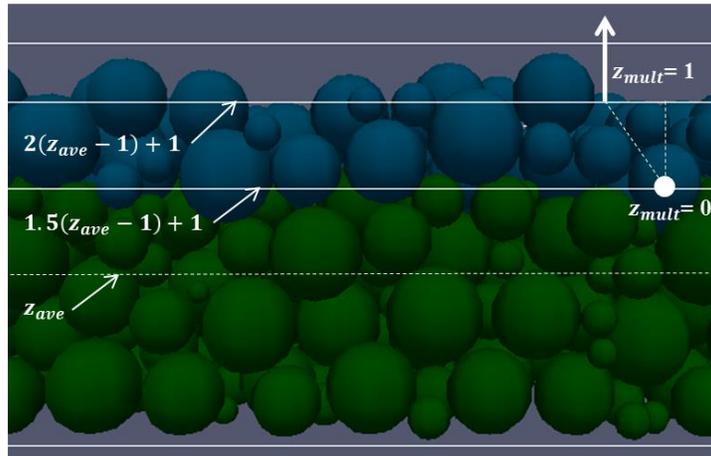
Figure 41. Schematic of which particles are assigned as surface particles and what magnitude multiplier is assigned for drag force calculations.

One case, Slope 12º non-reinforced for a fluid velocity of 0.5 m/s is shown in

Figure 42 at 0, 1.5, 3, and 4.5 seconds to show an example of how particles are being assigned as surface particles. The blue particles are surface particles and have the drag force applied to them, with a magnitude according to the z_{mult} depth function described above.

| 0 sec | 1.5 sec |

| 3 sec | 4.5 sec |
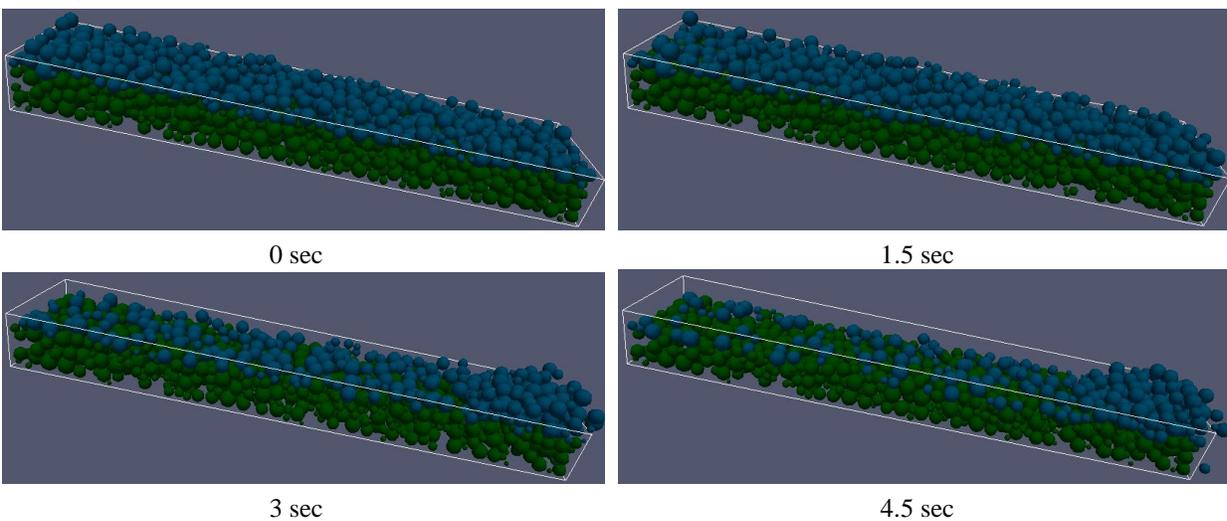
Figure 42. Slope 12º Non-reinforced and 0.5 m/s Fluid Velocity. Blue particles are surface particles.

3.3.2.6 Input Parameters for 3D Simulations

Coarse sand material properties were used for the force calculations in the model. The root reinforcement stiffness was chosen to be 20,000 N/m and this value is roughly 20-60x the normal stiffnesses between the particles (see explanation above in Input Parameters for 2D Simulations). Other constants for all of the simulations include the acceleration due to gravity of 9.81m/s and a sufficiently small time step increment of 1.0 x 10^{-6} second. This value is one-millionth of a second, dt in all relevant equations, and was checked to be less than dt_{crit} in $\boldsymbol{dtcrit} = \frac{\pi R_{min}}{\alpha} \sqrt{\frac{\rho}{G}}$

[Equation 15. The simulations were run for at least 3 seconds and some up to 7.5 seconds of simulation time, depending on the amount of particle movement. This results in a total of between 3 million and 7.5 million time steps for the simulations.

All input parameters are summarized in Table R and the third column gives information on where the variable is used.

Table R. Input Parameters for 3D Simulations

Parameter (units)	Value	Needed For
Number of Particles	2400	-
Density (kg/m^3)	1850 (APPC-Soil)	gravitational loading
Poisson's Ratio	0.15 (APPC-Soil)	i

Modulus of Elasticity (GPa)	20 (APPC-Soil)	used to calculate G in $Knt= \left(\frac{2\langle G\rangle\sqrt{2\langle R\rangle}}{3(1-\langle v\rangle)}\right)\sqrt{\delta_n^t}$	[Equation 17
dt (sec)	10^{-6}		time increment for time stepping
K_r (N/m)	20,000	K_{spring} in $Fspringjt= K_{spring}^t\left(\delta_{spring}^t - \delta_{spring1}^t\right)\frac{d_{springj}^t}{\left|d_{spring}^t\right|}$	[Equation 41
Friction angle	31°	$\tan(31°) = \mu$ in $Ftjt= -min\left(\left|\mu F_{nj}^t\right|, F_{tj}^t(\delta_t, \dot{\delta}_t)\right)\frac{\dot{\delta}_t}{\left|\dot{\delta}_t\right|}$	[Equation 32
Global damping coefficient	25		i n
Particle-particle contact damping coefficient	0.15	μ_c in $Fdampjt= -\mu_c K_n^t\delta_n^t$	[Equation 37

3.3.2.7

Similar

3.3.2.8

For

3.3.2.8.1

There

Figure
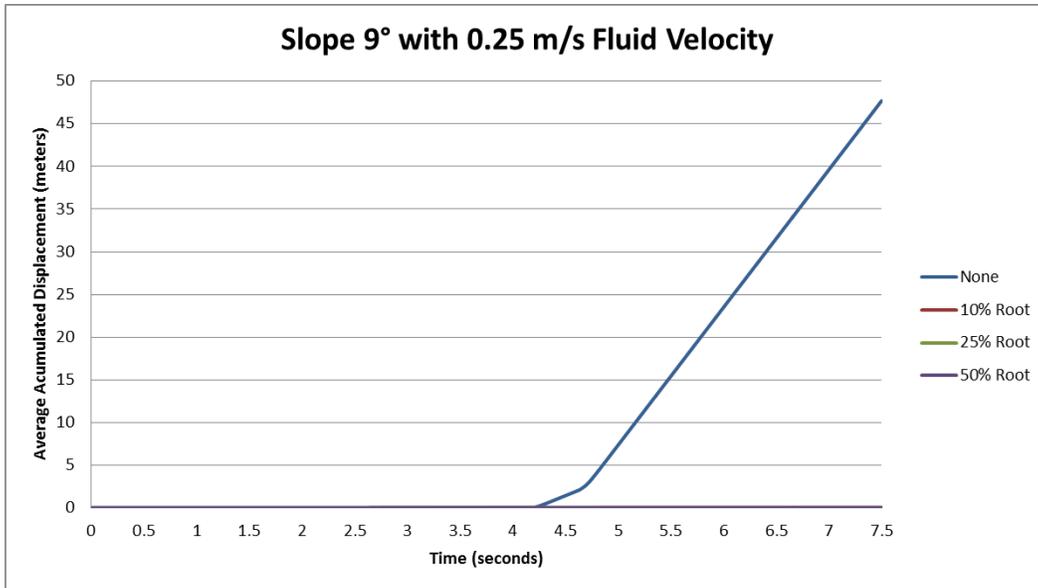
Figure
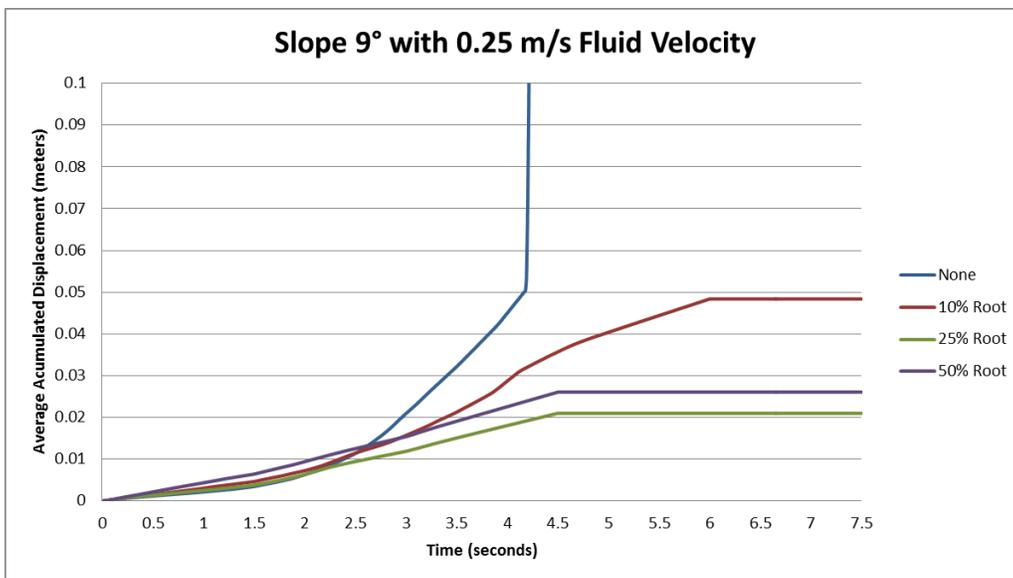
Figure
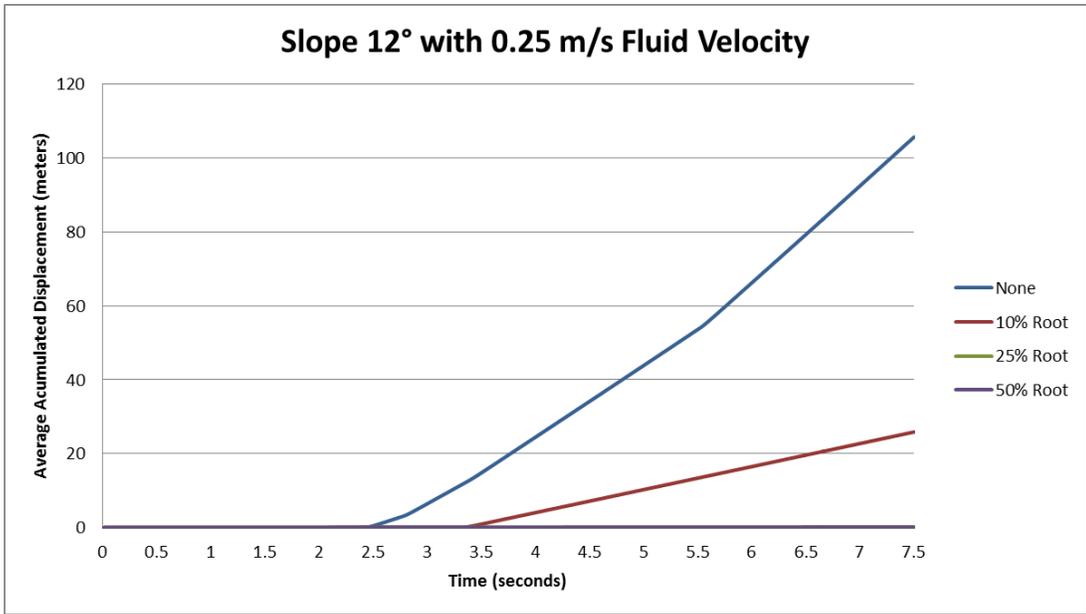
Figure

Next,
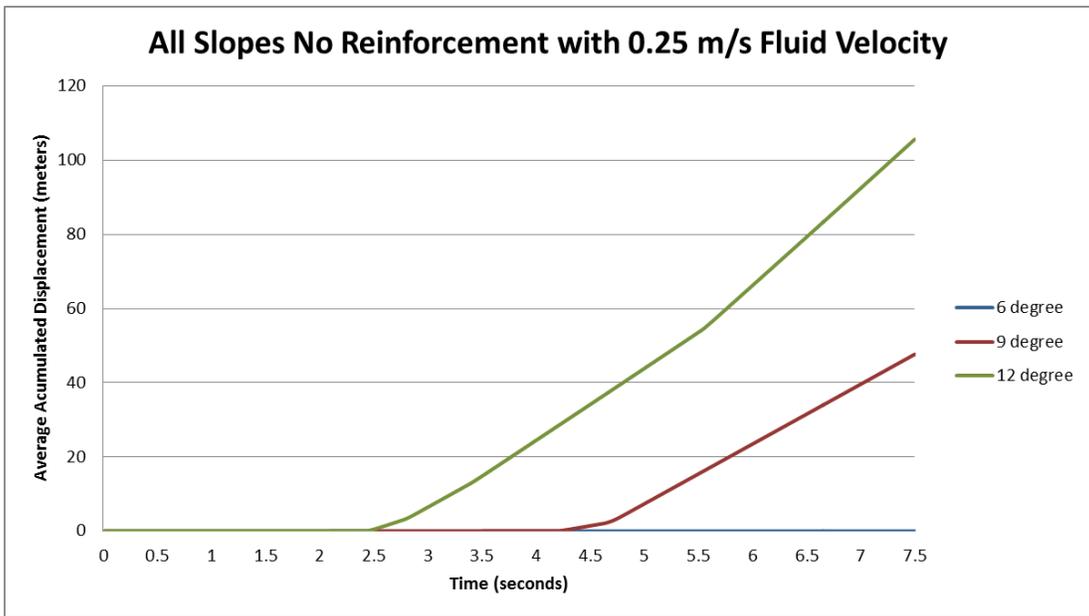
Figure

Table

0.5			
	Reinforcement		
Slope	*None*	*10%*	*25%*	*50%*
Slope	25.5%	18.8%	10.1%	2.1%
Slope	27.0%	20.6%	13.6%	4.8%
Slope	32.2%	24.1%	16.4%	5.7%

3.3.2.8.3

Finally,

CHAPTER

4.1

The

▪ The amount of runoff and erosion increased with a decrease in the amount of natural surface vegetation on the block samples. Burning the surface vegetation did not directly increase runoff, but burning did lead to an increase in erosion.

▪ The presence of straw mulch on the surface of a burned block sample reduced runoff rates and sediment concentrations relative to burned block samples without ground cover by providing layer above the soil to dissipate energy of raindrop impact and temporarily store precipitation. Straw mulch also reduced erosion via acting as a barrier to entrap dislodged soil particles, preventing them from moving further downslope.

- Burned block samples generally produced higher runoff and erosion during a subsequent rainfall simulation (second simulation) when compared to a prior rainfall simulation (first simulation).

- Burning exponentially increased erosion compared to unburned conditions. Also, straw mulch reduced burned soil erosion to levels consistent with unburned samples that had natural vegetation.

- Increasing runoff from burned block samples with no ground cover resulted in increased sediment yield. Surface cover, whether natural vegetation or straw mulch, prevented increasing runoff and increasing sediment yields.

- The ash layer on the burned soil surfaces had high infiltration capacity and acted as a water storage layer. A hydrophobic layer was identified below the ash layer on the burned soil surfaces. This hydrophobic layer prevented water infiltration from the wettable ash layer deeper into the soil, which increased runoff from burned samples during the second rainfall simulation. Straw mulch helped protect the ash layer from eroding during rainfall simulations, which helped maintain the ability of the ash layer to provide water storage.

- Notable changes in soil physical characteristics and hydraulic and mechanical properties with high severity burning were not found in this study. Similarities in surface dry density, organic matter, field saturated hydraulic conductivity, and shear strength between unburned and burned soil samples suggest that the observed increases in erosion on bare burned samples during rainfall simulations could be attributed to destruction of surface cover with burning.

Although

4.2

Root

- Higher displacements and larger percent sediment yields occurred with higher drag forces or faster overland flow.

- The root reinforcements acted to inhibit particle movements, reduce sediment yields, and stabilize the slopes.

- Increasing the amount of root reinforcements, simulating root growth over time after a fire, decreased particles movement downslope and the total amount of sediment yield.

- In general, steeper slopes were associated with higher particle movements and larger sediment yields than less steep slopes subjected to the same drag forces.

The

4.3

The

1. Surface vegetation of post-burned soil slopes should be evaluated immediately following a wildfire and areas with high-burn severity (e.g., surface vegetation completely removed via burning) should have ground treatment applied to mitigate erosion and runoff;

2. Straw mulch used as a ground cover should be applied at a rate of at least 0.06 kg/m^2 to reduce erosion to conditions relative to in-tact vegetation; and

3. Seeding should be applied along with ground cover application to promote re-establishment of surface vegetation to mitigate erosion and runoff long-term.

Although

REFERENCES

Ahrens,

Anderson,
APPC-
ASTM
ASTM
ASTM
ASTM
ASTM
ASTM
ASTM
ASTM
Baron,
Bautista,
Benavides-
Beyers,
Bossy,
Bruggink,
Burned
Burroughs,
Cannon,
Chung,
Chung,
Coetzee,
Cofie,
Commandeur,
Conrad,
Cui,
Cundall,
Cundall,
Dalaeli,
DeBano,
DeBano,
Doerr,
Doerr,
Ebel,
Elliott,
Foltz,
Foltz,
Foerster,
Fried,
Graham,
Ice,
Julien,
Kharaz,
Kilinc,
Lade,
Larsen,

Lee,
Lynch,
MacDonald,
MacDonald,
MacDonald,
Maw,
Mindlin,
Moody,
Moody,
Moody,
Morgan,
Munjiza,
Murphy,
Napper,
Neary,
Neary,
Ng,
Ning,
O'Sullivan,
Padros,
Pietraszek,
Ravi,
Regmi,
Renzo,
Robichaud,
Robichaud,
Robichaud,
Robichaud,
Robichaud,
Robichaud,
Robichaud,
Roby,
Santi,
Schmeer,
Schmeer,
Schumacher,
Sheng,
Thornton,
Timoshenko,
United
Verdin,
Vu-
Vu-
Wieting,
Wischmeier,
Woods,

Wu,
Yanosek,
Zavala,
Zhang,
Zhang,
Zhu,

APPENDIX

Figure

Arapaho- Roosevelt Soil Sample Collection Area

Legend

soil testing area

0 0.1 0.2   0.4   0.6   0.8
Miles

By: Kayla Moden

Sources: Esri, HERE, DeLorme, Intermap, increment P Corp., GEBCO, USGS, FAO, NPS, NRCAN, GeoBase, IGN, Kadaster NL, Ordnance Survey, Esri Japan, METI, Esri China (Hong Kong), swisstopo, MapmyIndia, © OpenStreetMap contributors, and the GIS User Community

Figure

Figure
APPENDIX

A

An

Temporal

Figure

Table

Test	Scenario	Specimen	Straw	Test	Rainfall
Sand-	1	90%	0	2	1
	2	80%	0	2	1
	3	70%	0	2	1
	4	70%	0.22	2	1
	5	70%	0.44	2	1
	6	60%	0	2	1
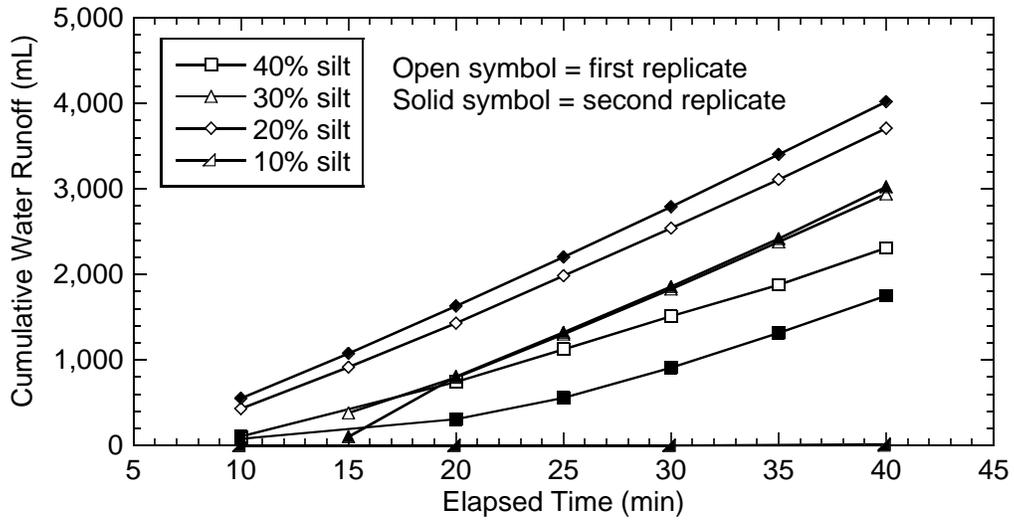
Figure

Relationships
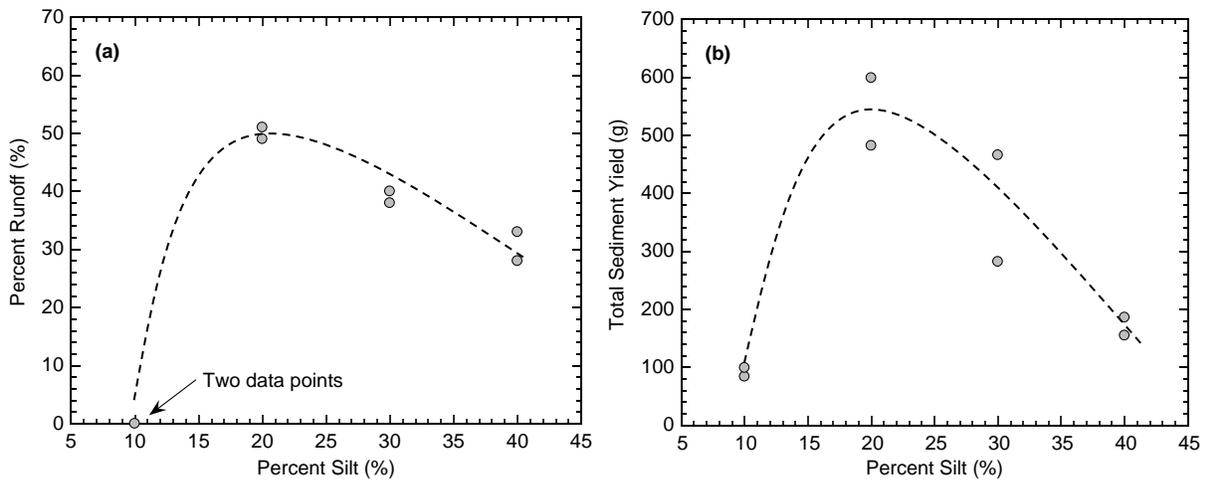
Figure

The

The

Temporal
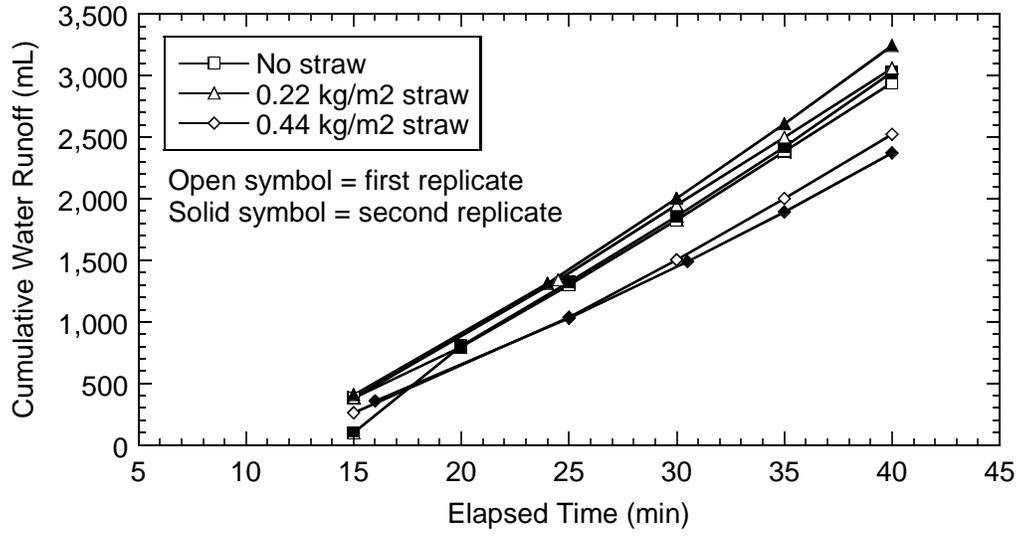
Figure

Relationships

The

Figure

Several

120
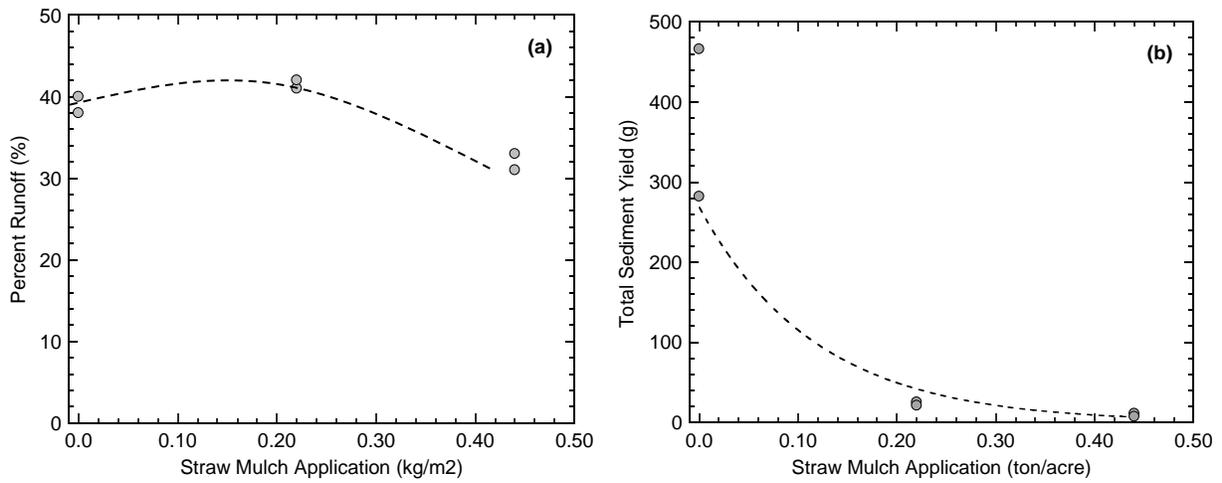
APPENDIX

thermocouple
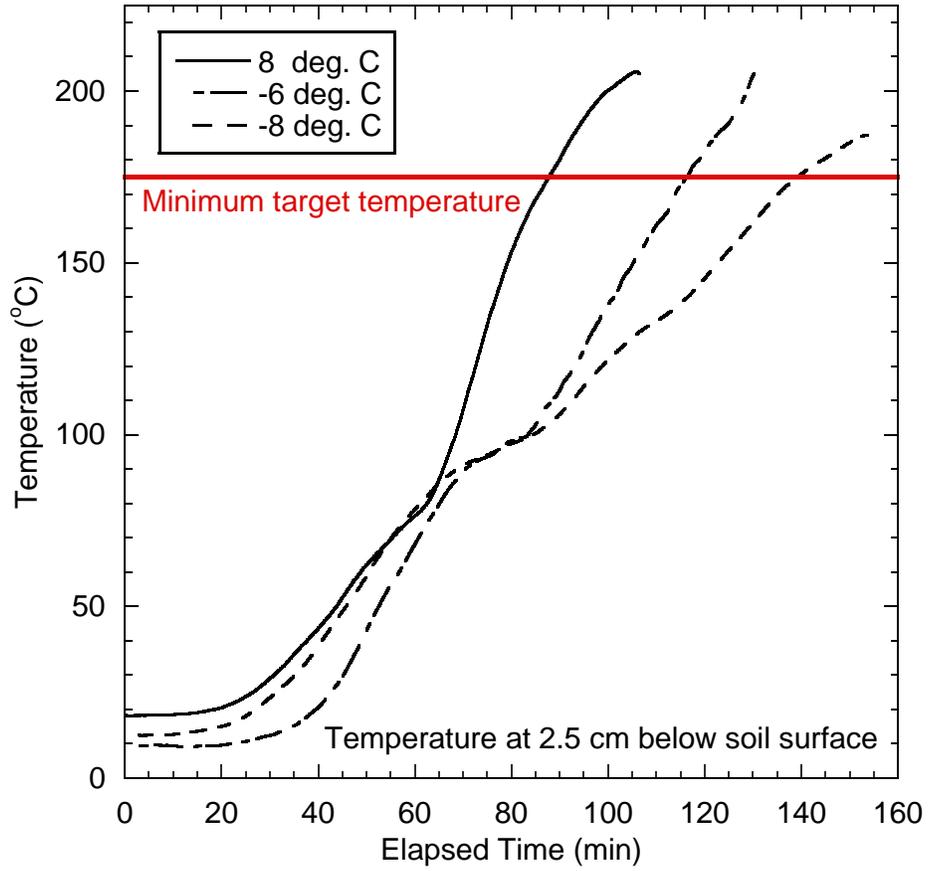
Figure

APPENDIX

Figure

Figure

Figure
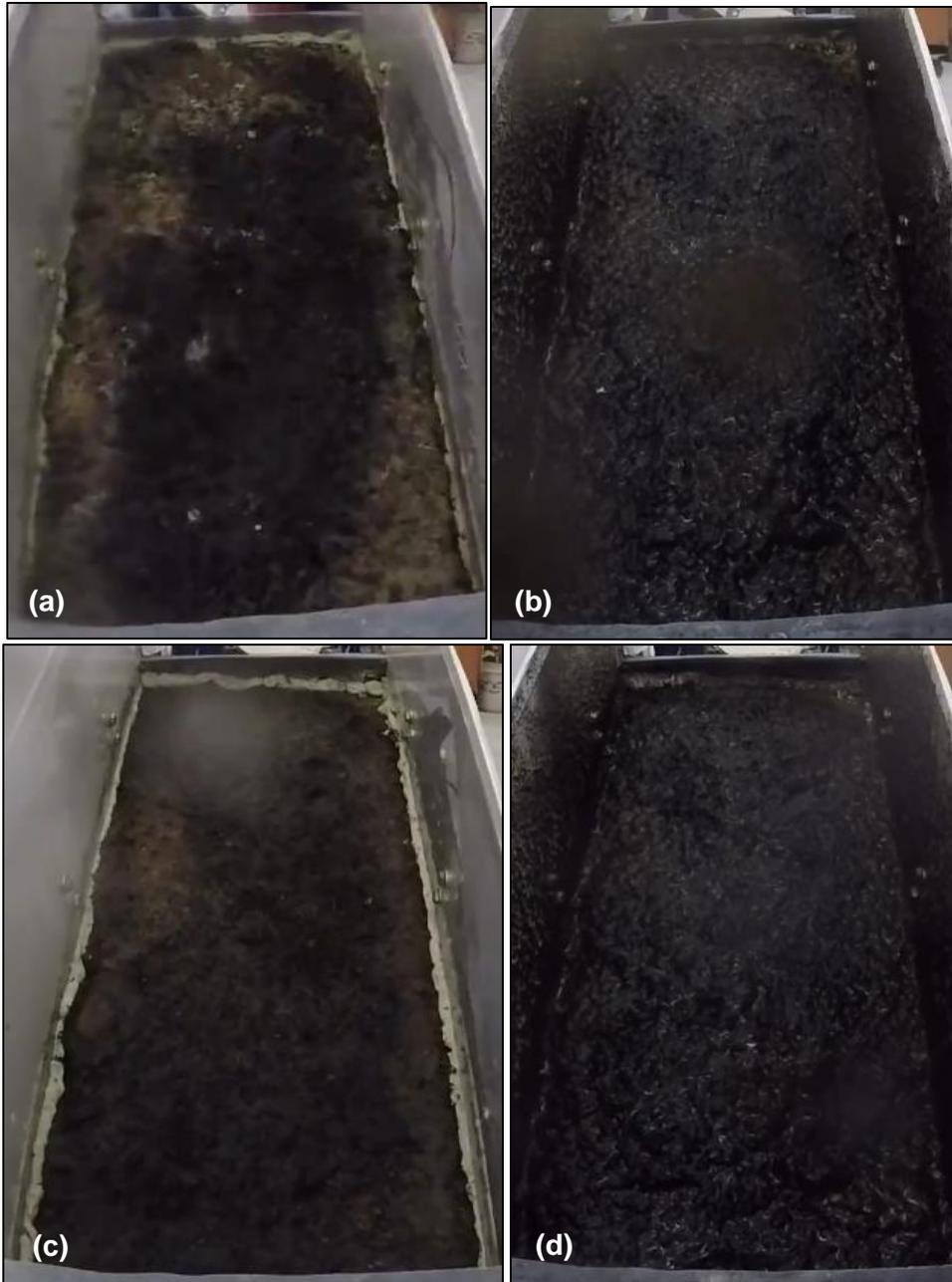
Figure

Figure

Figure

Figure

APPENDIX

Chung

Table

Test	Title	Objective	Reference(s)
1	Elastic	Check	Timoshenko
2	Elastic	Check	Timoshenko
3	Normal	Check	Ning
4	Oblique	Check	Foerster
5	Oblique	Check	Maw
6	Impact	Check	Vu-
7	Impact	Check	Chung
8	Impact	Check	Chung

Because

Table

Input	Test		Test		Test	
	Ex.	Ex.	Ex.	Ex.	Ex.	Ex.
	Glass	Limestone	Al.	Mg.	Al.	Cast
Young's	4.80E+10	2.00E+10	7.00E+10	4.00E+10	3.80E+11	1.00E+11
Poisson	0.20	0.25	0.30	0.35	0.23	0.25
Friction	0.350	0.350	0.000	0.000	0.000	0.000
Restitution	1.00	1.00	1.00	1.00	different	
Density	2800	2500	2699	1800	4000	7000
Radius	0.010	0.010	0.100	0.100	0.0025	0.0025
Velocity	±10	±10	0.2	0.2	3.9	3.9
Input	Test		Test			
	Ex.	Ex.	Ex.	Ex.		

	Al.	Al.	Al.	Copper
Young's	3.80E+11	7.00E+10	7.00E+10	1.20E+11
Poisson	0.23	0.33	0.33	0.35
Friction	0.092	0.092	0.400	0.400
Restitution	0.98	0.98	0.50	0.50
Density	4000	2700	2700	8900
Radius	0.0025	0.0025	0.100	0.100
Velocity	3.9	3.9	0.2	0.2

Figure

(a)

Figure

Table

Physical	DEM Ex.	DEM Ex.	Analytical Ex.	Analytical Ex.	Percent Ex.	Percent Ex.
Contact	40	54	40	54	0.00%	0.00%
Maximum	274	368	274	368	0.00%	0.00%
Maximum	10,701	7,110	10,697	7,108	0.04%	0.03%

By
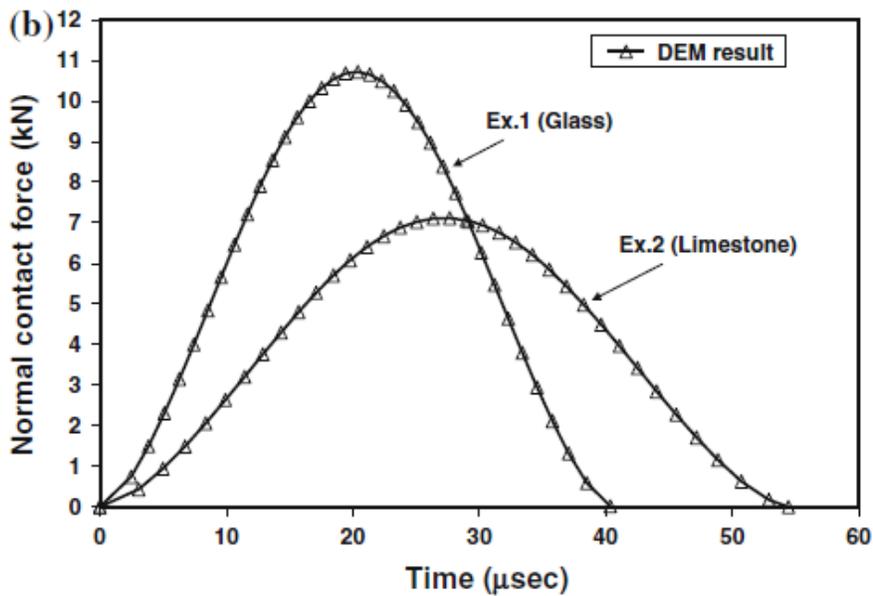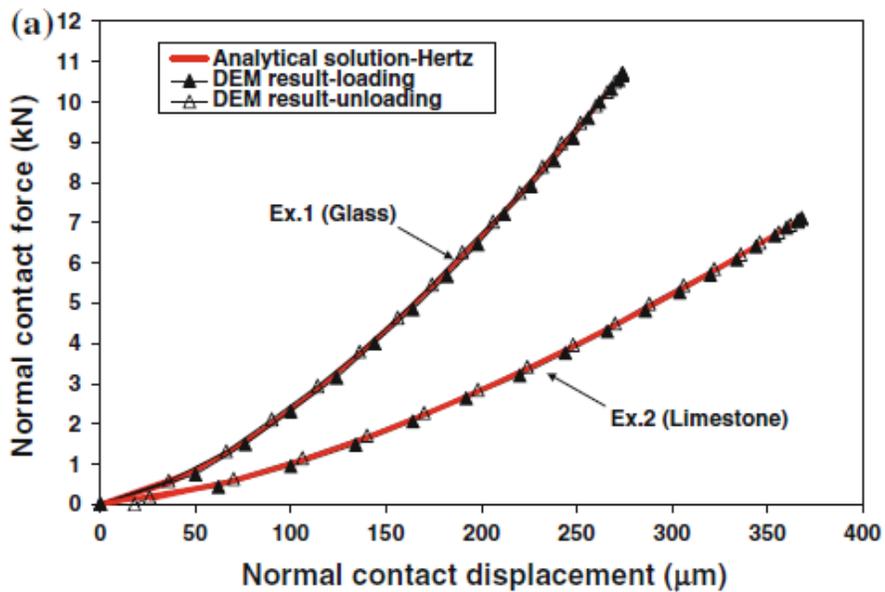
Figure

Figure

Table

Figure

(a)

Figure

Table

	DEM		Analytical		Percent	
Physical	Ex.	Ex.	Ex.	Ex.	Ex.	Ex.
Contact	731	767	731	766	0.00%	0.13%
Maximum	50	52	50	52	0.00%	0.00%
Maximum	11,370	7,233	11,370	7,233	0.00%	0.00%

By

Figure

Figure
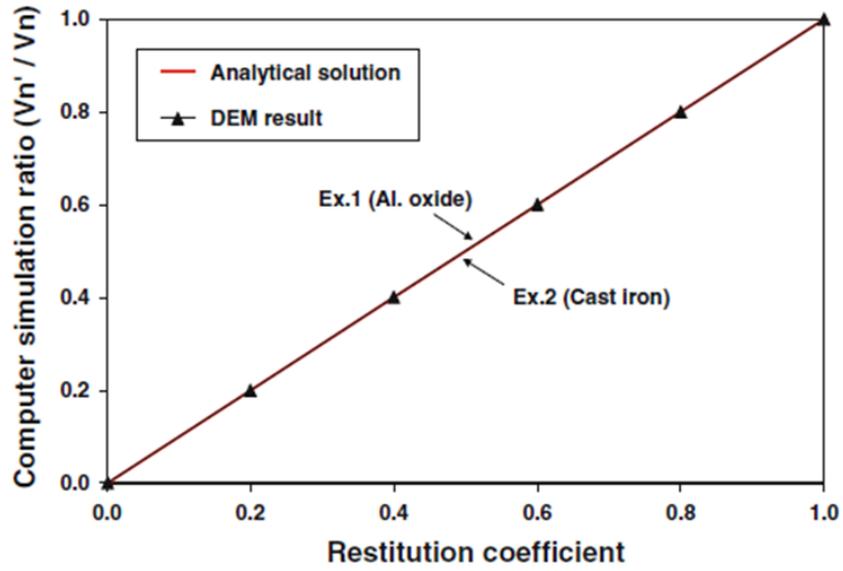
Figure
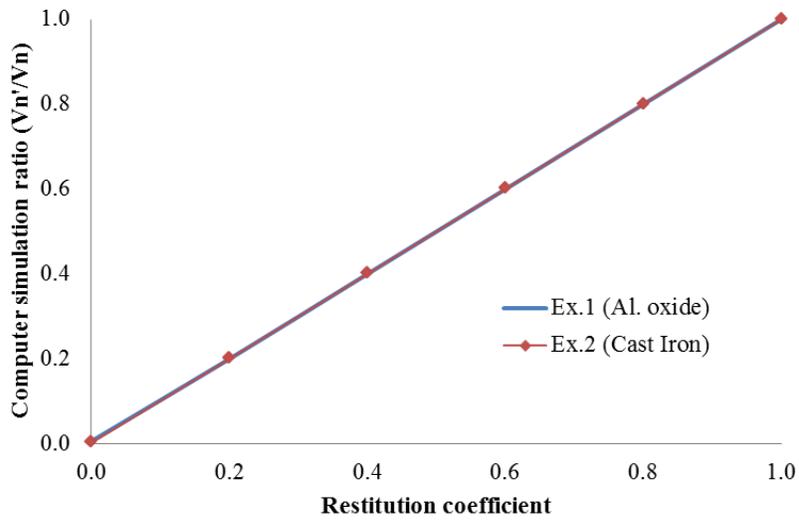
Figure
By

Figure

Figure
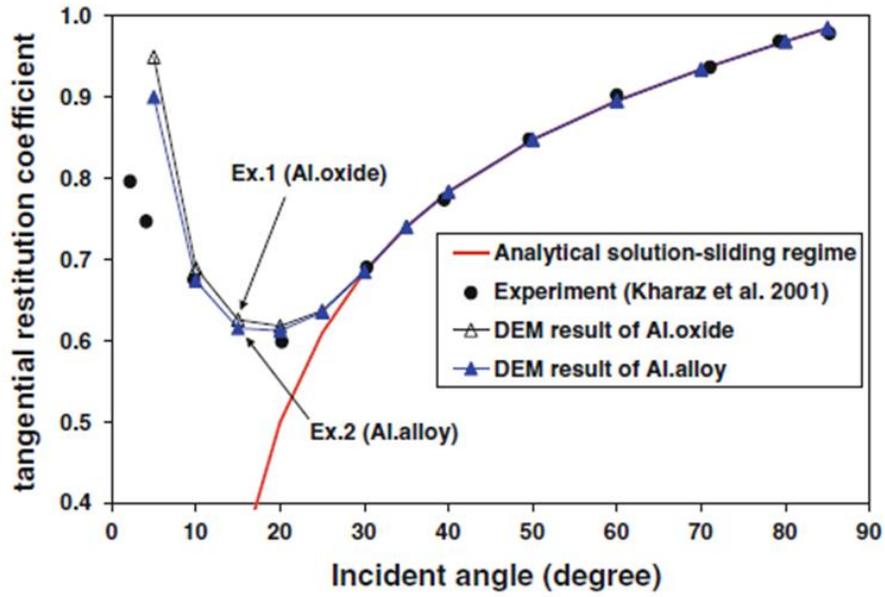
Figure
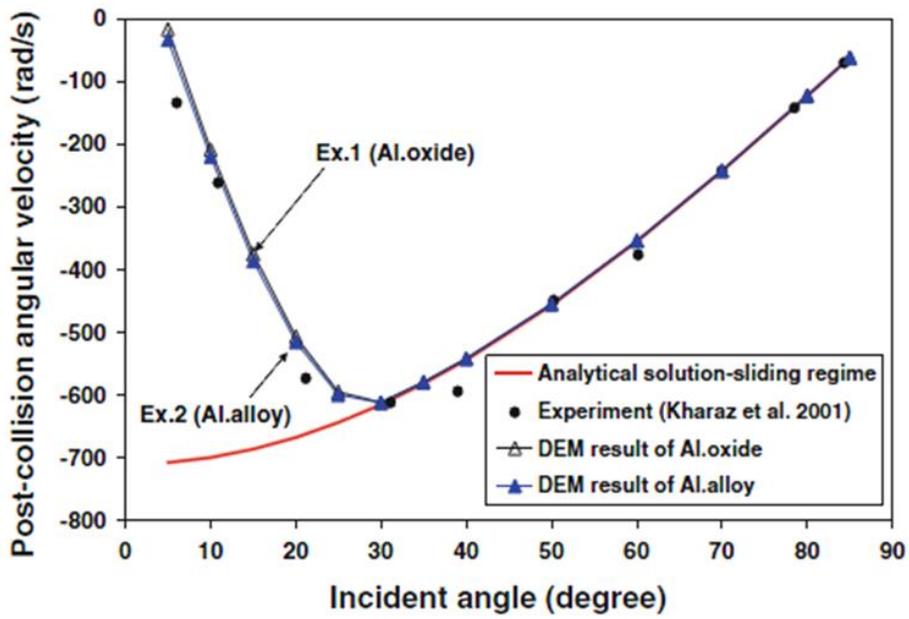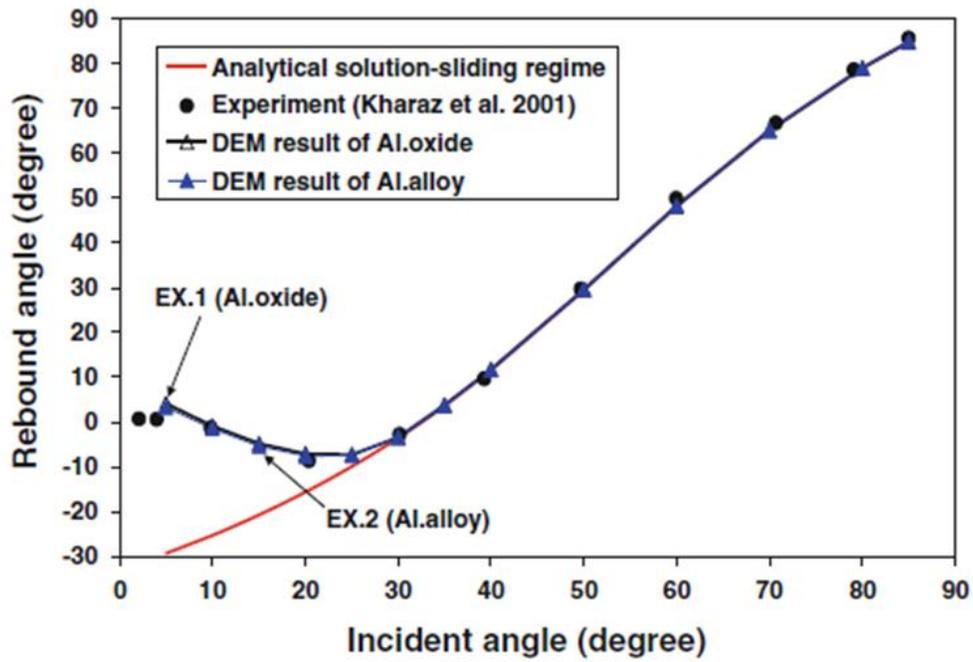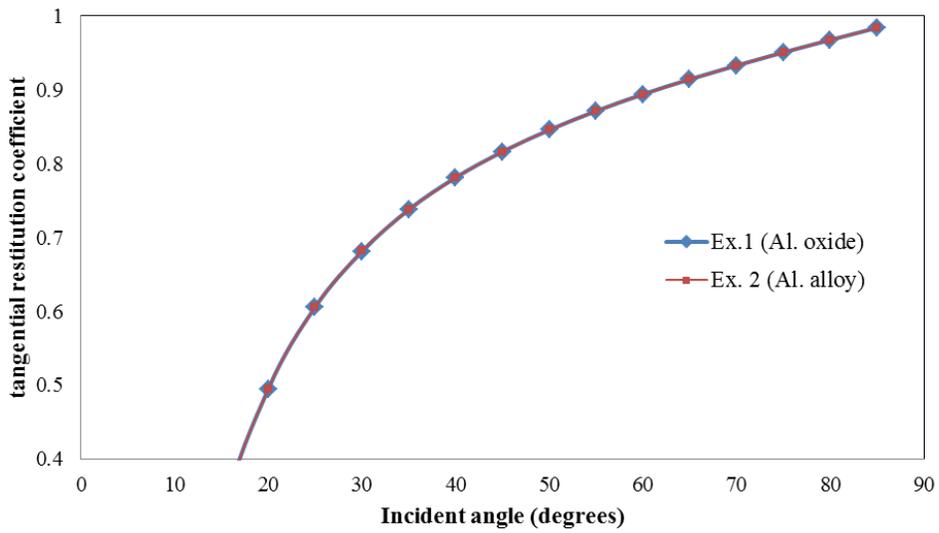
Figure
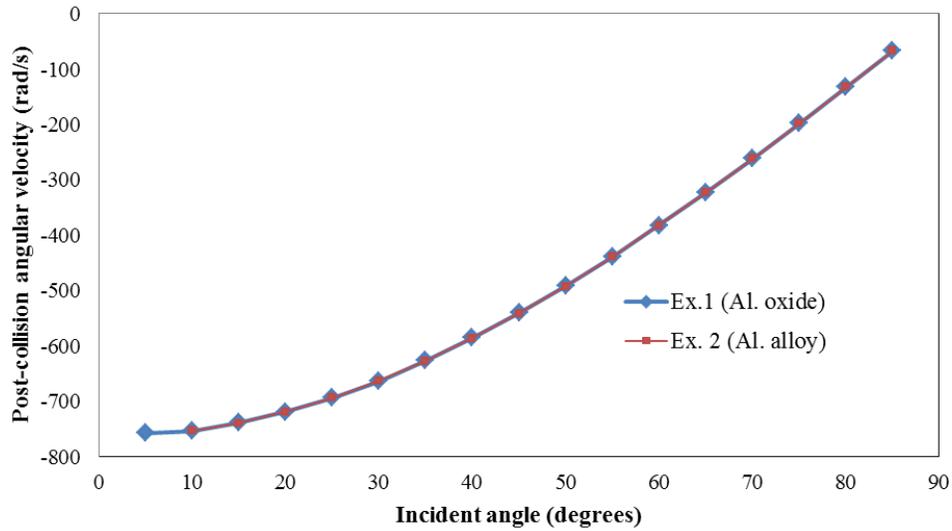
Figure
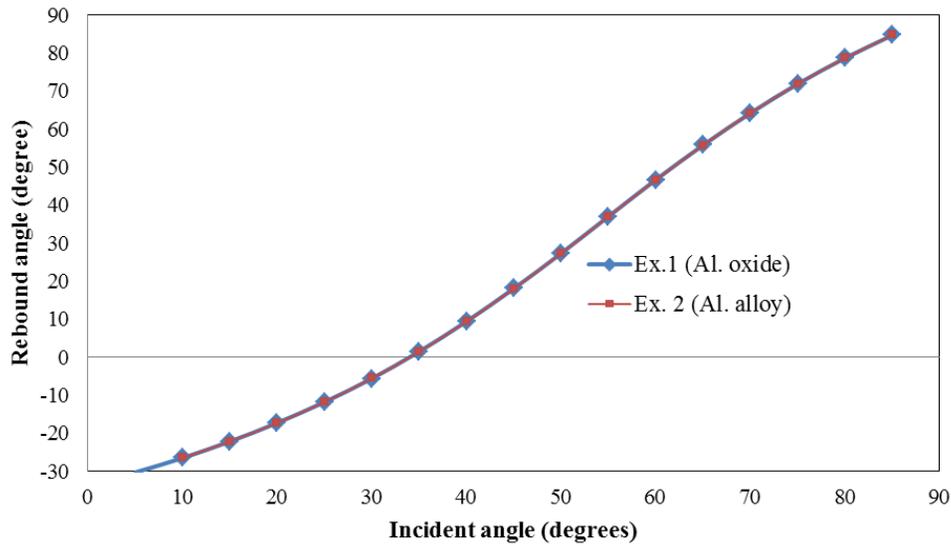
Figure

Figure

Figure

By comparing Figure 68 to Figure 71, Figure 69 to Figure 72, and Figure 70 to Figure 73, the DEM

model matches the analytical solutions for Test 4. The deviation of the published results from the

analytical solution below about 28° incident angle is due to the inaccuracy of the analytical solution

to predict behavior in the sticking regime. This discrepancy can be improved by using a more

complete Hertz-Mindlin contact model (Chung and Ooi 2011), whereas the DEM model used for

this research uses a Simplified Hertzian contact model (described by $Knt= \left(\frac{2\langle G\rangle\sqrt{2\langle R\rangle}}{3(1-\langle v\rangle)}\right)\sqrt{\delta_n^t}$

[Equation 17). However, because the simulations performed for this report do not involve particle velocities anywhere near the velocity used for this benchmark test (3.9 m/s), one assumption made is that the deviation from the analytical solution below the critical impact angle would have negligible effects on the simulations and that the analytical solution is accurate enough.
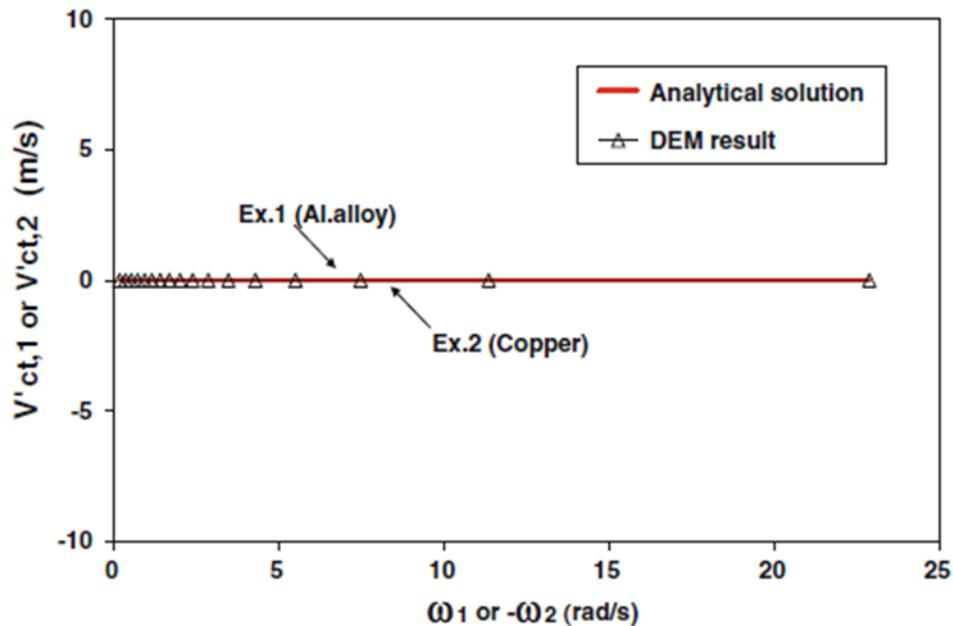
Figure 74. Test 7 published results for post-collision tangential velocity at the mass center for varying pre-collision angular velocities (Chung and Ooi 2011).
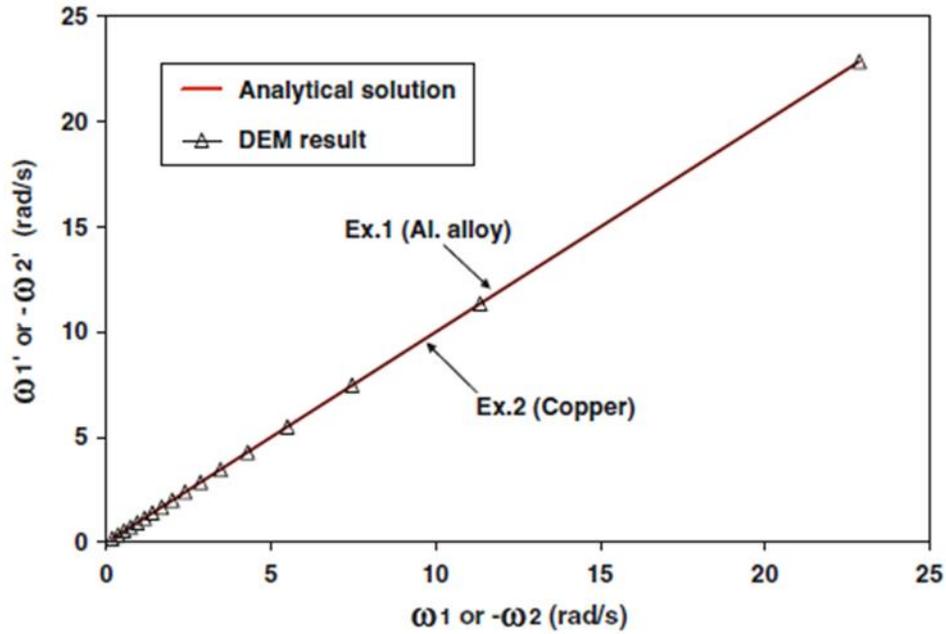
Figure 75. Test 7 published results for post-collision angular velocity for varying pre-collision angular velocities (Chung and Ooi 2011).
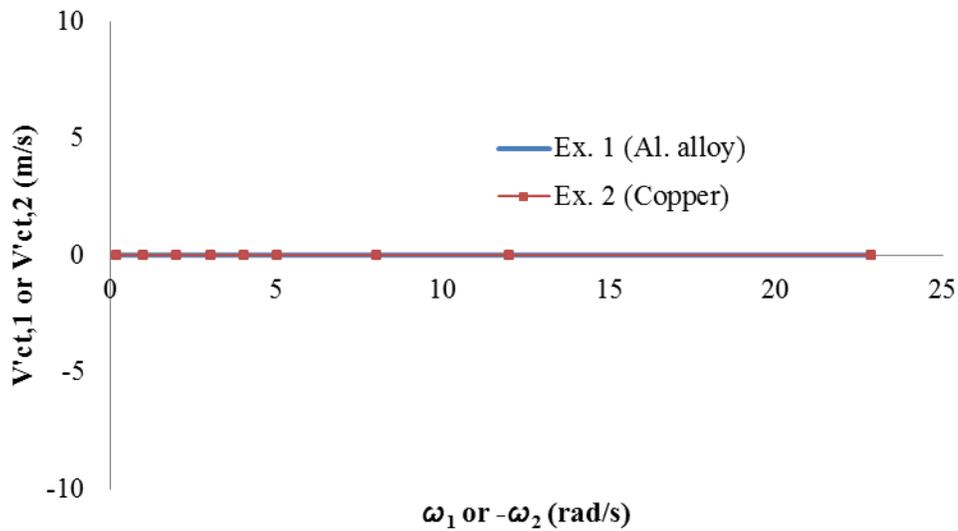
Figure 76. Test 7 DEM results for post-collision tangential velocity at the mass center for varying pre-collision angular velocities.
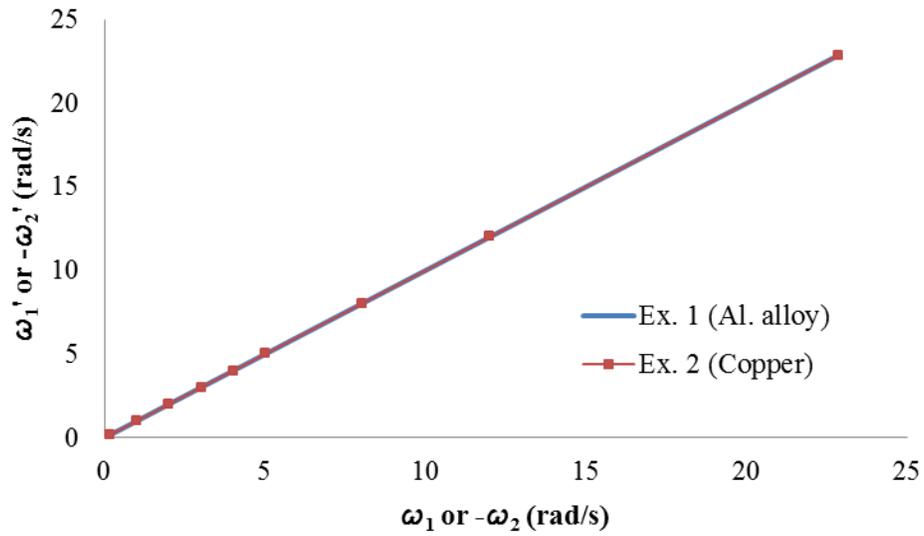
Figure 77. Test 7 DEM results for post-collision angular velocity for varying pre-collision angular velocities.

By comparing Figure 74 to Figure 76 and Figure 75 to Figure 77, the DEM model matches the published results and analytical solutions for Test 7.

APPENDIX F: TWO-DIMENSIONAL DISC ROOT DEVELOPMENT SIMULATION PARTICLE POSITION PLOTS

Particles with reinforcements are colored red. The lines showing the springs are not shown in Figure 78 through Figure 87, but can be seen by looking back to

Figure 22 through

Figure 26. Note that when the 2 second figure looks the same as the 3 second figure, movement has stopped. This can also be seen by comparing the almost horizontal lines on Figure 28 through Figure 32 from 2-3 seconds for the corresponding simulations. Also, when no particles are on the right side of BC3 and BC4, the right rigid wall and save mass boundary conditions, respectively, this corresponds to a final percent runoff of 0% in Table N.

Non-Reinforced

0 sec

1 sec

2 sec

3 sec

25% Shallow

0 sec

1 sec

2 sec

3 sec

25% Deep

0 sec

1 sec

2 sec

3 sec

50% Shallow

0 sec

1 sec

2 sec

3 sec

50% Deep

0 sec

1 sec

2 sec

3 sec

Figure 78. Slope 5.89º with 2.4 Drag Force Multiplier. Red particles are reinforced particles.

Non-Reinforced

0 sec

1 sec

2 sec

3 sec

25% Shallow

0 sec

1 sec

2 sec

3 sec

25% Deep

0 sec

1 sec

2 sec

3 sec

50% Shallow

0 sec

1 sec

2 sec

3 sec

50% Deep

0 sec

1 sec

2 sec

3 sec

Figure 79. Slope 5.89º with 3.2 Drag Force Multiplier. Red particles are reinforced particles.

Non-Reinforced

0 sec

1 sec

2 sec

3 sec

25% Shallow

0 sec

1 sec

2 sec

3 sec

25% Deep

0 sec

1 sec

2 sec

3 sec

50% Shallow

0 sec

1 sec

2 sec

3 sec

50% Deep

0 sec

1 sec

2 sec

3 sec

Figure 80. Slope 7.51º with 2.4 Drag Force Multiplier. Red particles are reinforced particles.

Non-Reinforced

0 sec

1 sec

2 sec

3 sec

25% Shallow

0 sec

1 sec

2 sec

3 sec

25% Deep

0 sec

1 sec

2 sec

3 sec

50% Shallow

0 sec

1 sec

2 sec

3 sec

50% Deep

0 sec

1 sec

2 sec

3 sec

Figure 81. Slope 7.51º with 3.2 Drag Force Multiplier. Red particles are reinforced particles.

Non-Reinforced

0 sec

1 sec

2 sec

3 sec

25% Shallow

0 sec

1 sec

2 sec

3 sec

25% Deep

0 sec

1 sec

2 sec

3 sec

50% Shallow

0 sec

1 sec

2 sec

3 sec

50% Deep

0 sec

1 sec

2 sec

3 sec

Figure 82. Slope 9.14º with 2.4 Drag Force Multiplier. Red particles are reinforced particles.

Non-Reinforced

0 sec

1 sec

2 sec

3 sec

25% Shallow

0 sec

1 sec

2 sec

3 sec

25% Deep

0 sec

1 sec

2 sec

3 sec

50% Shallow

0 sec

1 sec

2 sec

3 sec

50% Deep

0 sec

1 sec

2 sec

3 sec

Figure 83. Slope 9.14º with 3.2 Drag Force Multiplier. Red particles are reinforced particles.

Non-Reinforced

0 sec

1 sec

2 sec

3 sec

25% Shallow

0 sec

1 sec

2 sec

3 sec

25% Deep

0 sec

1 sec

2 sec

3 sec

50% Shallow

0 sec

1 sec

2 sec

3 sec

50% Deep

0 sec

1 sec

2 sec

3 sec

Figure 84. Slope 10.93º with 2.4 Drag Force Multiplier. Red particles are reinforced particles.

Non-Reinforced

0 sec

1 sec

2 sec

3 sec

25% Shallow

0 sec

1 sec

2 sec

3 sec

25% Deep

0 sec

1 sec

2 sec

3 sec

50% Shallow

155

0 sec   1 sec

2 sec   3 sec

50% Deep

0 sec   1 sec

2 sec   3 sec

Figure 85. Slope 10.93º with 3.2 Drag Force Multiplier. Red particles are reinforced particles.

Non-Reinforced

0 sec

1 sec

2 sec

3 sec

25% Shallow

0 sec

1 sec

2 sec

3 sec

25% Deep

0 sec

1 sec

2 sec

3 sec

50% Shallow

0 sec

1 sec

2 sec

3 sec

50% Deep

0 sec

1 sec

2 sec

3 sec

Figure 86. Slope 12.05º with 2.4 Drag Force Multiplier. Red particles are reinforced particles.

Non-Reinforced

0 sec

1 sec

2 sec

3 sec

25% Shallow

0 sec

1 sec

2 sec

3 sec

25% Deep

0 sec

1 sec

2 sec

3 sec

50% Shallow

0 sec

1 sec

2 sec

3 sec

50% Deep

0 sec

1 sec

2 sec

3 sec

Figure 87. Slope 12.05º with 3.2 Drag Force Multiplier. Red particles are reinforced particles.

APPENDIX G: THREE-DIMENSIONAL SPHERE ROOT DEVELOPMENT SIMULATION PARTICLE POSITION PLOTS

F.1 0.25 m/s Fluid Velocity

Non-Reinforced

0 sec

1.5 sec

3 sec

4.5 sec

6 sec

7.5 sec

10% Root

0 sec
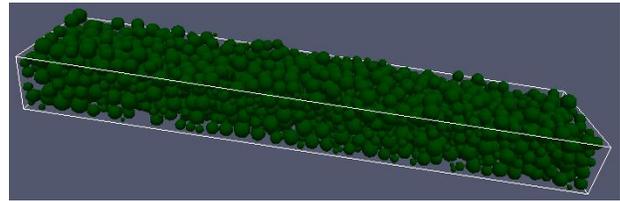
1.5 sec
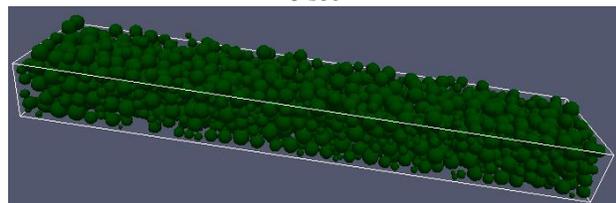
3 sec
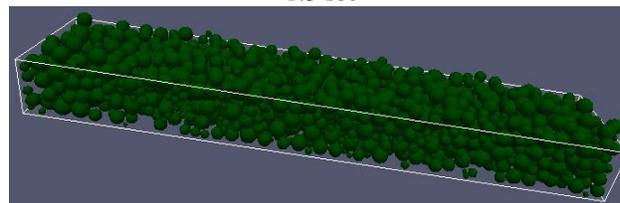
4.5 sec
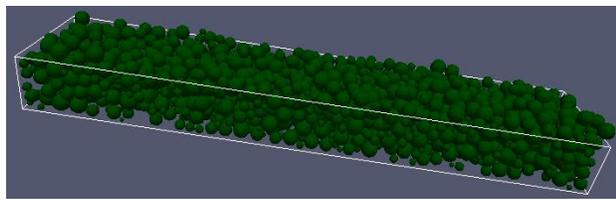
6 sec
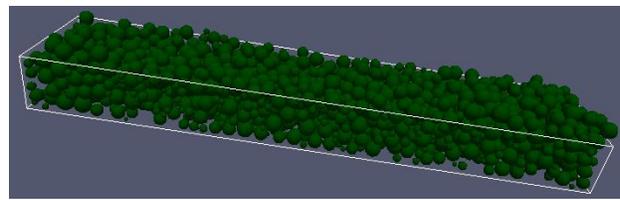
25% Root

0 sec
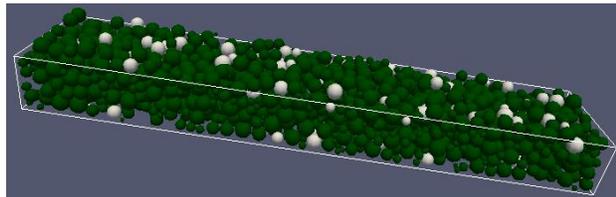
1.5 sec
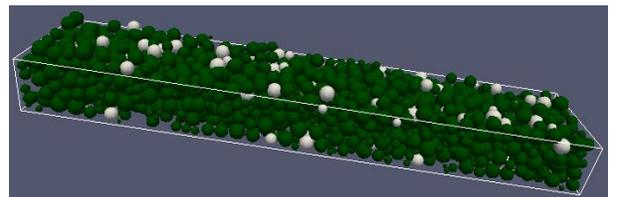
3 sec
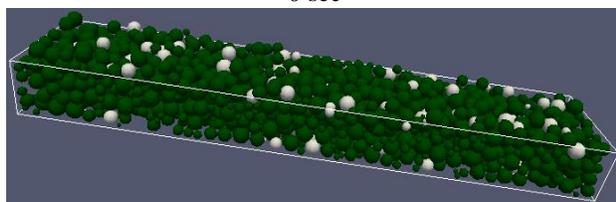
4.5 sec
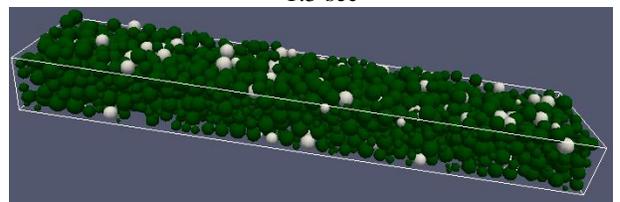
50% Root
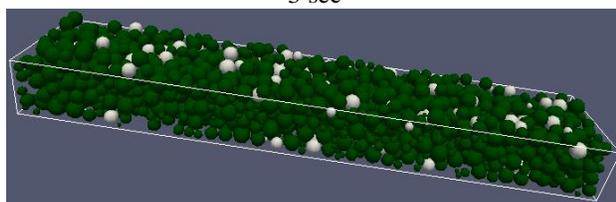
0 sec
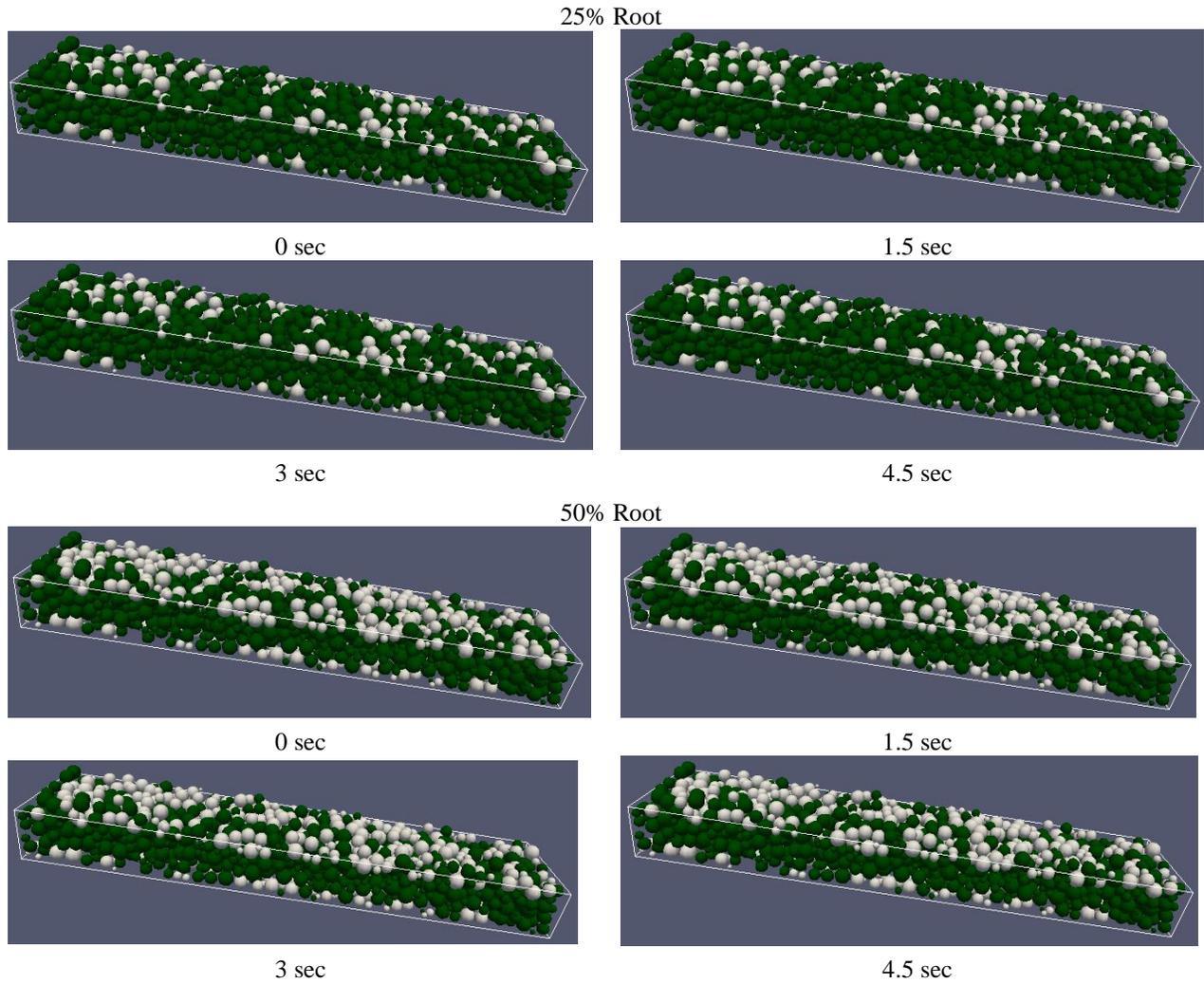
1.5 sec

3 sec

4.5 sec

Figure 88. Slope 9º with 0.25 m/s Fluid Velocity. White particles are reinforced particles.
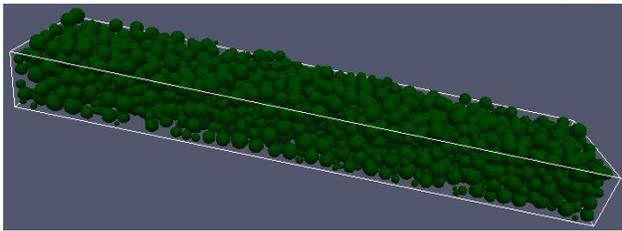
Non-Reinforced
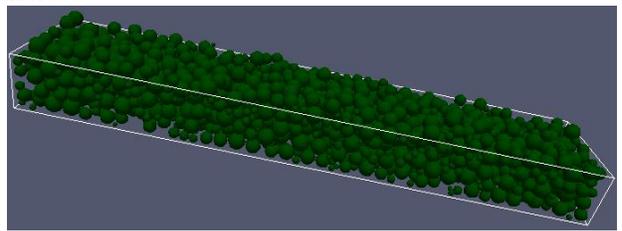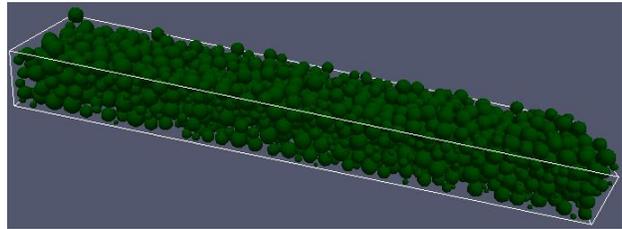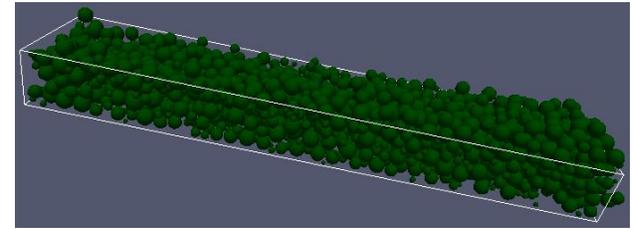
0 sec
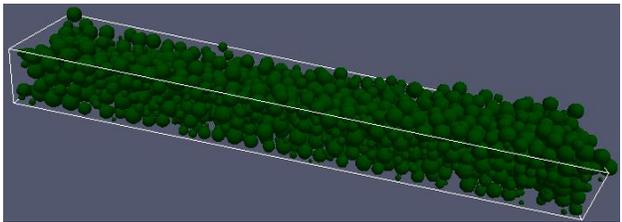
1.5 sec
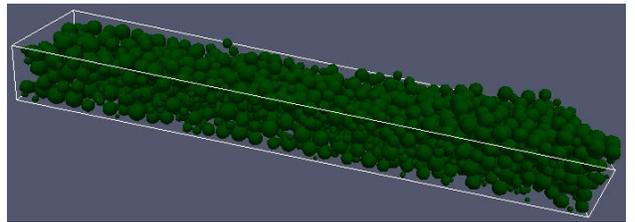
3 sec

4.5 sec
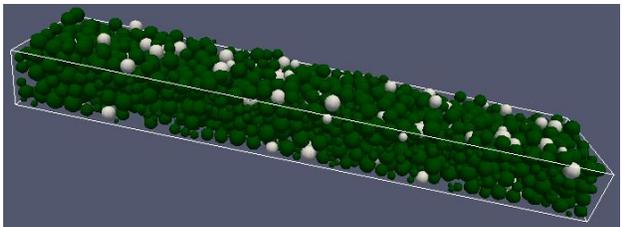
6 sec
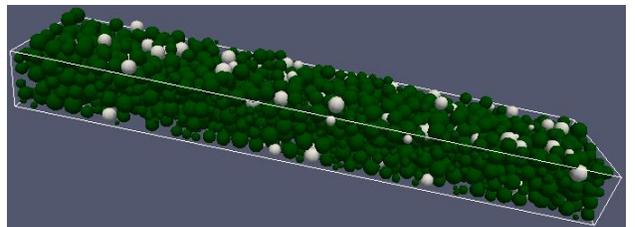
7.5 sec
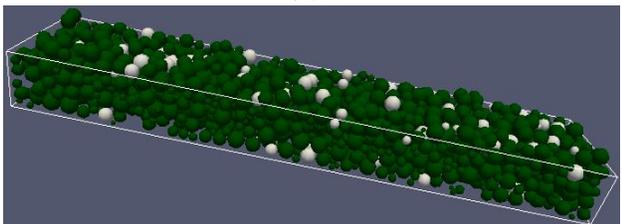
10% Root

0 sec

1.5 sec

3 sec

4.5 sec

6 sec

7.5 sec

25% Root

163

0 sec

1.5 sec

3 sec

4.5 sec
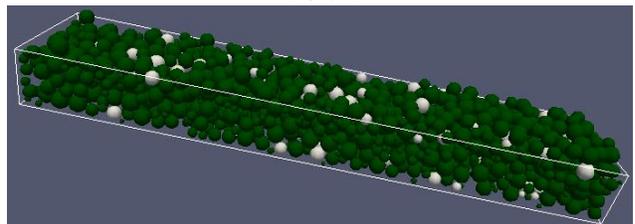
6 sec
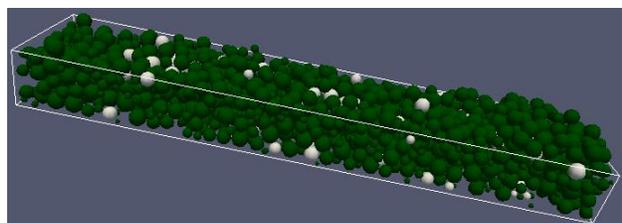
7.5 sec
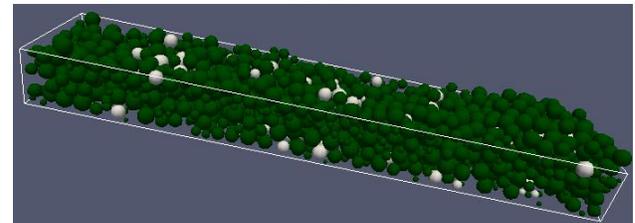
50% Root

0 sec
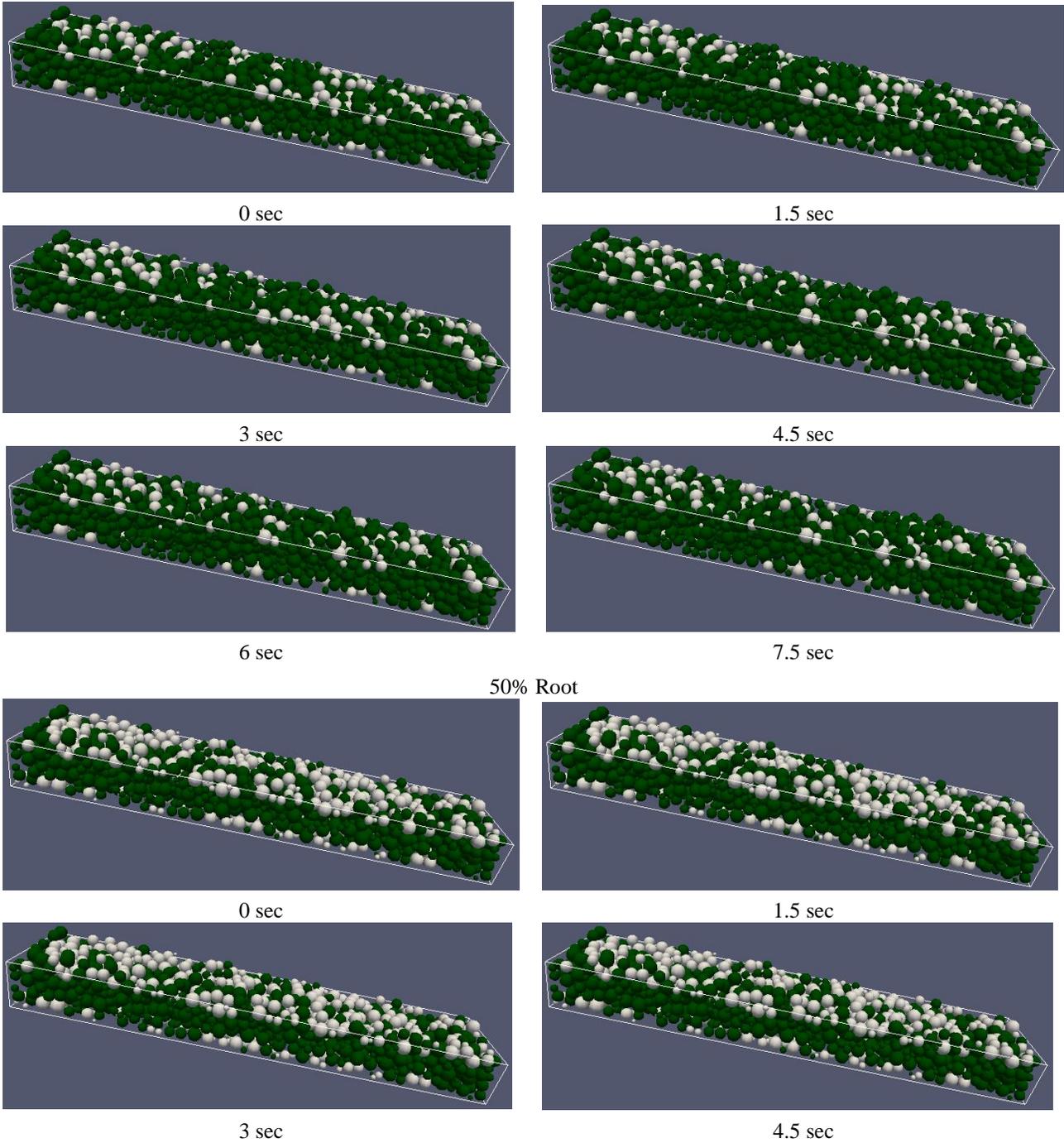
1.5 sec

3 sec

4.5 sec

Figure 89. Slope 12º with 0.25 m/s Fluid Velocity. White particles are reinforced particles.

F.2 0.5 m/s Fluid Velocity
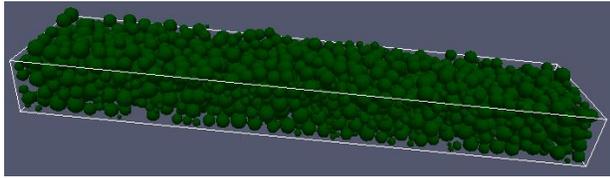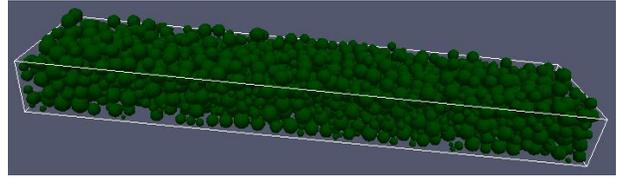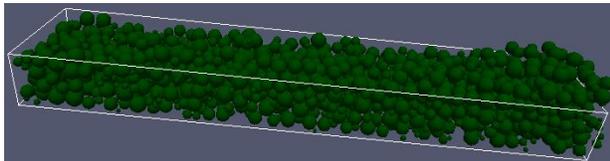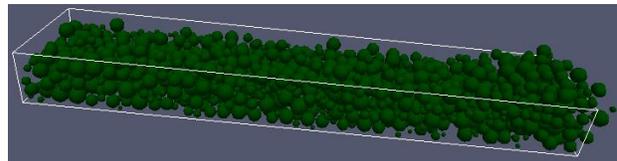
Non-Reinforced

0 sec

1.5 sec
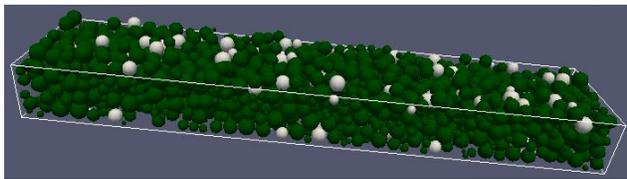
3 sec
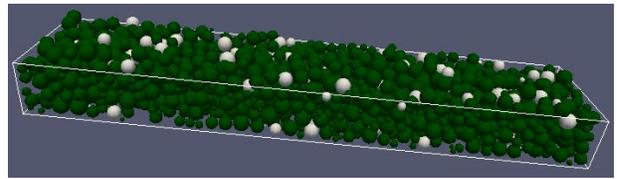
4.5 sec
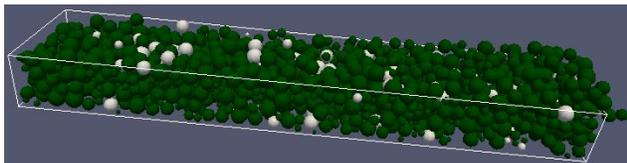
10% Root
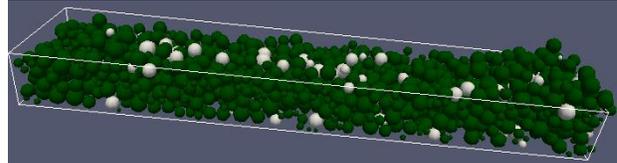
0 sec

1.5 sec
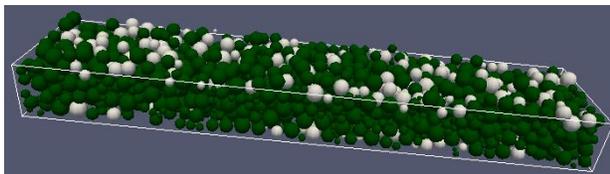
3 sec
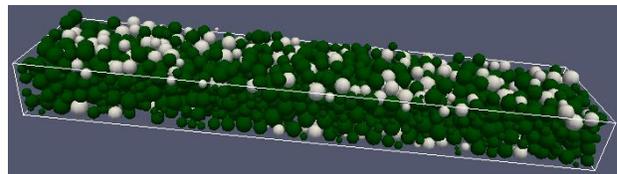
4.5 sec
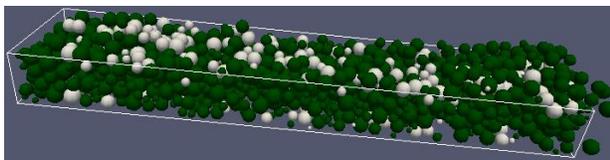
25% Root
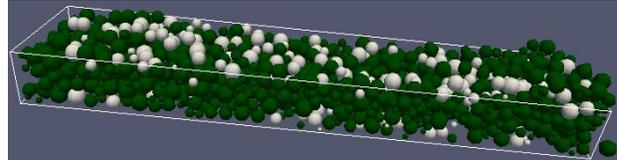
0 sec

1.5 sec
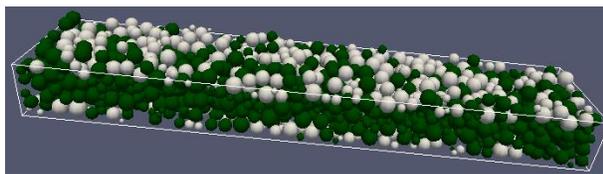
3 sec
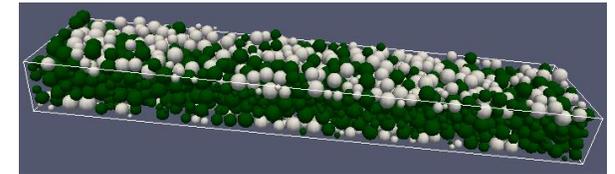
4.5 sec
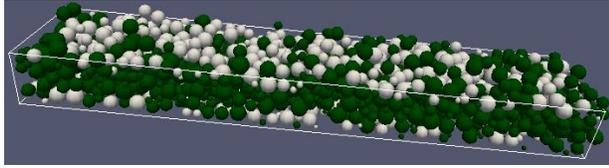
50% Root
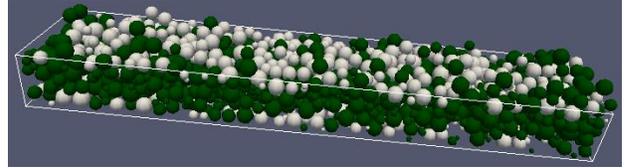
0 sec

1.5 sec

3 sec   4.5 sec

Figure 90. Slope 6º with 0.5 m/s Fluid Velocity. White particles are reinforced particles.
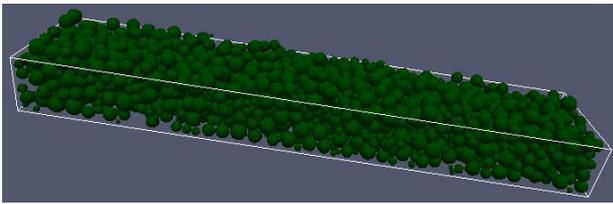
Non-Reinforced
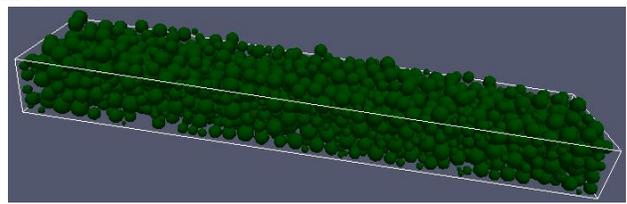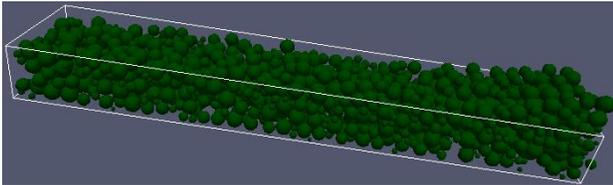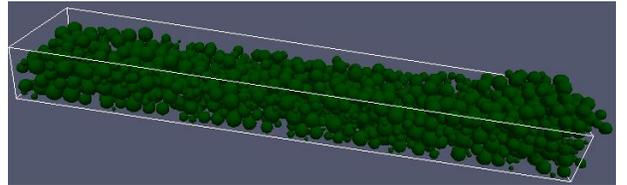
0 sec

1.5 sec
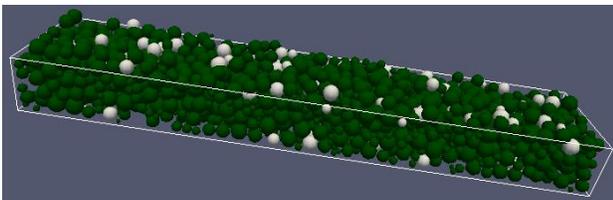
3 sec
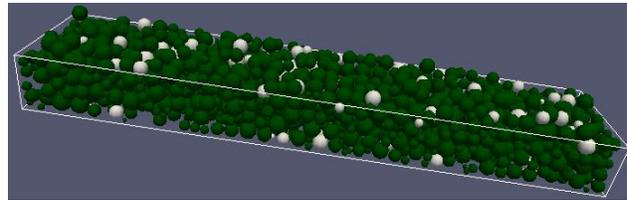
4.5 sec
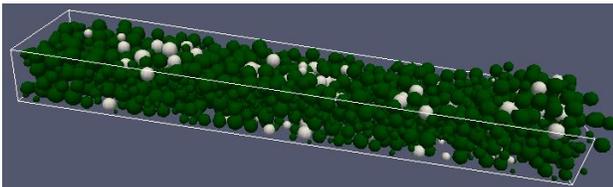
10% Root
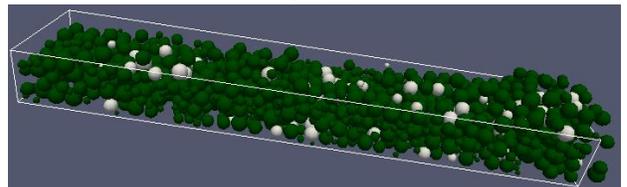
0 sec

1.5 sec
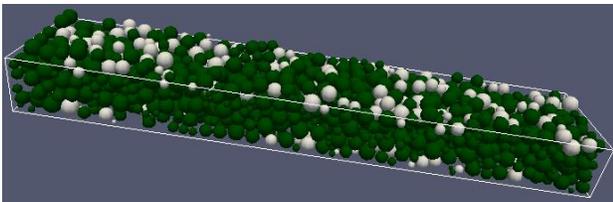
3 sec
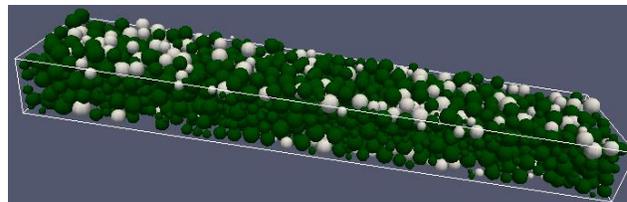
4.5 sec
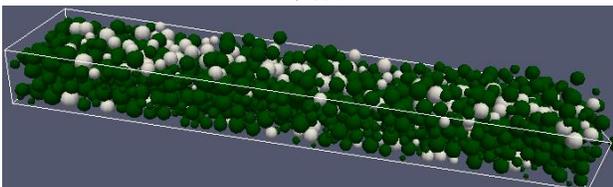
25% Root
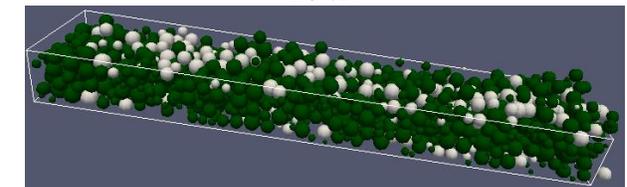
0 sec

1.5 sec
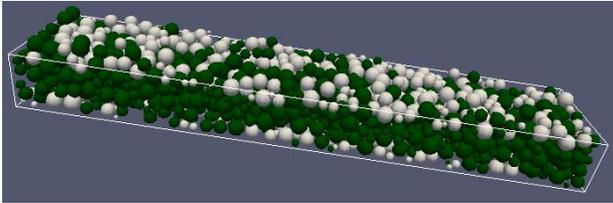
3 sec
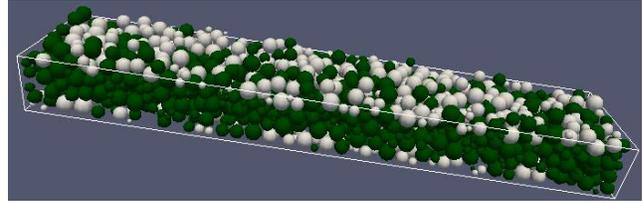
4.5 sec
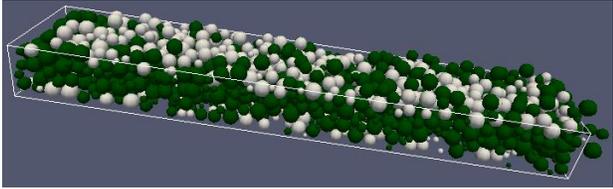
50% Root
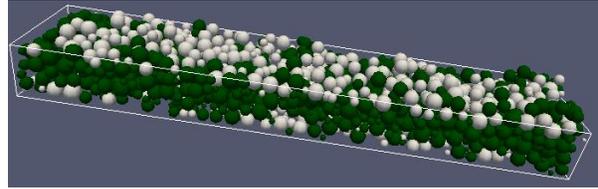
0 sec	1.5 sec

3 sec	4.5 sec

Figure 91. Slope 9º with 0.5 m/s Fluid Velocity. White particles are reinforced particles.

Non-Reinforced

0 sec

1.5 sec

3 sec

4.5 sec

10% Root

0 sec

1.5 sec

3 sec

4.5 sec

25% Root

0 sec

1.5 sec

3 sec

4.5 sec

169
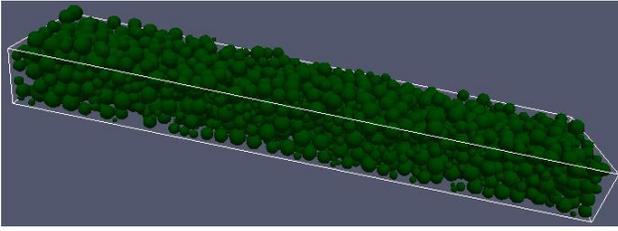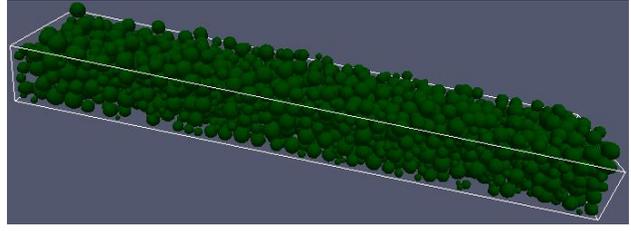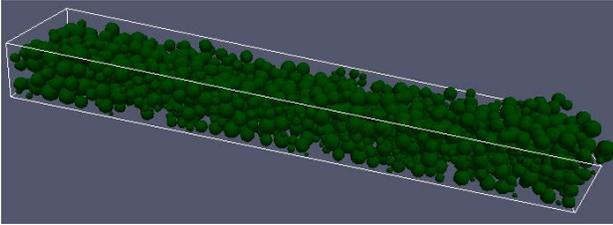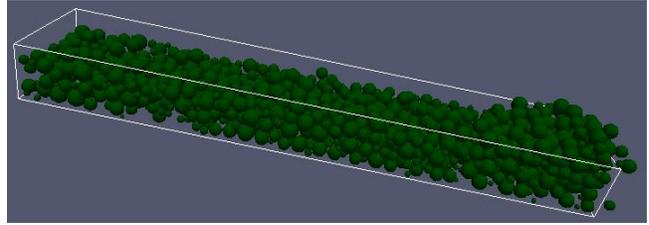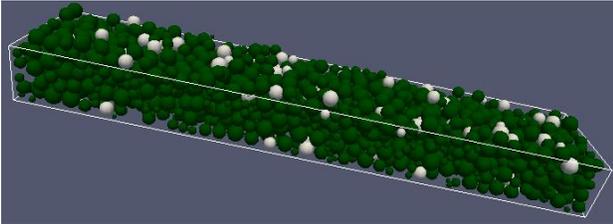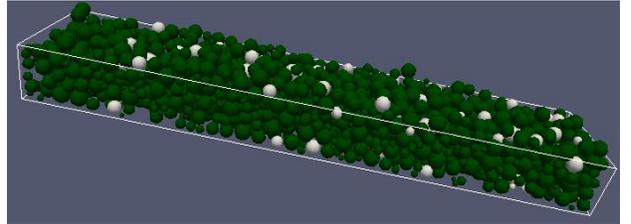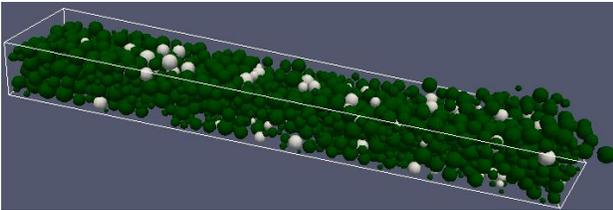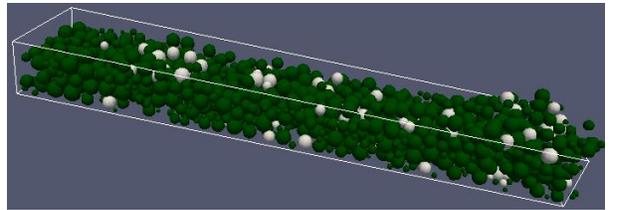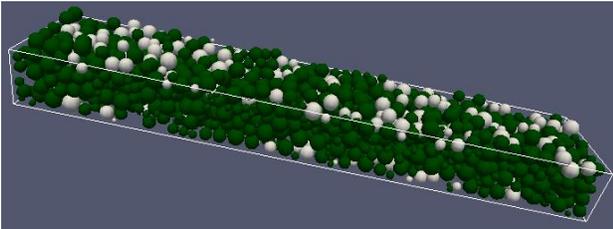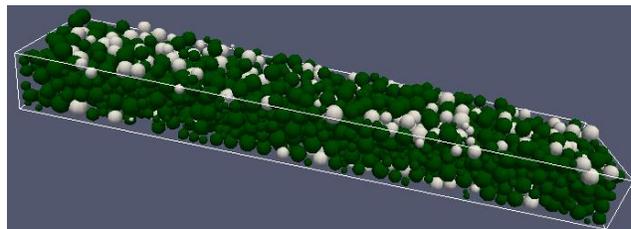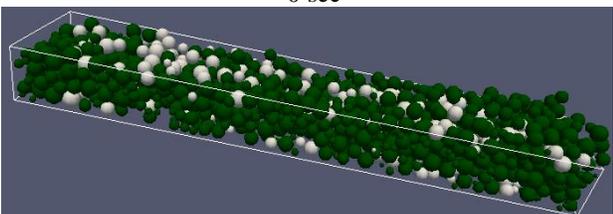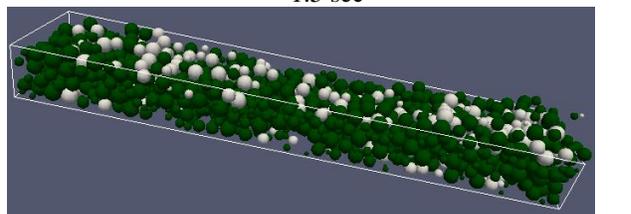
50% Root
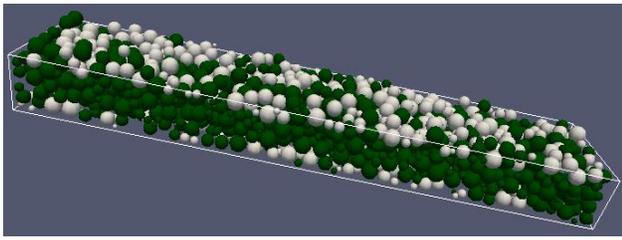
0 sec
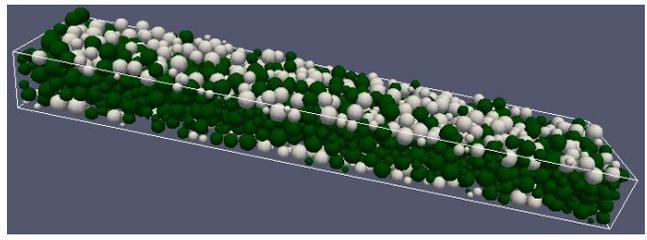
1.5 sec
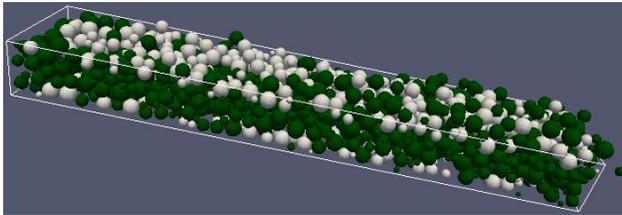
3 sec

4.5 sec

Figure 92. Slope 12º with 0.5 m/s Fluid Velocity. White particles are reinforced particles.